Irradiance simulation of PV system in urban environments

3D view factor model validation and comparison with ray-tracing methods

Ruben E. Cardose

Irradiance simulation of PV system in urban environments

3D view factor model validation and comparison with ray-tracing methods

by

Ruben E. Cardose

to obtain the degree of Master of Science
at the Delft University of Technology,
to be defended publicly on Monday January 20, 2020 at 10:00 AM.

Student number:	4206606	
Project duration:	January 16, 2019 – January 20, 2020	
Supervisor:	Dr. ir. O. Isabella	
Daily supervisor:	Ir. A. Calcabrini	
Thesis committee:	Dr. ir. O. Isabella,	Head of PVMD group, Assoc. prof. at Faculty of EEMCS at TU Delft
	Prof. dr. M. Zeman,	Head of the ESE department, Full professor at Faculty of EEMCS at TU Delft
	Dr. Ir. H. Ziar,	Postdoc researcher at TU Delft
	Dr. ir. P. Nourian,	Assistant Professor of Design Informatics at TU Delft
	Ir. A. Calcabrini,	PhD candidate at TU Delft

An electronic version of this thesis is available at `http://repository.tudelft.nl/`.

TU Delft

PVMD
Delft University of Technology

Preface

This master thesis marks the end of my studies at the Delft University of Technology. Throughout my studentship, I experienced some very memorable moments, made some great friends, met some inspiring people and of course gained a wealth of knowledge throughout. It also sparked a deep interest in solving the social and technical hurdles of today's society which brought me to study the most innovative technologies needed for a successful energy transition in my master Sustainable Energy Technology. Considering everything I learned, I am inspired and eager to apply everything learned to my future professional career. Everything mentioned earlier could not have been possible without a strong support group, for which I would like to reserve this chapter and show appreciation.

First of all, I would like to express great gratitude to all my graduation committee members, each of whom has provided me with expert advice, guidance, flexibility and understanding throughout the research process. I would like to thank my daily supervisor, Andres, for his excellent supervision. He guided me throughout the entire research project, helped me with all the simulations, was always available for a quick question and got the best out of me. Additionally, you went through my thesis multiple times with full commitment and precision. I would not have been able to complete this thesis without your help. Furthermore, I would also like to thank Dr. ir. Olindo Isabella for his passion and enthusiasm expressed during my project. Working under his supervision, both during my thesis project and my internship has enriched not only my academic career but also my prospective professional career. I am very grateful to have been able to take part of the PVMD group and make an contribution to the research conducted. I want to thank the entire PVMD group staff. I learned a lot from the presentations, reports and discussions at the weekly meetings. Finally, I want to thank Prof. dr. M. Zeman, Dr. ir. P. Nourian and H. Ziar for their willingness to be part of my graduation committee.

Looking back on my time as a student in Delft, I realize that this experience would not have been possible without the support of many people close to me. First my girlfriend Giandra, you encouraged me to follow my dreams and still try to do the master I want Sustainable Energy Technology, even though I am not directly applicable and needed to do a bridging program first. Without your encouragement and support, I would never have chosen this path and could not have achieved this degree. Additionally, you helped me to stay calm and relaxed when work or the study was tough. Thank you for all the love, support and patience you have shown me throughout. Also my Caribbean Combo friends Marson, Devin, Sharwan and Rais, thanks for everything. The parties, barbeques, pool nights, drinks and laughs were a very nice distraction. Jehan and Sharif, thanks to have been awesome neighbors. I very much enjoyed watching our games during the weekends. The deadlines we had to work on made them so much more exciting. To all my friends, hope to see much more of you and thank you all!

Last but not least, I want to thank my family. My mom, dad and sister, without their continuous love and support, I could not have achieved any of this. You have always supported me throughout my studies and life. Words can't express how much that means for me. Love you all!

Everyone, thank you all for your unconditional support, *masha masha danki*!

Ruben Cardose,
Delft, Januari 2020

Abstract

Within the coming years it is expected that PV installations could be established on every possible surface and terrain, within the urban environment. Due to the complex morphology of buildings in urban environments, systems will likely be more susceptible to partial shading compared to other conventional PV systems. In particular bifacial PV modules are highly susceptible to shading since they rely on irradiance on both the front and the back surface. To better estimate the irradiance received by such systems, particularly in urban environments, much research is conducted to develop fast and accurate simulation tools. The research described in this report investigated the different simulation frameworks that have been developed for modeling bifacial PV systems, and develop a new simulation framework capable of simulating irradiance within urban environments. Available models capable of simulating rear irradiance differ in input variables considered, simulation time required and accuracy of predictions. Empirical models, for example, can result in inaccurate predictions since not all variables affecting rear irradiance are considered. Only the 3D view factor, backward and forward ray tracing methods fulfill the requirements to simulate the backside irradiance/irradiation when the aim is to perform simulations in more complex urban environments. Out of the existing simulation models tested, the backward ray tracing model performed within the Radiance software proved to be the fastest simulation tool for modeling yearly irradiation or a single irradiance measurement incident under free horizon conditions. Time of use (TOU) simulations, however, results in longer simulation time for backward ray tracing performed in Radiance, since a ray tracing simulation at each time instance is required. To calculate the irradiance a receiving surface receives in an urban environment a method is worked out based on view factors and ray casting. Within the software Rhinoceros a CAD design of the surrounding environment is created, while the plug-in Grasshopper is used for the ray casting and mathematical calculations. Through a series of sanity checks, it was determined that the developed methods are reliable for calculating irradiance/irradiation when the aim is to perform simulations in more complex urban environments. It was also identified how different sky models can result in large differences in irradiance simulated. Sky models such as Isotropic, Hay and Davis or simplified Perez underestimates the irradiance, when receiving surfaces are tilted in comparison with the Perez luminance distributed sky model. The model was validated using monitoring station measurements and compared with simulations performed with other ray tracing models. DHI, DNI measurements obtained from the Solys 2 are used for replicating the irradiance measured at the dual-axis and single-axis tracker. Since their orientation was fixed throughout the measurement period they are referred to as POA 1 and POA 2 respectively. With POA 1 and 2 having a 90 and 30 degree tilt respectfully and an azimuth of 67 and 180 degree respectfully. Making POA 1 the front/back side of a typical (bifacial) east-west configuration and POA 2 the front of a tilted (bifacial) module. Two measurement days are considered, a fully overcast day and a clear sunny day. For the overcast day, an relative RMSE value of 23.09% and 11.7% are achieved for POA 1 and 2. For both cases the irradiation was mostly underestimated, considering the negative MBE and positive MAE. On the clear sunny day, relative RMSE values of 20.35% and 5.26% are achieved for POA 1 and 2. The model again mostly underestimates on the sunny day. A simple DHI correction with the factor $1/SVF_{Solys2}$ is performed in order to investigate the impact of potentially corrupted DHI measurements on the irradiance simulations. With relative RMSE value of 19.96% and 5.2% recorded for POA 1 and 2 on the overcast day. While on the sunny day relative RMSE values of 19.38% and 3.77% are achieved for POA 1 and 2 respectively. Only slightly changing the model predictions. When compared to ray tracing models the model performs slightly better than the forward ray tracing model. A possible reason why the forward ray tracing was underestimated was proposed to be due too the small aim area used. However increasing the aim area would require a larger number of rays to maintain the same accuracy which results in longer simulations. Possible improvements to the model could be, adding reflected irradiance term on reflecting surfaces and the Perez luminance distribution sky model.

Contents

List of Figures

List of Tables

1 Introduction

1.1. The solar energy potential

Renewable energy is essential for solving the urgent threat of climate change. To mitigate climate change, the Paris agreement was set up, with the long-term goal to keep the increase of global average temperature below 2°C. At the heart of the agreement lies the energy and electricity sector, the source for at least two-thirds of the greenhouse-gas emissions [11]. Aiming to reach the Paris agreement goals, it was determined that the energy sector needs to be transformed in a renewables-led sector. Recent technological developments and increasing concern over the past years have led to an increase in the share of renewables. But to successfully combat climate change and limit global warming to less than 2°C, this has not nearly been enough. Additional research in different renewable technologies is required to identify their potential.

One source of renewable energy that will play an important role in achieving climate agreement goals is solar energy. Solar energy (i.e., electromagnetic radiation) can be converted into electricity using photovoltaic (PV) technology. Globally around 100 GW_p of solar PV were installed by the end of 2017, accumulating the total installed capacity to around 400 GW_p [1]. According to projections made by IEA in a high-renewable scenario, solar PV could even reach 4.7 TW_p (4,674 GW_p) by 2050 [12]. This growth is in great part due to the predicted decline in the Levelized Cost of Electricity (LCOE) of solar energy and shows the importance of the research that needs to be conducted over the next decades.

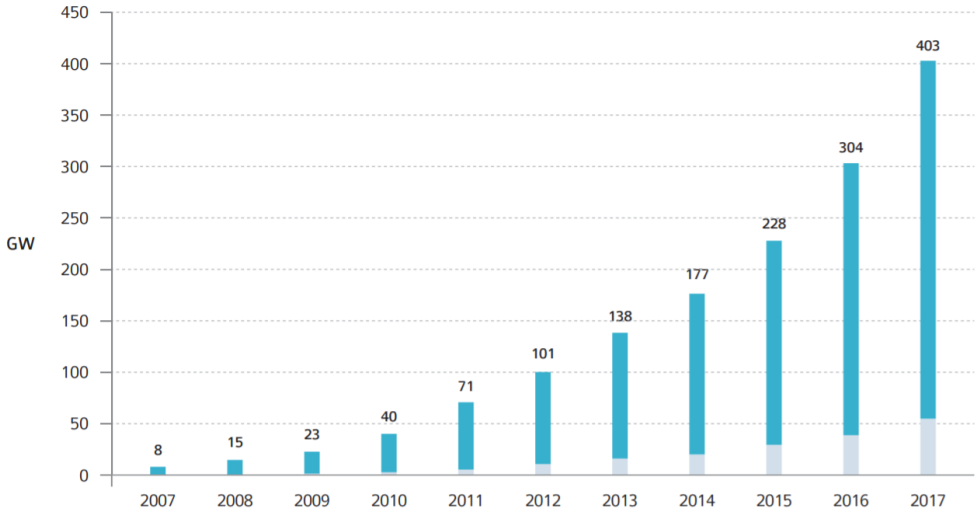

Figure 1.1: Evolution of cumulative PV installed. With the total accumulating capacity reaching around 400 GW_p in the year 2017 [1].

In the future, it is expected that energy demand will increase. One of the largest energy consumers is the building sector (both residential and commercial), which currently accounts for around 20% of the total delivered energy consumed worldwide [13]. Due to population growth, it is expected that in the future most

humans will be settled in much denser populated cities with urban landscapes. For this reason, more energy has to be generated within the city itself, to reach climate ambitions. This can be done for example by using solar panels that are placed on roofs, but also other surfaces, such as façades, roads, and pavements. Such PV modules are much more susceptible to a high amount of shading compared to modules installed in large scale solar power plants. Much research has been done in improving simulation tools to fast and accurately compute the energy yield under these conditions.

1.2. Bifacial PV

Solar PV can be categorized into monofacial and bifacial technologies. Monofacial PV can only use light incident on the front side of the device, while bifacial PV is able to use light incident on both sides. This, simply put, is done by substituting the typical back metallic contact of monofacial modules with a selective area contact like the one placed on the front side of the module. Currently, the PV market is mostly dominated by monofacial photovoltaic technology, but the bifacial PV technology is receiving considerable attention in recent years. The reason why bifacial PV is gaining so much attention by researchers is it has the potential to achieve higher energy yields compared to monofacial PV. The rear-side irradiation which is additionally collected by bifacial PV can offer great potential to decrease module cost and LCOE. Fertig et. al. strongly motivates the use of bifacial concepts to achieve the lowest LCOE in applications with sufficient rear-side irradiation [14]. The potential of bifacial PV has not gone unnoticed by the market. The ITRPV predicts that

Figure 1.2: Example of bifacial PV modules as seen from the back.

the share of crystalline silicon (c-Si) bifacial PV cells in the global market will continue to increase and could reach 35% by the year 2028 [2]. While forecasts surprisingly keep predicting higher markets shares in the future, past market share predictions have fallen short of the mark. The 35% bifacial PV market share can only be achieved if certain barriers for the adoption of bifacial PV are overcome. Two key barriers have been identified which must be addressed in order to promote the widespread use of c-Si bifacial PV devices in the future. Firstly, a universal bifacial PV performance measurement method/standard for indoor characterisation needs to be defined similar to the monofacials Standard Test Conditions (STC). And secondly, more comprehensive simulation models for outdoor performance characterisation must be developed and adapted [15]. Both are believed to increase the bankability of bifacial PV technology, ensure confidence in investors and hopefully result in higher bifacial market shares in the future.

As mentioned earlier, yield prediction models are necessary to simulate and predict the energy yield of a PV systems. These models must be able to develop, simulate and investigate a PV system on neighbourhood scale. Bifacial PV yield simulation frameworks can partly rely on models used in monofacial simulation frameworks, for example using the temperature and the electrical models. However, the irradiance model is different since the solar power incident on the rear side of bifacial PV must be calculated. For this reason the different existing irradiance models must be thoroughly investigated and possibly adapted.

1.3. Build environment and X-IPV

The built environment is a major consumer of energy worldwide. For example in Europe buildings are responsible for around 40% of the total energy consumption [16]. This is why the European Commission has set up the European Renewable Energy Directive, which states that all new buildings must be Nearly Zero-Energy Buildings (NZEB) by 2020 [16]. With NZEB meaning a building that has a very high energy performance. The nearly zero or very low amount of energy required should be covered to a very significant extent by energy from renewable sources, including energy from renewable sources produced on-site or nearby [16]. Improving the energy efficiency of buildings has many economic, social and environmental benefits. Furthermore, it also has many positive implications for the solar energy potential in this sector. Solar energy could be a decentralized power generation technology that's relatively easy to install. In NZEB's, the photovoltaic systems are one of the the most used renewable energy technologies. In Europe, around 90% of NZEB's or high efficient buildings expected to achieve the NZEB level have used photovoltaic systems [17].

In recent years solar energy has been installed in large numbers within the entire building sector, not just the NZEB's. IEA forecast an expansion of distributed PV generation within the building sector of almost half the total global PV capacity growth over 2018-23. This is led by commercial and industrial projects, and followed by residential applications. Homes, businesses and large industrial applications are expected to generate almost 2% of the global electricity demand by 2023 [18].

The growth of solar energy in the building sector goes hand in hand with growth in the Integrated Photovoltaics (X-IPV) market. Namely, the Building Applied Photovoltaics (BAPV) and Building Integrated Photovoltaics (BIPV) market sectors. In the case of BAPV the PV modules are added to the original structure such as roofs, while in BIPV the PV modules are integrated within the structure. In the past BIPV was a much more expensive solution than BAPV, and the main advantage in choosing BIPV was aesthetics. Due to the new regulations set on energy efficiency of building, this is expected to change in the future. BIPV offers the possibility of using vertical surfaces (e.g., façades) to generate electricity as the roof area of many buildings is limited. In many cases, BIPV will be the only way of reaching the energy performance requirements.

1.4. Societal and scientific relevance

The number of BIPV projects is expected to grow and due to the complex morphology of the buildings in the urban environment, it is very likely that systems will be more susceptible to partial shading than the more conventional BAPV systems. In particular the earlier mentioned bifacial PV modules are highly susceptible to shading since they rely on irradiance on both the front and the back surface. Since it has been identified that new simulation tools are needed, various new models have been developed for simulating incident irradiance on the rear surface of a bifacial module.

However, most of these simulation tools mostly assume that there are no surrounding objects that can cause shading on the PV modules. When assessing large scale PV systems, where the main source of shading losses is self shading, the simulation result can still accurately predict the energy yield. Various research studies have shown that these models can be used to accurately predict energy yield in free horizon locations. Nevertheless, in more complex urban landscapes the free horizon assumption can result in significant accuracy loss. Therefor, the impact of local shading should not be neglected.

There are some simulation frameworks/methods that allow to simulate the electrical performance of bifacial PV system taking into account the shading caused by surrounding obstacle. Most of these frameworks are based on ray-tracing methods which easily become highly computationally demanding. The large scale deployment of (bifacial) PV modules depends on the development of both fast and accurate simulations tools. For simulating bifacial PV modules within the urban environment this has proven to be difficult. It is also relatively unknown how the faster simulation tools perform when simulating more complex urban landscapes.

In recent years, various models have been developed in order to determine the incident irradiance on the back of the modules. The models can be categorized as emphirical, view factor and ray tracing based models. Various studies have been conducted in order to compare or validate their performance [19, 20]. These comparisons however are performed under simple horizons without considering shading of nearby obstacles typical in urban landscapes.

This research aims to explore the different simulation models for calculating the yield of bifacial PV systems specifically in scenarios with high amount of shading like urban landscapes. This analysis will determine which methods are more adequate for simulations in urban landscapes. The second objective is to improve the models that have the potential to be used in urban landscapes. The third objective is to use the simulation models on a bifacial PV systems within the urban environment.

1.5. Research objective

Based on the problem earlier defined, specific research objectives can be presented. The research objectives are as follows:

- First, identify, analyse and compare different modelling methods for bifacial energy yield simulation for simple free horizon landscapes.
- Secondly, develop, analyse and compare different modelling methods for more complex urban landscapes.
- Lastly, validate the simulation model with real life measurements.

1.5.1. Research questions

The aforementioned research objectives are aimed to be answered with this study. This can be summarized into one main research question. The research question is defined as followed:

- How and with which type of modelling framework can the irradiance received on a bifacial (BI)PV system be simulated while considering the impact of surrounding objects that can cause shading on such a system?

The main research question can be divided in more specific sub-research questions. Together, these questions should ultimately contribute to answer the main research question and close the research gap. The sub-questions are:

1. What are the most relevant variables influencing a bifacial PV system received irradiance?
2. How do different existing models perform in different landscapes, ranging from free horizon to more complex urban landscapes?
3. How do the simulation results compare to real life measurements?

1.6. Structure report and outline of thesis

In the first Chapter an introduction is given. The following Chapter 2, proceeds with giving more insight into theoretical background. Touching on topics like; how bifacial solar cells work, the different modelling methods that exist and explaining in more detail what this research aims to achieve. This chapter also contains a literature review which describes the current knowledge including previous findings, as well as theoretical and methodological contributions which this research aims to build on.

In Chapter 3, a simple comparison of the previously described models under free horizon conditions is presented. This chapter subsequently identifies each of the models advantages, drawbacks and more importantly describes the scope and applicability of each models output for an urban landscape.

In Chapter 4, the findings of the previous chapter are then used to compare and improve the different existing models for an typical urban landscape.

Chapter 5, describes a case study where the energy potential of bifacial PV modules on a vertical façade in a typical urban landscape are simulated.

Finally in Chapter 6, the research conclusions and recommendations for future research are presented.

2

Theoretical background

In this chapter, the current knowledge including substantive findings, as well as theoretical and methodological contributions of the research subject are given. This constitutes the basic understanding that is required to address the research objective formulated in Chapter 1. This is done by first giving a brief description of the history, current status and characteristics of bifacial PV cells and modules, then zooming in on the variables affecting bifacial PV energy yield. Finally, the different simulation models that exist are categorized and their underlying principles are described.

2.1. Bifacial PV technology review

2.1.1. History and growth expectation of Bifacial PV

History and current status of bifacial PV modules started in the year 1960, when a Japanese researcher named H. Mori proposed the first approach used to build a bifacial solar cell [21]. He did this by creating a collecting pn junction on each surface of a silicon wafer. The main purpose of this proposal was to increase the conversion efficiency of silicon solar cells, limited at the time by the diffusion length of minority carriers [22]. Since then, many researchers have been working on the solar cell described by H. Mori.

In the year 1977, the first bifacial lab cells with a creditable efficiency 12,7% for a 4 cm^2 area device were fabricated by the professor A. Cuevas with an n^+pn^+ / n^+np^+ junctions. This design proved crucial for the further development of the bifacial solar cell [22]. The research of H. Mori suggested the use of mirrors for collecting irradiance on the back of the solar cell for his patented design. A few years later the professor A. Cuevas and a group of researchers in Madrid by chance discovered a simpler and effective way to exploit the potential advantages of bifacial solar cells, by using the surrounding albedo [22]. It was shown that using mirrors or concentrators which here for was associated with bifacial solar cells was not needed since collecting the (natural or artificial) albedo was much easier. The professor and his research group showed that an increase of 50% in electric power generation can be obtained by simultaneously collecting direct and albedo radiation from the rooftop and surroundings around a module [23].

Since the invention of the bifacial solar cell by H. Mori and the fundamental discoveries of professor A. Cuevas, bifacial PV has become hot topic within the photovoltaic research community. A lot of research is conducted to improve the module efficiency and also accurately predict their potential. The general motivation being the expectation that bifacial PV will become more prevalent in the global market. The International Technology Roadmap for Photovoltaic (ITRPV) for example, predicts an upward trend of the crystalline silicon (c-Si) bifacial PV cells shares in the global PV market. Since its first appearance in the ITRPV roadmap of 2015, the predicted market share keeps becoming increasingly positive. With the latest ITRPV roadmap 2018, displayed in Fig. 2.1 below, even expecting an 35% market share by the year 2028 [2]. Some reports also go as far as to indicate that bifacial PV is becoming the most promising technology to lower the cost of solar PV to the U.S. Department of Energy's 1 USD/W_p system size target [23]. However, to achieve this it is important to not only understand the working principle of this new emerging technology but also identify the challenges and opportunities of this technology. This is what the following subparagraphs aims to do.

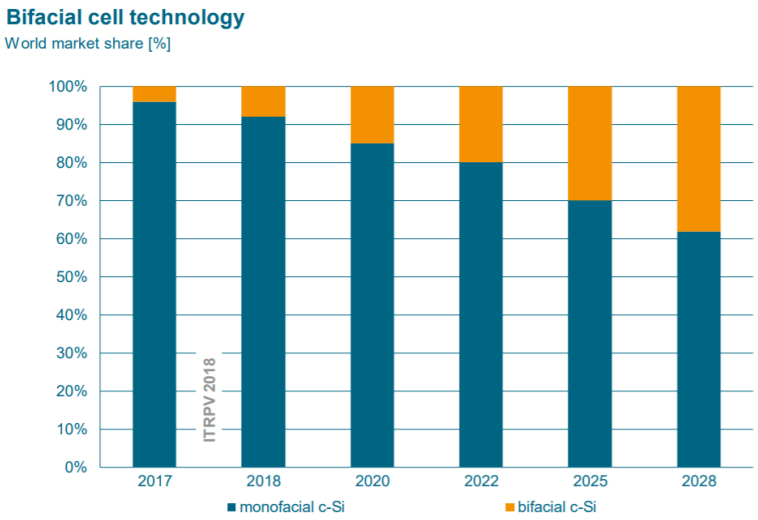

Figure 2.1: ITRPV worldwide market share predictions. Taken from [2]

2.1.2. Bifacial PV cell- and module structure

As was already previously mentioned bifacial solar cells can simultaneously collect photons from incident and albedo radiation reaching both the front- and back-side of a solar module. Monofacial solar cells however can only collect photons reaching the front side of the device. Consequently, bifacial solar cells can increase the power density of PV modules compared to monofacial cells while reducing area-related costs for PV systems [23]. What makes these types of solar cells able to do this can be explained by looking at Fig. 2.2, which shows a cross-section of a standard bifacial crystalline silicon solar cells next to the well known Al-BSF monofacial solar cell. As can be seen in the figure, the main difference between the monofacial and the bifacial solar cell is in the back-side. With the monofacial consisting of a reflecting back sheet while the bifacial consist of a metallized grid structure making the rear transparent when an anti-reflection coating (ARC) layer is added on the backside to reduce the light reflection. The open metallization grid is printed on both sides to simultaneously absorb illumination from either side or both. While the figure shows a p-type bifacial solar cell an n-type solar cells variant can also be created. For the p-type, the emitter is the n^+ which serves as the diffused layer, where as the p^+ layer serves as a back surface field (BSF). The opposite counts for the n-type solar cell.

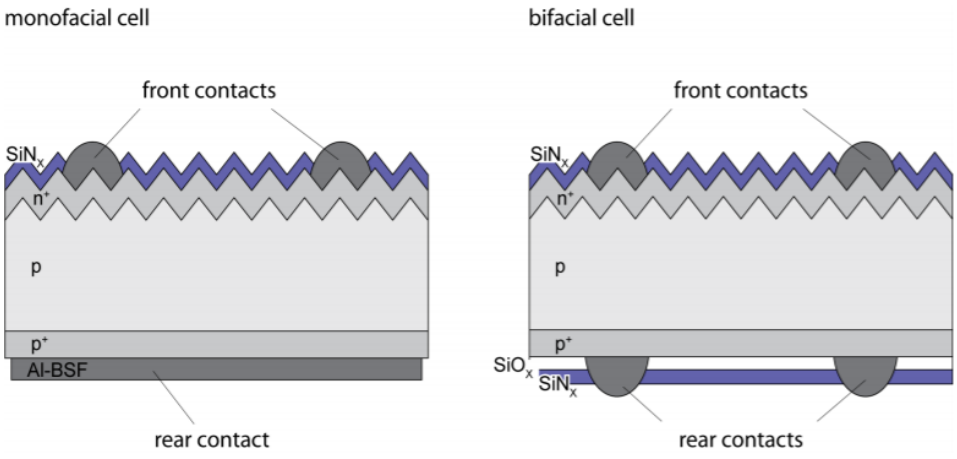

Figure 2.2: Sketch of standard n-type monofacial and bifacial crystalline silicon solar cells. Taken from [3]

The above mentioned solar cells are connected and encapsulated in order to form a bifacial PV module. Just like the bifacial solar cell differs from the monofacial solar cell, the module structure is also different since it needs to allow rear irradiance. In the Fig. 2.3, the difference between a monofacial and a bifacial

PV module structure is displayed. As can be seen both modules consist of a number of cells connected in series, with the most common modules having either 60 or 72 cells with three bypass diodes. Then the cells are encapsulated in order to provide adhesion between the solar cells, the top surface and the rear surface of the PV module. EVA (ethyl vinyl acetate) is the most commonly used encapsulant material. Both monofacial and bifacial modules have a similar front surface material, usually glass but also acrylic and polymers are possible. The main reason for using these materials is because they are optically transparent. The difference between the monofacial and bifacial modules lies at the rear surface material. Bifacial PV modules similar to the front surface material have an optically transparent back surface material, like glass, acrilic or polymers, in order to accept light from the rear of the modules. On the other hand, most monofacial modules consist of a thin polymer sheet, typically Tedlar, at the rear surface. For the rear surface, besides of course being optically transparent for bifacial PV modules, the key characteristics of the PV module are also that it must have low thermal resistance and that it must prevent the ingress of water or water vapour.

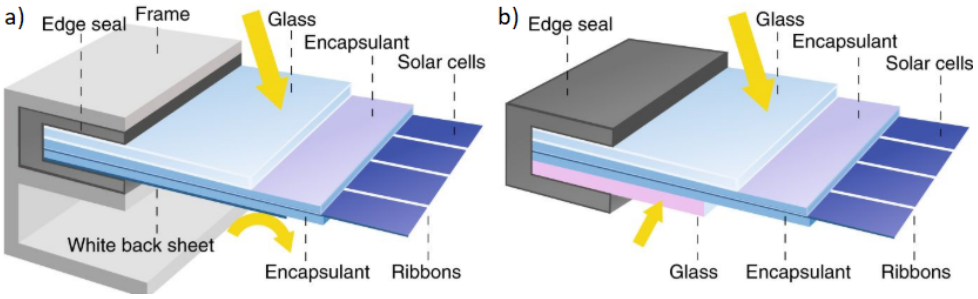

Figure 2.3: Sketch of (a) Monofacial module and (b) bifacial module structure. Taken from [4]

2.1.3. Important bifacial PV characteristics

Bifacial modules are characterized by their bifaciality factor (ϕ_{Pmpp}), which is defined as the ratio of efficiencies (η) illuminating exclusively the front or the rear-side of the solar panel, and can be expressed as [19, 23]:

$$\phi_{Pmpp} = \frac{\eta_{mpp,rear}}{\eta_{mpp,front}} \cdot 100\% = \frac{P_{mpp,rear}}{P_{mpp,front}} \cdot 100\% \tag{2.1}$$

The bifaciality factor varies depending on cell and module design. In literature values have been reported as high as 99% , but usually ranges commercially between 60% and 90% [19]. While for monofacial solar module a consensus based standard for testing and rating modules under a specific laboratory conditions was defined, named the Standard Test Conditions (STC), there is no such condition yet defined for bifacial solar cells [23]. The bifaciality factor and other previously used methods to characterize bifacial cells report the front and rear side efficiency of bifacial solar cells separately, and do not provide information regarding bifacial operation under both front and rear illumination, since the bifacial characteristics are not simply a linear combination of the monofacial characteristics [24]. It was not until recently that a measurement setup was proposed, by adding mirrors and filters to solar simulators under STC, to consider bifacial cells under both front and rear illumination conditions [23]. Since then some new alternative parameters have been defined to characterize bifacial solar cells under both front and rear illumination. Some important parameters being, the irradiance gain (g) and the irradiance factor (x), which can be expressed as [24]:

$$g = \frac{G_f + G_r}{G_f} \tag{2.2}$$

and

$$x = \frac{G_r}{G_f} = g - 1 \tag{2.3}$$

Consequently, the bifacial $1x$ efficiency (η_{1x}) can be defined, as the efficiency which occurs when a bifacial solar cell is simultaneously illuminated on the front and x times the front irradiance on the rear side of a solar cell. Lastly, the actual gain from a bifacial PV module in reference to a monofacial module can be determined by a parameter called the gain efficiency product (GEP), which can be expressed by[23]:

$$GEP = \eta_{1x} \cdot g \tag{2.4}$$

2.2. Variables affecting bifacial PV energy yield

Like a monofacial module, also a bifacial module performance depends on a set of variables. With a simulation model the variables can be inserted and through physical models a desired output like energy yield or surface utilization can be calculated. Before the different models available are identified, the different variables which a bifacial PV module depends on will be identified. In the Fig. 2.4 below, for simplicity a simplified diagram of a bifacial PV system is displayed. As the figure shows the variables are categorized into 4 types of subcategories, namely installation parameters (yellow), external parameters (blue), output parameters (green) and the model parameters (grey).

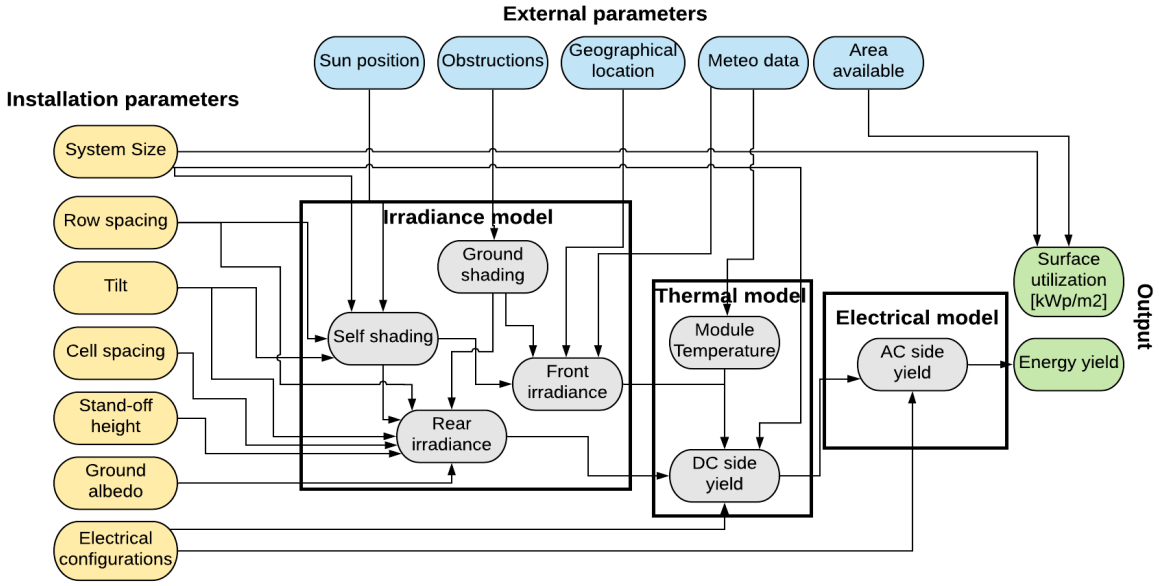

Figure 2.4: Simplified relation diagram of an bifacial PV system.

One important reason for simulating the operation of a bifacial PV system is to make an estimate of the potential energy yield of such a system, since the energy yield determines the LCOE and payback time of the system. These financial indicators are important to ensure convince potential investors to invest in bifacial PV systems. When an unlimited amount of space is available the energy yield is usually the most important parameter. And explains why lots of research have the main objective to improve the efficiency of the different components of the system. However, when a limited amount of space is available, like in most urban environments, another important parameter is the surface utilization. Bifacial modules can have a direct impact on the surface utilization. Which is why the surface utilization, especially for bifacial systems in the urban environment should also be considered. As the Fig. 2.4 shows, the potential energy yield and surface utilization of a PV system can be simulated through three sub-models, namely the optical model, the thermal model and lastly the electrical model [15]. In particular the irradiance model is different when simulating an bifacial module compared to an monofacial module. The results of the module depend on different parameters, which can be split into installation and external parameters. With the installer or designer having control over the installation parameters of the PV system and the external parameters being predefined depending at which particular location, landscape or climate, the PV system will be installed.

2.2.1. Impact of installation parameters and system size

As was mentioned earlier for bifacial PV systems compared to monofacial PV system special attention to the irradiance model needs to be given. The irradiance model is used to calculate the amount of irradiance the module recieves on the front- and backsides. The irradiance recieved consist of three components [25]: direct, diffuse and ground oor surface reflected irradiance as shown in the left side of Fig. 2.5.

Over the past years, various studies have been performed that show the impact of installation parameters on the energy yield of a bifacial PV system [15, 26]. The most important installation parameters being; Tilt, Stand-off height, Row spacing and depending on the situation also cell spacing and ground albedo. Another important parameter especially for bifacial pv system is the system size. Since bifacial modules in large scale

systems, generate lower energy due to large shadowing areas cast by the modules on the ground [26]. In the following paragraph the importance of shading for bifacial PV will be explained.

2.2.2. Impact of self/mutual- and ground reflected-shading

While the front surface irradiance of a bifacial module can be calculated similarly to a monofacial module, the irradiance on the rear surface of bifacial module is more complex to model.When the module is tilted the main irradiance components on the front surface are direct and diffuse irradiance. The rear surface mostly receives ground reflected and diffuse irradiance. In the Fig. 2.5 an example is given of the shares of the direct, diffuse and ground reflected irradiance on the front and rear surface of a 30° tilted or vertically placed bifacial PV module. The amount of irradiance the rear surface receives reflected from the ground is greatly dependent on the environment behind the module. Due to this phenomena, the irradiance on the back of a bifacial PV can be even more susceptible to shading since it not only depends on a shaded module but also shading of the surrounding behind the module. It is important to take this into consideration especially for scenarios in an urban landscapes.

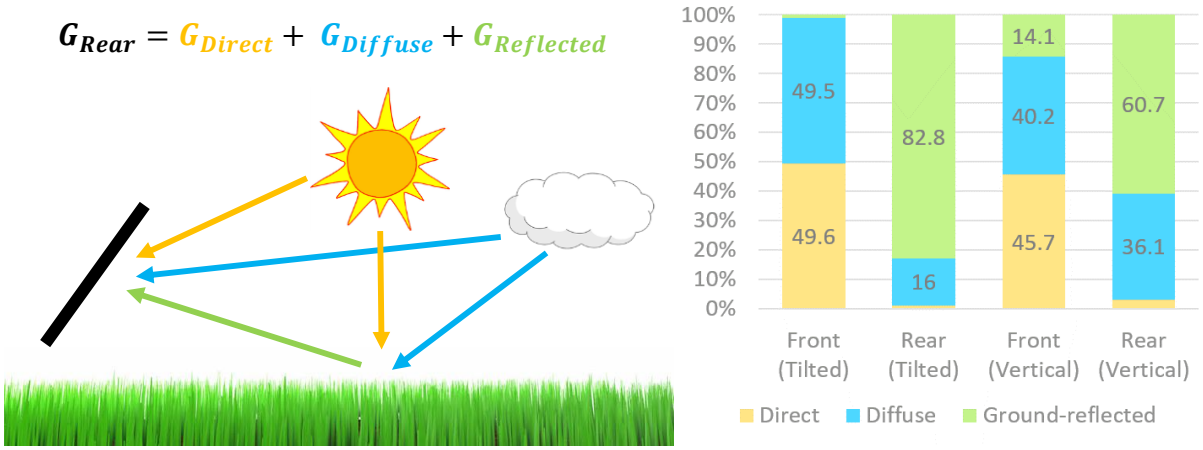

Figure 2.5: Example of irradiance components on Front and Rear surface of a single south-facing bifacial PV module tilted 30° or placed vertically with default values for stand-off height = 0.5, albedo = 0.25, Azimuth = 180°and cell spacing = 0 mm for a simple horizon.

For simplicity, a distinction is made between self/mutual- and ground reflected-shading. Self/mutual shading is the condition when (part of) a PV module and the mounting structure, casts a shadow on itself or other modules in the vicinity. While the term ground reflected shading is used when the module or any other obstruction nearby cast a shadow on the ground nearby the PV array. The difference between the two subsequently also indicate which type of irradiance will be blocked. With self/mutual shading blocking direct radiation and ground reflected shading as the name suggest blocking part of the reflected irradiance a module receives from the ground. Over the past years the effect of self/mutual shading has been thoroughly studied since this type of shading is typical and important for a monofacial modules performance [27]. Ground reflected shading blocks part of the irradiance reaching the ground which could have bounced back into the module. Since bifacial PV irradiance on the rear is highly dependent on the ground-reflected irradiance, as Fig. 2.5 earlier suggested, this type of shading is very important to consider for situations with a high dependency on ground reflected irradiance. Especially within urban landscapes which typically suffer from a lot of shading.

2.3. Irradiance simulation frameworks for bifacial PV modules

There are several models that have been developed to calculate the irradiance on bifacial PV systems. These models put special focus on the calculation of the rear side irradiance. Since the main source of irradiance on the rear side is ground-reflected irradiance and/or diffuse irradiance. The methods for back surface irradiance modelling fall into three categories:

- Empirical models; which establish a relationship between front and rear irradiance based on measurements [28, 29]

- View factor models; quantifying the proportion of the radiation which leaves a surface A that arrives at surface B [30–32]
- and Ray-tracing models; which simulate multi-path reflections and absorptions of individual rays entering a scene[20, 33].

Each of these models are described in detail in the following sections.

2.3.1. Empirical models

Empirical models are simplified analytical approximations based on a combination of measurements and simulations. They use a more limited set of variables to calculate an approximate bifacial gain of bifacial PV modules compared to monofacial PV modules.
Two well known and widely used emperical models will be described. The first one being a model which allows yearly Bifacial Gain in Energy (BGE) calculation for single bifacial PV modules [28]. The BGE, expressed in percentage, is the amount of energy that the rear side of a bifacial module generates as a function of the amount of energy generated by the front side of the bifacial module, and can be expressed by:

$$BGE[\%] = \frac{E_{rear}}{E_{Front}} = \frac{E_{Total,Bifacial} - E_{Front}}{E_{Front}} \tag{2.5}$$

E_{Rear} is the energy from the rear surface of the system/module and E_{Front} is the energy from the front surface of the module/system. The BGE can be calculated as:

$$BGE[\%] = A \cdot \beta + B \cdot h + C \cdot \alpha \tag{2.6}$$

where A is the fit coefficient for the tilt angle, β is the tilt angle of the module in degrees for a range of 7.5°to 35°degrees, B is the fit coefficient for the stand-off height of the module, h is the minimum stand-off height ratio of the bifacial module in meters for a range of 0.15m to 0.8m, C is the fit coefficient for albedo, and α is the average minimum surface albedo surrounding the bifacial module in percentage. The final set of emphirical coefficients were found to be A=0.317/deg, B=12.145/m, and C= 0.1414/%. This model is only intended to cover a limited range of installation conditions, avoiding extraneous conditions, such as racking/system shadowing to the rear of the bifacial modules, and only covers the most common installation conditions of PV modules. The model was also estimated for modules with a bifaciality factor of 95%. In order to adapt the energy yield model for another type of bifacial module with a different Bifacial factor (ϕ_{Pmpp}) the BGE must be multiplied with the new bifacial factor and divided by 95%. Lastly, the BGE values of this empirical model is intended as a single annual value and when used for running time of use (TOU) computations, it averages out the BGE variations that are expected throughout the day and seasons. A second empirical model note mentioning is a model which is based on system-level ray-tracing simulations proposed by Kutzer et al. [34]. the BGE estimation of the model is calculated as:

$$BGE[\%] = \alpha \cdot \phi_{Pmpp} \cdot 0.95 \cdot [1.037 \cdot (1 - \sqrt{gcr}) \cdot (1 - e^{-8.69 \cdot h \cdot gcr}) + 0.125 \cdot (1 - gcr^4)] \tag{2.7}$$

With h being the normalized clearance height h = H/CW, gcr being the ground coverage ratio and ϕ_{Pmpp} being the bifaciality factor. As can be noted by the previous equations of the two emphirical models, these type of models do not include all the effects of installation parameters and do not consider the climate variations that are expected throughout the day and seasons. Also urban landscapes are not considered with these models.

2.3.2. View factor models

More advanced method for modeling rear irradiance is based on view factors method. There are several view factor based models developed by various research institutes such as PVSyst [32], NREL [30] and Sandia National Laboratories [31]. View factors are used to quantify the fraction of reflected irradiance from one surface that arrives at another surface. The view factor from a general surface A_1 to another general surface A_2 is depicted in Fig. 2.6. View factors can be calculated with the following formula [20]:

$$VF_{1\rightarrow 2} = \frac{1}{A_1} \int_{A1} \int_{A2} \frac{cos(\theta_1) cos(\theta_2)}{\pi s^2} dA_1 dA_2 \tag{2.8}$$

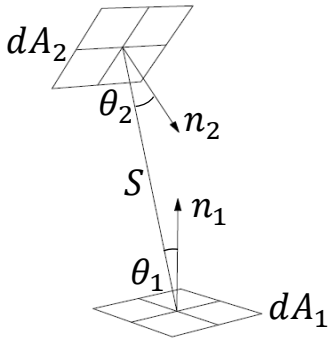

Figure 2.6: Visual representation of a view factor.

The view factor model assumes that all reflecting surfaces are Lambertian, i.e., irradiance is scattered isotropically [31]. A distinction can be made between the 2 Dimensional view factor models of PVSyst/NREL model and the 3 Dimensional view factor model of Sandia's. Each will be described separately.

2D view factor model

The 2D view factor models from NREL and PVSyst are designed for calculating the rear irradiance of one row or multiple rows of bifacial photovoltaic (PV) modules. The model calculates the backside irradiance for each row of cells to quantify the radiation profile in the PV module slant height direction, but does not distinguish differences in backside irradiance along the row's length [30]. The benefit of only considering cells along the module height is that it permits faster program execution because the backside irradiance is not determined for all the PV cells in a PV system. Even though simulations have shown increased backside irradiance for modules on the edges of rows[31], according to the model developers this effect is not significant for a PV systems with more than a dozen PV modules per row [30]. Since the NREL and PVSyst model are very similar only the NREL model will be described. The NREL model working principle can be subdivided into three steps:

1. First, identifying the part of the ground that is shaded by the PV array
2. Then determining the irradiance received by the ground by accounting for the effect of shading and the restricted view of the sky
3. Lastly, determining the total irradiance recieved by the backside of the PV module.

In the first step, the installation parameters (e.g. tilt, azimuth, stand off-height etc.) and climate data are used to calculate the sun position at each hour of the year and project shadows in the row-to-row (rtr) dimension. The rtr is divided into i segments (such as 100) and the incident irradiance directly, diffuse and reflected from each ground segment is evaluated. The total irradiance on the back can be divided into the following irradiance components [31]:

$$G_{Rear} = G_{Direct} + G_{Diff} + G_{Ground} \tag{2.9}$$

The total irradiance on the rear of the solar cell according to the 2D view factor model can be calculated with the equation [30]:

$$G_{rear} = b \cdot F_b \cdot (DNI + I_{cir}) + \sum_{i=1^o}^{180^o} VF_i \cdot F_i \cdot I_i \tag{2.10}$$

where b = max(0,cos(AOI)); F_b is the AOI correction for the DNI using the air-glass model of Sjerps-Koomen et al. [10]. The field-of-view of the rear solar cell is divided into 180 one-degree segments An example of one segment is shown in Fig. 2.7. For each segment the view factor of the solar cell to the ground or sky segment ($VF_{i\rightarrow k}$) is determined. $VF_{i\rightarrow k}$ is calculated with the following formula:

$$VF_{i\rightarrow k} = \frac{cos(\beta_{j-1}) - cos(\beta_j)}{2} \tag{2.11}$$

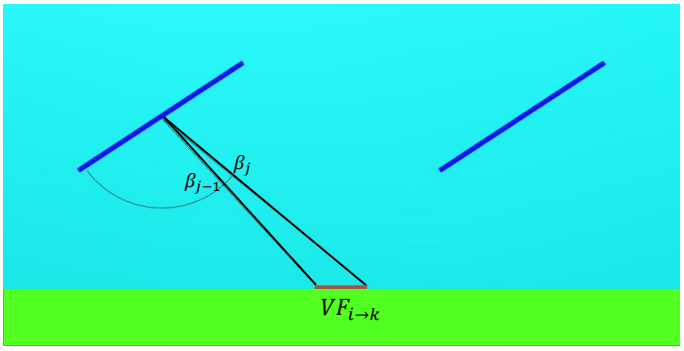

Figure 2.7: Sketch of the view factor of the ground segment to the solar module in 2 dimensions. The ground segment is indicated in brown, the solar modules are indicated in blue. The ground segment is determined by the angle of the

F_i from Eq. 2.10 is the AOI correction for the ith one-degree ground segment; and I_i is the irradiance recieved from each one-degree segment (either I_{sky}, I_{hor}, $\alpha \cdot GRI_n$, or I_{refl}).

The ground reflected irradiance on each of the ground segments ($G_{Ground,i}$) is calculated according to:

$$G_{Ground,i} = cos(90-\phi) \cdot (DNI + I_{cir}) + SVF \cdot I_{sky} \tag{2.12}$$

With $90-\phi$ being the sun's zenith angle. The ground reflected irradiance values are obtained using the Perez tilted surface model. According to Perez model the diffuse irradiance is decomposed into three components: the circumsolar (I_{cir}), the isotropic (I_{sky}), and horizontal (I_{hor}) [30]. For the horizontal ground segments the contribution from I_{hor} is considered to be insignificant and ignored [30]. SVF is the Sky View Factor of the ground surface. SVF can be interpreted as the ratio of radiation the solar module receives in comparison to the total radiation emitted by the sky's hemisphere. The SVF for the ground segments in 2D VF models is calculated with the formula:

$$SVF = \frac{cos(\beta_{s1}) - cos(\beta_{s2})}{2} \tag{2.13}$$

With β being the angle of the top and bottom corner of the solar cell, seen from the ground segments perspective. This is shown figuratively in Fig. 2.8.

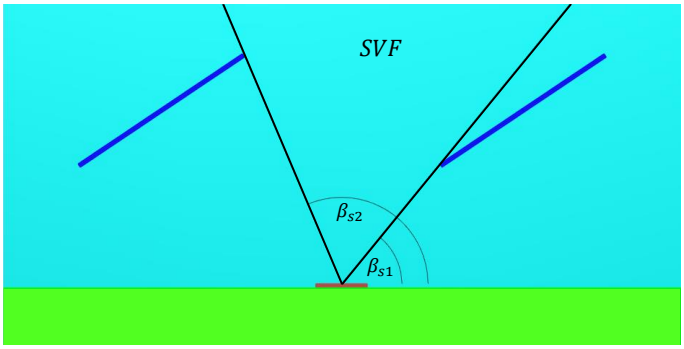

Figure 2.8: Sketch of Sky View Factor (SVF) in 2 dimensions. The ground segment is indicated in brown, the solar modules are indicated in blue. The angles for calculating the SVF of each ground segment according to equation 2.13 is also shown.

3D view factor model

The 3D view factor model that has been developed by Sandia differs from NREL's and PVSyst's in the fact that it is able to also simulate variations in back-surface irradiance on cells along the module or rows length. Different research studies [19] have shown increased backside irradiance for modules on the edges of rows. As was mentioned earlier the 2D models neglect these edge effect by assuming rows of infinite length. The 3D view factor model extends the 2D view factor model by also accounting for the module's position within the array and the lateral dimensions of the module.

The 3D view factor model calculates the back-side irradiance for each of the three components of irradiance (Direct, Diffuse and Ground-reflected), similar to Eq. 2.9. The diffuse and ground-reflected irradiance

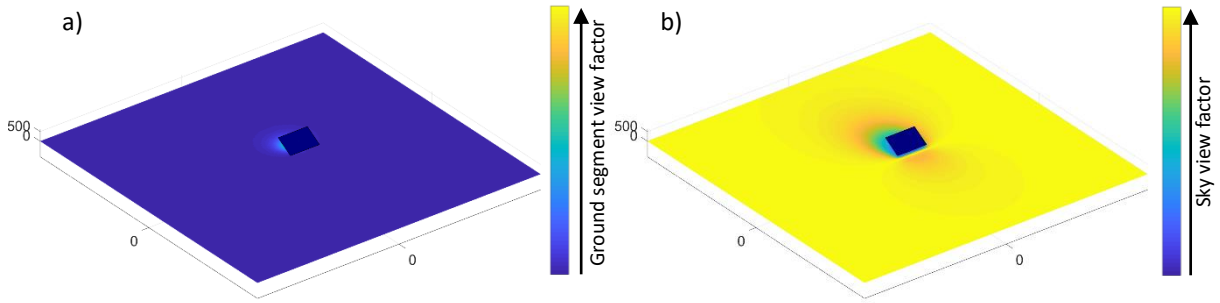

Figure 2.9: a) Sketch of $VF_{i\rightarrow k}$ of the ground cells below a solar module. Notice how ground cells behind the AOI of the solar cell have a 0 view factor. b) SVF for ground cells below a solar module. Notice how the ground cells closely below the solar module have a lower SVF compared to ground cells further away from the solar cell.

calculations are done with the help of view factors.
The direct irradiance (G_{Direct}) is calculated with the following formula [31]:

$$G_{Direct} = SF \cdot DNI \cdot cos(AOI) \tag{2.14}$$

δ is a binary value being equal to 1 if surface unshaded and 0 when shaded.

The diffuse irradiance on a solar cell can be calculated with either the Isotropic[35], Hay en Davies[36] or Perez[37] model for sky diffuse irradiance, each increasing with complexity. The simplest case being the Isotropic model, treats the sky as a uniform source of diffuse irradiance. Thus only depends on the diffuse horizontal irradiance (DHI) and the tilted angle. The Isotropic sky diffuse irradiance can be calculated with the following equation [35]:

$$G_{diff} = DHI \cdot SVF \tag{2.15}$$

The Hay&Davies model divides the sky diffuse irradiance into isotropic and circumsolar components. Next to the the surface tilt angle and diffuse horizontal irradiance, the model also uses direct normal irradiance, surface azimuth angle, extraterrestrial irradiance H_0, sun zenith angle (Z_s), and sun azimuth angle (A_s) to calculate the diffuse irrradiance the solar module recieves. The Hay&Davies sky diffuse irradiance formula can be expressed as [36]:

$$G_{diff} = DHI \cdot [R_b \cdot A + (1 - A) \cdot SVF] \tag{2.16}$$

and

$$A = DHI / H_0 \tag{2.17}$$

The Isotropic and Hay&Davies separate the isotropic, circumsolar, and horizon components explicitly. The model developed by Perez is more complex in the sence that it relies on a set of empirical coefficients for each term. The Perez sky diffuse irradiance formula can be expressed as[37]:

$$G_{diff} = DHI \cdot [(1 - F_1) \cdot SVF + F_1(\frac{a}{b}) + F_2 \cdot sin(\beta)] \tag{2.18}$$

Where F_1 and F_2 are complex empirically fitted functions that describe circumsolar and horizon brightness, respectively.

The ground reflected irradiance is calculated by first setting up a grid of cells for the ground below the module. For each ground grid (i) the irradiance impingent on the particular cell on the ground is calculated with the following formula [31]:

$$G_{Ground,i} = DHI \cdot SVF + SF \cdot DNI \cdot cos(90 - \phi) \tag{2.19}$$

SVF is the view factor of the ground cell to the unblocked sky. The irradiance a solar cell (k) receives from the ground is equal to the sum of the irradiance of the ground cell multiplied with the albedo and the view factor of the ground cell to the solar cell ($VF_{i\rightarrow k}$). This is expressed in the following formula [31]:

$$G_{Ground} = \sum_i \alpha \cdot G_{Ground,i} \cdot VF_{i\rightarrow k} \tag{2.20}$$

2.3.3. Ray tracing models

Another way of simulating the rear irradiance is with ray-tracing models. Which simulate multipath reflection and absorption of individual rays entering a scene [20]. Different ray tracing models have been developed in recent years, like Radiance [38], COMSOL [39] and LighTools [40] to name a few. The models differ in the type of ray tracing method they are based on. With four types existing [15]: forward, backwards, hybrid ray tracing, and diffuse ray tracing. Radiance uses backward/reverse ray tracing which traces rays from the image back to the light source(s). While COMSOL and LightTools use forward tracing. Forward tracing is less efficient and thus more computationally demanding because not all rays from the source(s) contribute to form the final image. However, backward ray tracing fails to recognise the optical alterations in between the source(s) and image, such as the refracting medium (lens) because it assumes large concentration of rays at the lens's surface as the source [15]. Hybrid ray tracing is a simple combination of forward and reverse ray tracing. While distributed (stochastic) ray tracing, which is also used in Radiance, is useful for simulating diffuse and reflected rays in a three-dimensional setting and scenes with extreme complexity[15]. In Fig. 2.10 the difference between forward and backward ray tracing is displayed figuratively. The figure consist of a lightsource, the sun and sky dome, and a scene consisting of a solar panel and white building. When considering forward ray tracing the rays are traced from the lightsource into the scene and collected at the interested surface. When the interested surface is the front of the solar panel, some rays are traced that never reach the interested front surface. While considering backward ray tracing the rays are traced from the interested surface into the scene till they reach a lightsource. In the following paragraphs a detailed description of a backward and forward ray tracing model will be discussed.

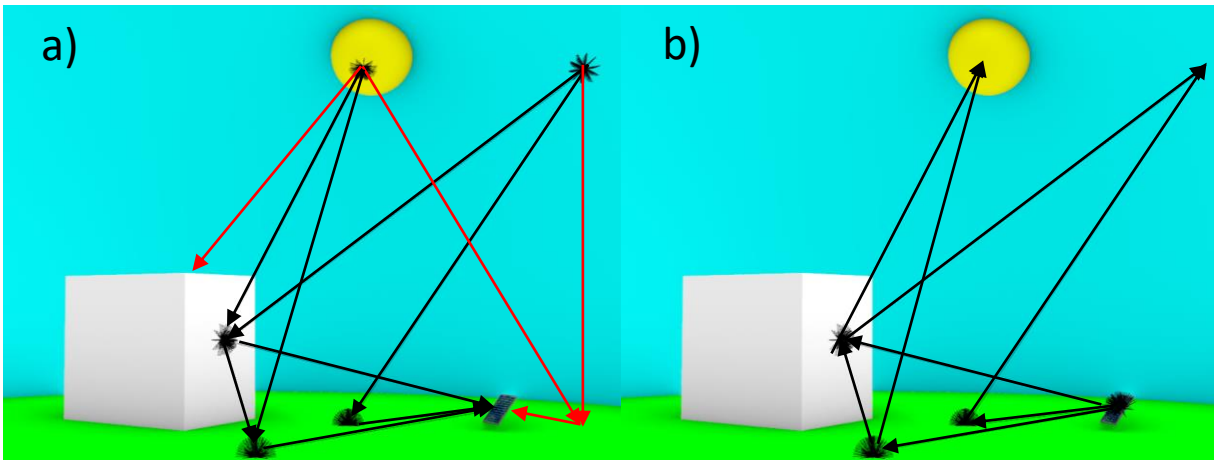

Figure 2.10: a) Illustration of forward ray tracing. Where rays are traced from the lightsources (Sun or sky dome) into the specific scene till they are fully absorbed by a specific surface. The light either reflects of a surface or gets absorbed. Forward is less efficient because a larger number of rays get traced that never reach the surface (see rays painted red) b) Illustration of backward ray tracing. Where rays are traced from a surface into the specific scene until they reach the final light source (Sun or sky dome).

Backwards ray tracing with Radiance

Among the spectrum of available ray tracing tools, Radiance is considered a state-of-the-art backward ray tracer which is based on a mixed stochastic and deterministic raytracing approach [41]. Simulation results with Radiance have been physically validated for a range of building geometries and shading devices [19, 42]. Therefore, many annual daylight simulation tools use Radiance for the global illumination calculations under a set of sky luminance distributions.

To calculate the irradiance on an arbitrary surface a test point on the surface is selected. The simulation method uses a source at the desired test point that emits rays into a half-hemisphere (2π). Rays propagate from the module towards the sky. Light, represented by rays, is followed from the point of measurement into the scene till it reaches the light source. Monte Carlo methods are commonly used to propagate a large number of possible rays to arrive at irradiance on the different surfaces in the modeled system. Different optical properties, like reflectance and transmittance for each defined surface are capable to be processed within Radiance. The surfaces composing the model are each assigned different material properties. The optical properties of the material determine how light will interact with the geometric surface. Radiance offers four classes of materials: Plastic, Metal, Transparent and Mirror.

Before the simulation starts it is important to set up the radiance parameters for simulation. An important parameter to consider is *-ab N* which sets the number of ambient bounces to N. Thus determines the maximum number of diffuse bounces computed by the indirect calculation. A value of 1 implies no indirect calculation. Another important Radiance parameter to consider is *-ad N*, with N setting the number of rays to be emitted from the test point.
Since Radiance consists of more than 100 individual sub-programs, one has to clearly define the approach used to make irradiance calculations. In this study, solar irradiation on all surfaces in an hourly resolution has been simulated with either 'gendaylit' or the 'cumulative sky' approach. Gendaylit generates an angular distribution of direct and diffuse irradiation for a given location at a certain time following the Perez luminance model [37]. For simulating cumulative irradiation over extended periods, computational efficiency can be improved at the expense of temporal resolution by using a 'cumulative sky' approach, which sums the sky irradiance over a longer duration (e.g., day, month, and even years) and runs a single ray-trace calculation for the entire period. The way the sky irradiance is summed is based on Robinson and Stone model by dividing the sky into patches [5]. Each patch gets assigned a radiance value calculated with the Perez luminance model (TMY), such that patches closer to the sun have a higher value than others. By using typical meteorological year data as input, this model can also take into consideration weather variations. It can be used to model a single hour or any period (day, month, year) by adding up every hour to create a "cumulative" sky, see Fig. 2.11.

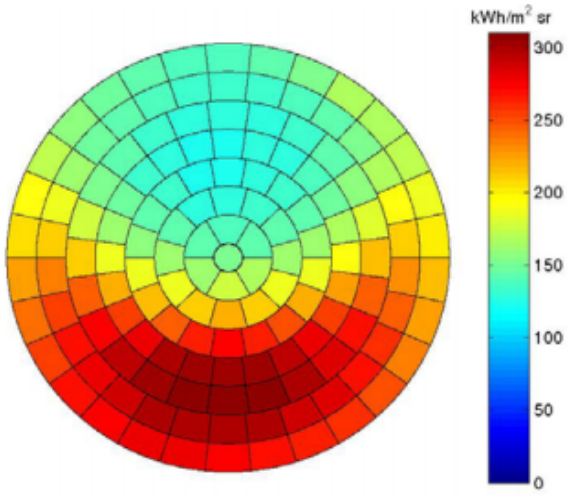

Figure 2.11: Example of cumulative diffuse sky radiance distribution for Oslo (based on 10yr mean solar data). Taken from [5]

For simplicity the plug-in DIVA (a Radiance-based tool able to include the effects of a wide variety of material types, sky and lighting conditions, and physical phenomena related to light propagation of a specific scene) within the CAD software Rhinoceros and Grasshopper was used [43]. In the CAD software Rhinoceros geometries can easily be drawn. After the designing the DIVA plug-in assigns optical properties to each geometry and translates the geometries and properties to Radiance UNIX code for simulation. Another option is using a series of Python wrapper functions called bifacial_radiance which have been developed by NREL [44].

Forward ray-tracing with Lighttools
The irradiance model that has been developed by Santbergen et. al. differs with the Radiance model in the fact that it is based on the forward ray tracing principle. This irradiance model calculates the irradiance incident on a surface by combining a so-called sky map, characterizing the irradiance conditions, with a sensitivity map, characterizing the geometry and optical properties of the PV system and its surroundings [45].
First the sky dome is split into a number of triangle sky patches. For each sky patch the sensitivity and surface area of the sky patch is calculated. While the sky map is determined by calculating the sky radiance for each of the sky patches. After calculating the sensitivity map. the total irradiance on a surface can then be calculated by integrating the product of the sky map, sensitivity map and surface areas over the whole skydome as given

by Equation:

$$G_{tot}^{M} = \int_{sky} L_{e,\Omega} \cdot S \cdot d\Omega \tag{2.21}$$

Where $L_{e,\Omega}$ (W/sr/m^2) is the sky radiance, S (-) is the sensitivity at each sky patch and $d\Omega$ (sr) is the solid angle of each sky patch. For calculation of the sensitivity map a ray tracing software is required. The ray tracing software applies the principle of tracking individual ray paths from a light source to the PV module surface for different solar hemispherical angles of incident. Each surface is assigned a optical property such as transmittance, reflectance, absorbtance etc. By simply calculating the amount of rays a certain surface has absorbed in reference to the direct normal intensity for different angles the sensitivity map can be set up. The sensitivity at each angle describes the surface sensitivity to incident light as a function of the hemisphirical angle of incidence. This is described by the formula:

$$S = \frac{P_{abs}/A_T}{1000} \tag{2.22}$$

Where P_{abs} (W) is the power absorbed on each surface after ray tracing simulation from a specific sky patch. A_T (m^2) is the area of the receiving surface. While the 1000 (W/m^2) is the reference direct normal intensity used during simulations. For a horizontal receiving surface the sensitivity (S) is simplified to cos(ω), with ω being the zenith angle of the center of each sky patch.

In Fig. 2.12 to 2.14 an example of the ray tracing process for obtaining the sensitivity map is given. Fig.

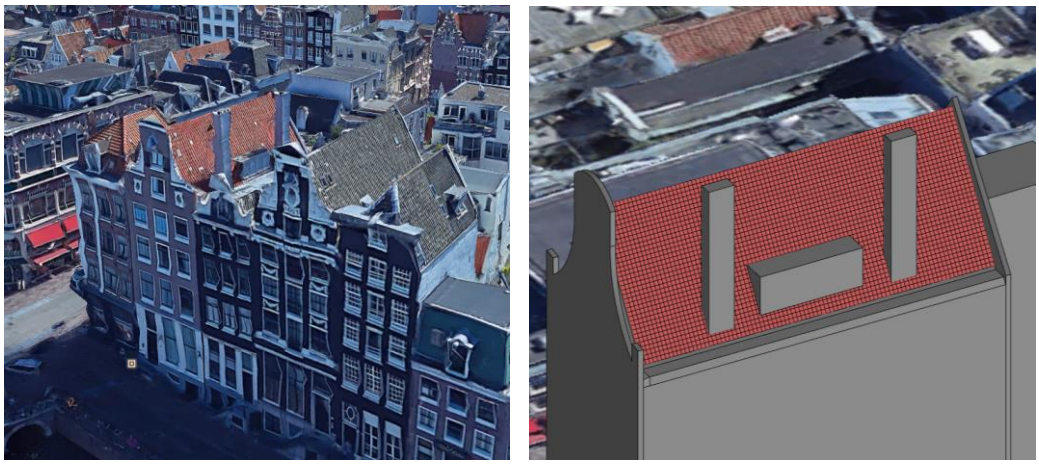

Figure 2.12: On the left an example of a corner house, of which the southeast facing roof is used as example for explaining sensitivity map. On the right a CAD design of the corner house. Picture courtesy of ir. A. Calcabrini.

2.12 shows how the scene for which the sensitivity map needs to be calculated first needs to be drawn using an CAD software. The CAD design software used within this research is Rhinoceros [46]. The design is then sequentially imported into the LightTools software for the forward ray tracing. Fig. 2.13 the ray tracing is done on the scene of the previous example. For each surface in LightTools a optical property is chosen. Example optical properties are; simple scatterer, lambertian scatterer or absorber. After the optical property of each surface is assigned the aim area needs to be defined. In the example of Fig. 2.13 the aim area is displayed. The aim area is defined as a region the rays are emitted. In the example this is a circle with a certain radius. Within this region the rays are traced originating from various positions on the sky dome. The sky dome is split evenly into sky patches and from the center of each sky patch a certain number of rays are traced aimed at the aim area. Similar to the Radiance software Monte Carlo methods are used for tracing the rays. The rays across the entire aim area are traced with a certain radiometric power, generally $1000 W/m^2$. On all the surfaces within the scene, the power absorbed term (P_{abs}) from Equation 2.22 is stored for each originating sky patch. After which the sensitivity of a certain surface for each sky patch is calculated based on Equation 2.22. In Fig. 2.14 the sensitivity map of a small section of the example roof is displayed.

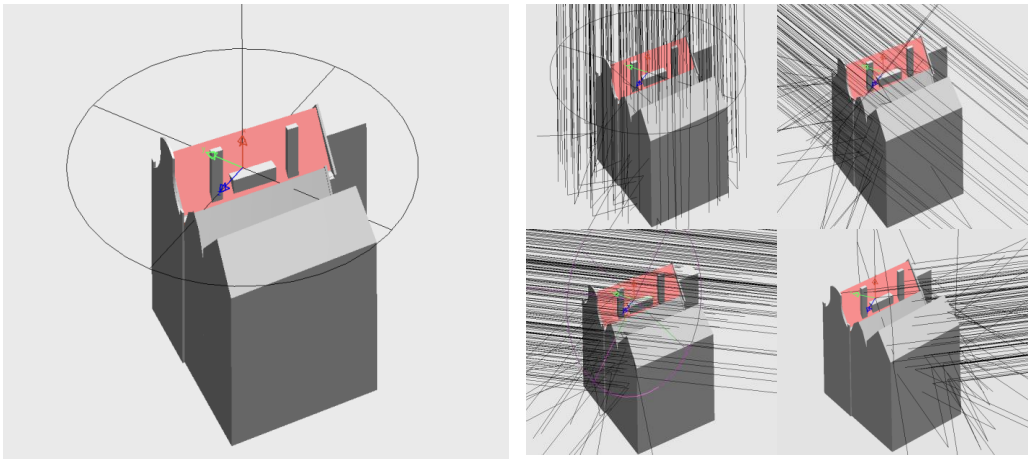

Figure 2.13: On the left an example of the aim area defined for the ray tracing simulation. On the right forward ray tracing results for rays originating from four different sky patches. Picture courtesy of ir. A. Calcabrini.

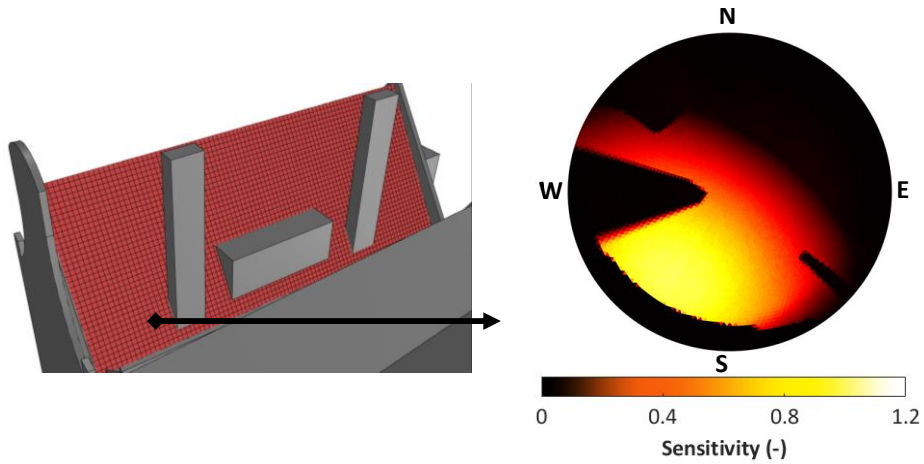

Figure 2.14: On the right the small section of the roof area that was taken for constructing the sensitivity map. On the right the sensitivity map of the small roof section that was taken. Picture courtesy of ir. A. Calcabrini.

The sky map can be calculated in a similar fashion as for the Radiance model by generating an angular distribution of direct and diffuse irradiation following the Perez model for sky luminance distribution [37]. By taking the easily measurable DNI and DHI meteorological data values, retrievable from Meteonorm for example, the luminance distribution of the circumsolar and diffuse light across the sky is calculated using the Formula 2.18 mentioned earlier. Thus is the sky map a simple representation of the irradiance distributed across the entire sky. This model relies on a set of empirically measured values obtained from empirical data from all over the world. Since hourly data for the DNI, DHI and sun position are available for many locations for a full year, this information can easily be used to create a sky map for each hour of the year. Another method of modelling the sky is the Isotropic assumption based on Equation 2.15. A isotropic sky map was created so in later chapters a fair comparison could be given between the view factor models and the ray tracing model. Since the view factor models do not consist of a luminance distribution of the sky. The isotropic sky map for the forward ray tracing was constructed by rewriting equation 2.21. For the Isotropic sky assumption it is known that the sky radiance term ($L_{e,\Omega}$) is constant and is taken out of the integral. The equation to solve than becomes:

$$L_{e,\Omega} = \frac{G^M_{tot}}{\int_{sky} S \cdot d\Omega} \tag{2.23}$$

Since it is known that for a horizontal surface the sensitivity (S) is simplified to $\cos(\omega)$ and the integral of the solid angle of each sky patch ($d\Omega$) becomes 2π the sky radiance ($L_{e,\Omega}$) of each sky patch can be calculated

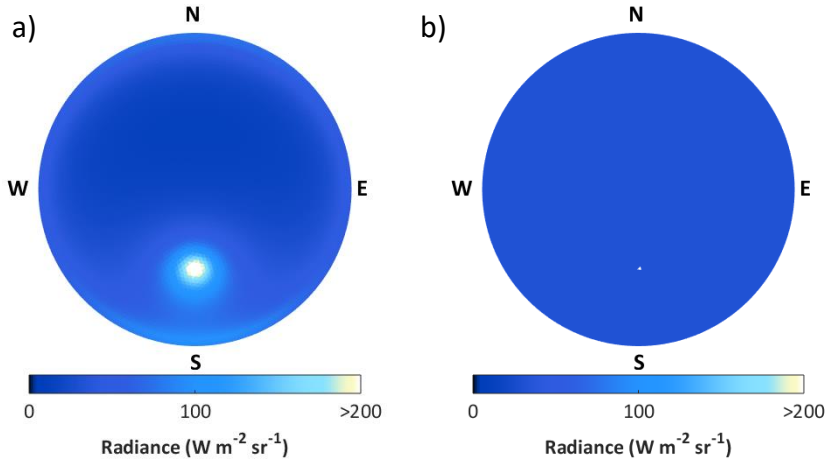

Figure 2.15: Example of luminance distribution and Isotropic sky map. For the situation the sun at 45 and 180 degree altitude and azimuth respectfully. And a DHI and DNI value of 100 and 800 W/m^2 respectfully.

with the formula:

$$L_{e,\Omega} = \frac{DHI}{\pi} + \delta \cdot \frac{DNI}{d\Omega} \tag{2.24}$$

With δ a binary value having the value one when the sun position is at a particular sky patch and zero other wise. In Figure 2.15 an example of the difference between an Perez luminance distribution and a Isotropic sky map is given.

2.4. Urban environment

2.4.1. Energy use build environment

Next to transport and industry, the build environment is the biggest end-consumer of energy worldwide, responsible for around 40% of the total energy consumption in Europe [16]. Most of the consumed energy in buildings is used to heat-up and cool down the building. Another major energy share is consumed by lighting, water heating or other electrical equipment. Today most of the required energy is produced from fossil fuel sources such as coal, gas and oil. The burning of fossil fuels however raises serious environmental concerns since greenhouse gas carbon dioxide (CO_2) are emitted as a byproduct. This greenhouse gas increases radiative forcing and contributes to global warming and climate change.

2.4.2. Potential of building façades

Improved energy performance regulations and laws for buildings where set up to mitigate climate change partly caused by the energy consumption of the building sector. An improved efficiency can be obtained through energy efficiency measures and by implementing renewables such as solar energy. The energy performance in buildings directive will enter into force in 2020 and might become an important driver of PV development in the building sector by pushing PV as the main possibility to reduce the net energy consumption in buildings after energy efficiency [47]. It is expected that the measures will lead to a significant growth of solar energy in the building sector. Not just the Building Applied Photovoltaics (BAPV) but also the Building Integrated Photovoltaics (BIPV) market. For BAPV the PV modules are added to the original structure for example on top of the roof, while BIPV the PV modules are integrated within the structure and becomes more part of the architectural concept and a replacement for conventional building materials. Two main application areas for BAPV and BIPV can be classified[6]: roof and façades. The roof application area can be categorized in the following subcategories[6]: Solar tiles, Full roof solution, Mounting structure, Skylight, Prefabricated system and a Lightweight system. The façade application area, described in a little more detail, can be categorized in the following subcategories [6]:

- Mounting structure, with PV modules installed as a façade cladding through a mounting system not specifically developed for the building skin technological units.
- Warm façade, a continuous building envelope system in which the outer walls are non-structural. A

curtain wall fulfills all building envelope requirements such as load bearing, thermal insulation, weatherproofing and noise insulation.

- Cold façade, consisting of a load-bearing sub-frame, an air gap and a cladding panel. They are “cold” because, during hot weather, the heat from the sun is dissipated through the naturally ventilated air cavity, bringing a cooling effect for the wall and for the PV modules
- Lightweight, a product whose weight per square meter is significantly lower than conventional products which are usually based on glass.
- Solar glazing, glazed PV laminates for windows. Combining glass-glass PV laminates with adjustable light transmission, stimulating the architectural design of light and shadow and performing a fundamental role for the energy balance of the building.
- Accesories, PV modules integrated in for example balconies, parapets, outdoor partitions, shading systems or other elements. With shading systems the most commonly used accessory.

An example of each system is displayed in Fig. 2.16. For the mounting and prefab system the roof variant is displayed but a similar concept can be thought of for the façade variant.

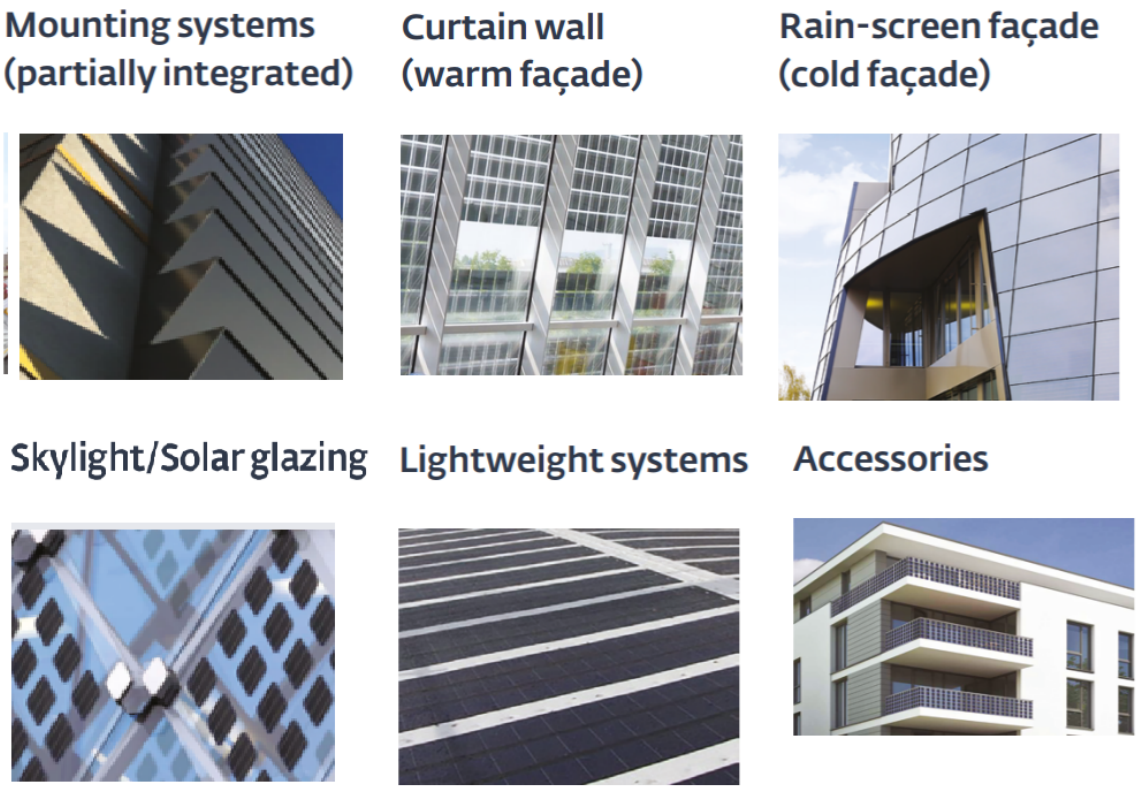

Figure 2.16: Overview of the subcategories of façade BIPV subcategories. Adapted from [6]

Currently in both the BAPV and BIPV market roof products are dominating. But due to the increasing requirements regarding energy efficiency in buildings mentioned earlier a growth of PV applications in the façade segment is expected. Since many buildings simply do not have enough roof area to meet the nearly zero-energy performance standards. Thus will start adding or integrating PV modules into (existing) structures such as façades and windows to generate enough energy. Because the PV can act as a substitute for traditional materials in façade systems [6]. Especially in the BIPV it can already be noticed that the difference in shares of roof and façade application is becoming less significant with façade application accounting for around 44% of total market share[6] while roof system accounts for the rest. The most common roof product group still being roof solar tiles (24%) followed by the full roof solution (15%) [6]. While for the façade application the most common product group is the cold façade (13%) followed by solar glazing/skylight (12%) [6].

Previously building façades in urban environments and it's potential for solar PV application has been often disregarded. This is also why only a few studies have included the potential for photovoltaic installations on building façades in their scope so far [7, 8, 48, 49]. However the interesting study conducted by K. Fath et. al. shows that for a typical 2 km^2 urban area that has been researched, building façade's provide almost triple the area of building roofs [7]. The research is conducted with a 3D model of Karlsruhe a typical German city located in the State of Baden-Wüirttember, displayed in Fig. 2.17. The model was used to estimate the economic potential of (building-integrated) photovoltaics for the a typical urban environment. The definition of economic potential is the share of technical potential currently economically exploitable from a building owner's point of view, i.e. considering actual system prices, electricity tariffs and the expected system lifetime [7].

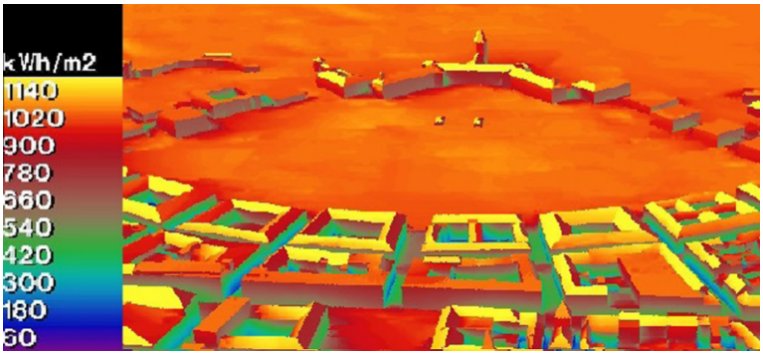

Figure 2.17: 3D city model of the city of Karlsruhe Used by K. Fath et.al. for predicting the economic potential of roof and façade PV application in urban areas. Taken from [7]

In total the façades in Karlsruhe receive about 41% of the total irradiation. However compared to most roof-tops many façades suffer greatly from non-optimal inclination and orientation. This can be seen in the Fig. 2.18 below.

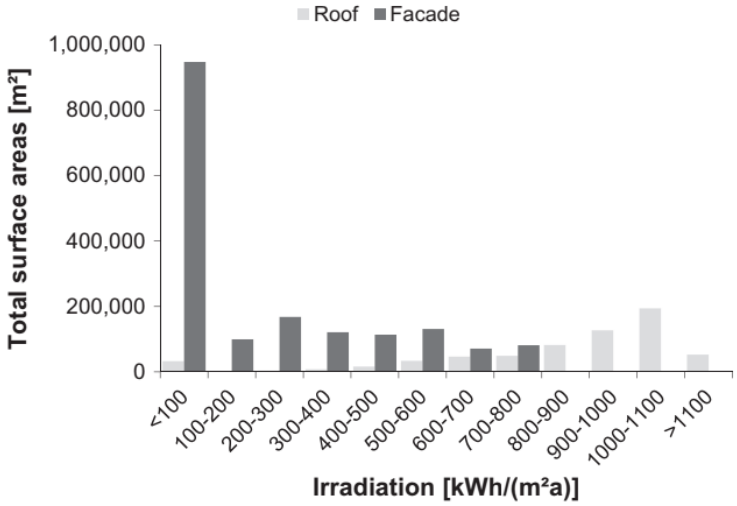

Figure 2.18: Distribution of surface areas according to irradiation class for roofs and façade within the city of Karlsruhe. Taken from [7]

Still under present market conditions and considering further a material substitution from the building integration of the photovoltaic installations, it was established that an economic potential of up to 56 MWp or 0.4 km^2 results, of which up to 6 MWp or 0.04 km^2 are currently economically installable on building façades [7]. Thus façades-mounted installations accounting for 13% of the economic potential. This study was conducted with the software Radiance, a backward ray-tracing software described above. A similar study was conducted by C. Catita et. al. and followed by P. Redweik et.al. for a case study of the Campus of the University of Lisbon, with the total annual solar irradiation on each calculated surface shown in Fig. 2.19.

This study however is based on a different approach for calculating the irradiance on a façade. Namely,

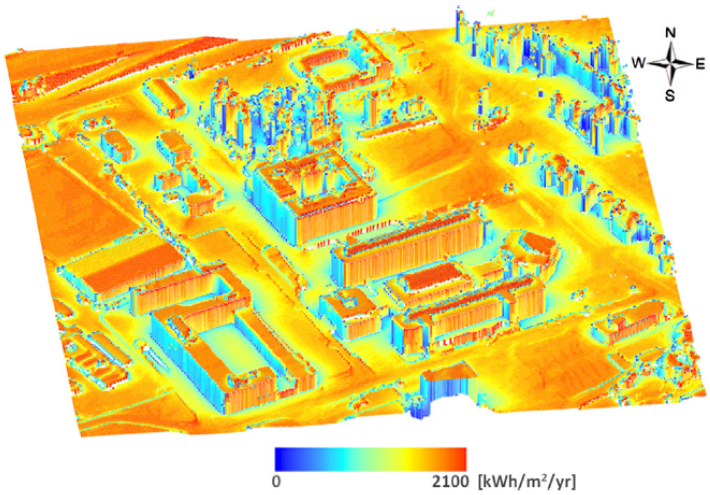

Figure 2.19: Calculated total annual solar irradiation on each surface for 3D Urban model for the Campus of the University of Lisbon. Taken from [8]

building a digital surface model (DSM) of the urban region built from LiDAR data and a solar radiation model based on climatic observations. A shadow algorithm developed in order to calculate shadow maps and sky view factor both for roofs and facades at once. So lastly direct and diffuse solar radiation can be obtained for each point on the ground, roof and façade's [8]. Also for this study it was observed that the irradiation reaching facades is lower than that of the roofs, but due to the large areas concerned, facades have a significant impact on the solar potential of buildings in an urban area [8, 48]. Both the studies only consider if the irradiance where to fall on the front side of the module, but did not investigate if instead of regular monofacial modules a bifacial PV module would be integrated. Also as mentioned different simulation methods where used in the studies, one based on Ray-tracing method while the other is based on a view factor method. It is not mentioned why a particular method is chosen, what the benefits are of the particular method and if this method also holds for simulation of the potential of a bifacial PV systems.

3

Simple comparison of different existing bifacial rear irradiance model implementations

In this chapter, the different simulation models that where previously discussed will be compared on their simulation time and accuracy. First, the simulation setup and the meteorological data used for the simulation is discussed. Followed by a discussion of the simple comparison simulation results when simulating the rear irradiance on a single bifacial module under free horizon conditions. Lastly, the difference in modelling urban landscapes compared to simple free horizon is discussed.

3.1. Simulation setup

Large scale deployment of (bifacial) PV modules requires the development of both fast and accurate simulations tools. In the previous chapter different simulation models where categorized and their underlying principles described. The different models are compared on their simulation time and accuracy. The simulation time is measured by the computer when simulating a single bifacial module under free horizon conditions, with fixed values for the variables: tilt, azimuth, stand-of-height, cell-spacing and albedo. For the simulation time measurements the following default values are taken. Namely, a stand-off height equal to 0.5 m, albedo equal to 0.25, tilt equal to 30^o, and cell spacing equal to 0 mm. The PV module and its default values are displayed in Fig. 3.1.

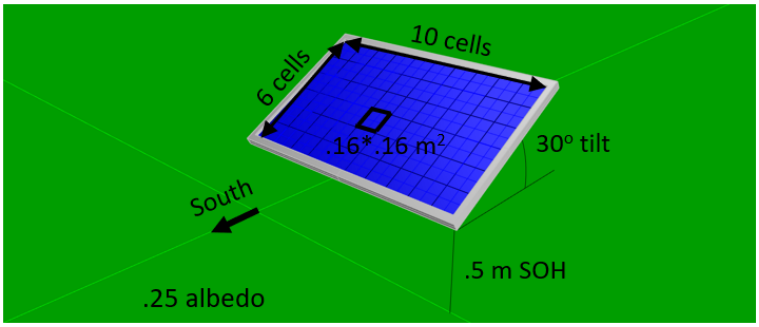

Figure 3.1: Sketch showing the default simulation input parameters that where considered. The solar module consisted of 60 cells. Each cell having and 0.158·0.158 m width and height respectifully. The solar module is orientated towards the south with an 30 degree tilt and having an .5 meter stand off height. The albedo of the ground was taken taken to be 0.25.

To make a comparison of the sensitivity and accuracy of the models for the variables, simulations are performed with the models for varying input parameters. Each of the default values of the simulation time measurements earlier are varied and the total rear irradiation is calculated. The varying variable values are displayed figuratively in Fig. 3.2.

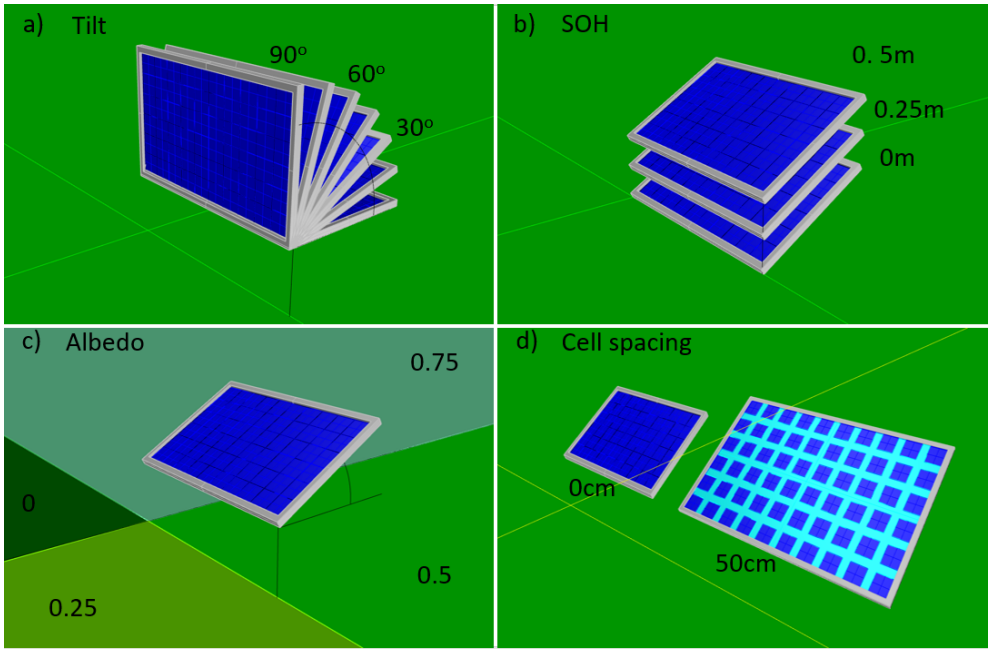

Figure 3.2: Sketch showing the varied input parameters that where considered for the sensitivity and accuracy simulation setup. The input parameters that where varied where a) Tilt b) Stand off height. c) Albedo d) Cell spacing.

For the empirical model the ϕ_{mpp} and the η is taken equal too 100% and 0% respectively. Since the empirical models are simplified analytical approximations expressed within a single formula the simulation time is not measured since this is much faster compared to the other simulation models.

3.2. Meteorological data

Each simulation model requires meteorological data as input for the rear irradiance calculations e.g. DNI, DHI, GHI. Meteorological data for a particular location can be obtained from different sources. Such as Koninklijk Nederlands meteorologisch instituut (KNMI), Meteonorm, Dutch PV Portal, NASA and PVGIS. Besides DNI and DHI measurements also consist of measurements for the wind speed, wind direction, temperature, solar irradiation, the amount of mist and several other relevant weather parameters. In this chapter Meteonorm is used. This data is available on most populated areas on the world and consist of all relevant hourly data for PV simulation. There are different ways of obtaining the meteorological data. Meteonorm for example uses ground stations, aerosols and satellites to obtain the data. The meteorological data is based upon average data of the past. For example, the average of the years 1995-2005 is taken. The irradiance might change from one year to another, but when looking at an average of 10 years, the differences are small since the climate does not change in such a short amount of time. For consistency for each simulation model the same input data of DHI and DNI is used. The data that is collected is from Meteonorm is of the e-bike location in Delft.

3.3. Free horizon simulation

3.3.1. Accuracy and sensitivity evaluation for different rear irradiance models

When comparing the different simulation models it is important to consider both the accuracy and the simulation time of the different models. For simplicity the models only a free horizon condition is considered. For each of the models the yearly total back-side irradiance is calculated for a single bifacial PV rear-side. Since the most important variables for a single module are tilt, stand-off-height, albedo and cell-spacing these parameters will be varied to investigate whether the models also consider each variable.
The default values are: south-facing front side, a 0.5 m stand-off-height, albedo of 0.25, 30^o tilt and 0 mm cell spacing, as sketched in Fig. 3.1. Each of these variables are varied as was shown in Fig. 3.2. The results of the simulations are displayed in Fig. 3.3 below.
From the figure three interesting differences can be noticed. Firstly, the 3D view factor model, the LightTools

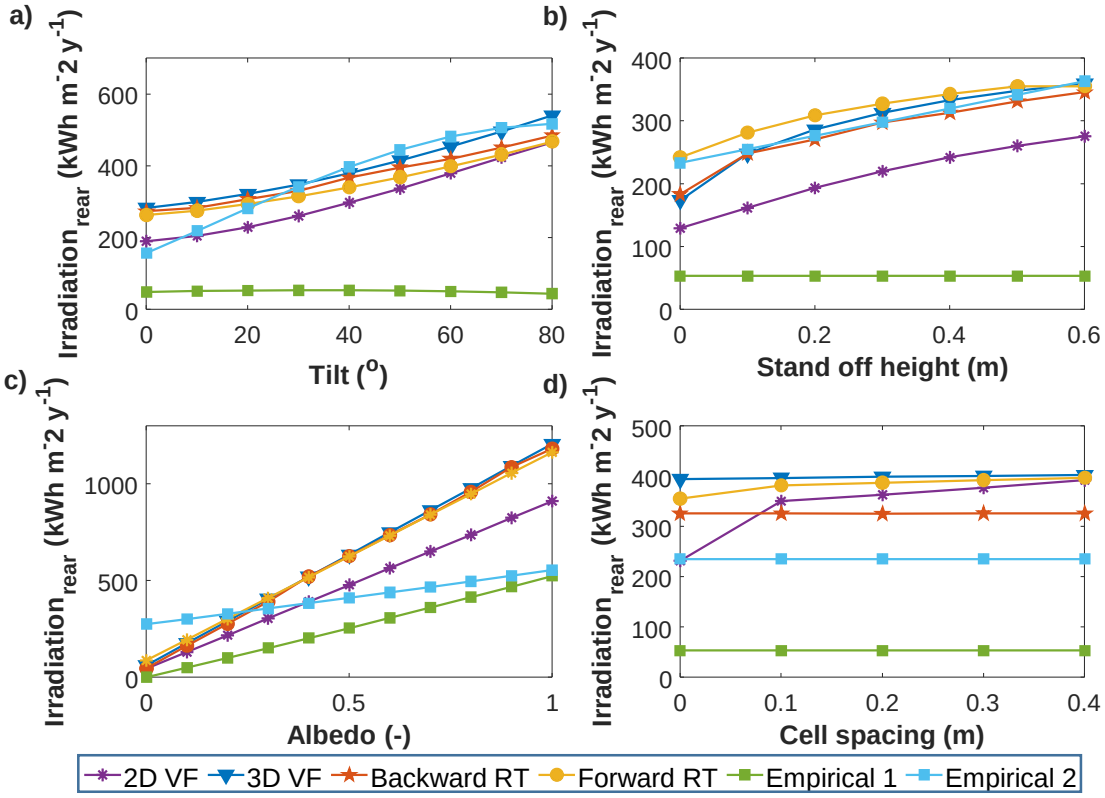

Figure 3.3: Yearly back-side irradiance comparison for single bifacial PV rear-side irradiance models, varying module tilt, module height, ground albedo and cell spacing, for Delft e-bike location. Default values (when not varied) are stand-off-height = 0.5, albedo = 0.25, tilt = 30^o, and cell spacing = 0 mm. For the empirical model the ϕ_{Pmpp} is taken equal too 100% and η equal too 0%.

and the Radiance model show a similar trend and closely predict the yearly irradiance for all the variables considered. There is a positive relation between the variables and the yearly rear-side irradiation. When increasing the tilt, stand-off-height, albedo and cell-spacing also an increase in the total irradiation on the back can be noticed.

The rear irradiation is mostly affected by self-shade on the ground from the modules themselves and the portion of the sky that's visible [50]. By changing the variables the self-shading and visible sky changes somehow affecting the yearly rear irradiance. The differences between the predicted values of the three models is mostly due to the accuracy setting chosen of each model. For each model a moderate accuracy setting was chosen instead of the highest accuracy setting since the highest accuracy setting can result in very long simulations. This will be discussed in more detail in the next paragraph. For the LightTools forward ray tracing the chosen settings are: sky subdivision in 640 sky patches and an total number of rays of 20 million. The settings for the Radiance backward ray tracing are: 10 thousand rays and 8 ambient bounces. Lastly, for the 3D VF model each ground segment is 1/4 the size of the solar cells.

Another observation is that the 2D view factor model shows a similar trend as the 3D view factor model, but predicts a lower yearly irradiance compared to the 3D view factor model. The main reason for this is that the 2D view factor model assumes rows of infinite extend in order to not suffer from additional complexity and computation time. Research simulations [19] have shown an increased backside irradiance for modules on the edges of rows. The edge effects become more and more negligible for larger rows, for a single bifacial PV module however these variations are still considerable as the figure shows. For the earlier simulations a single bifacial module is simulated, explaining why the 2D view factor models predictions are lower compared to the 3D view factor and ray tracing models.

Lastly, from Fig. 3.3 a), b), c), or d) it can also be noticed that a difference can be observed between the predictions made by the empirical models and the rest of the models. The first empirical model is still able to accurately predict the yearly irradiance for a varying tilt, stand-off height and to some extend albedo. This is not surprising since this model is only intended to cover a limited range of installation conditions. Only covering the conditions and measurements from which the model was fitted. Under different conditionds

the empirical models are rendered useless. This is especially the case for the second empirical model which only depends on the ground cover ratio and normalized clearance height (stand-off-height divided over the row spacing). Single a single bifacial module was simulated the irradiance predictions made under varying tilt, stand-off-height, albedo and cell-spacing are totally unsuited.
In the Fig. 3.4 the cell spacing was additionally considered for a stand-off height of a 100 mm and compared with the measurement taken for the stand-off height of 500 mm from the default simulations mentioned earlier. When considering the cell spacing under the default values (at a stand-off-height of 500 mm) it can be seen that the yearly back-side irradiance is nearly constant for all the rear-irradiance models. While this could suggest the irradiance does not depend on the cell-spacing, this not necessarily always the case. For example when varying the stand-off height of the bifacial PV system. It can be seen that a smaller stand-off height the cell-spacing has a higher influence on the total yearly irradiation. This relationship is also researched and supported in literature [50]. Some literature even suggest that with sufficient stand-off height (e.g., > 1 m), the total yearly rear irradiance is only slightly affected by the cell spacing and the module transparent area [50].

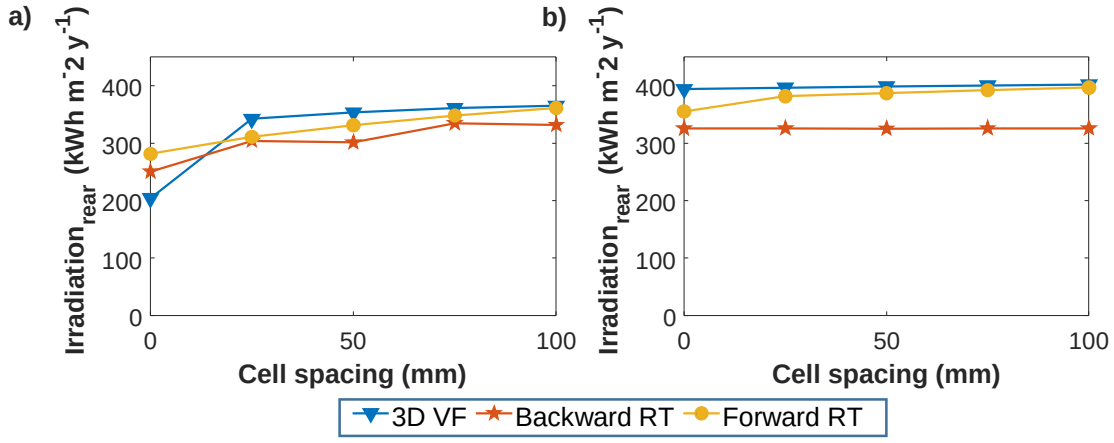

Figure 3.4: Yearly back-side irradiance measured for varying cell spacing with a) 100 mm and b) 500 mm stand-off height simulated with the 3D VF, forward and backward ray tracing models.

3.3.2. Simulation time evaluation for different rear irradiance models

The best suited models for accurately simulating the rear-irradiance of a single bifacial module under free horizon conditions are the 3D view factor, the forward and the backward models. One important difference between these models is the simulation time, which will be discussed in this paragraph. The different models depend on certain 'accuracy parameters' which can be selected for the simulation. Varying the different parameters not only changes the accuracy setting of the simulation but it also affects the simulation time. Hereby, the most important accuracy parameter for each of the earlier mentioned best suited simulation models will be discussed.

For forward ray tracing in LightTools the most important accuracy parameters are the number of rays to be traced and the number of sky patches the hemisphere is divided into for setting up the sensitivity map (see previous chapter). The ray distribution in the forward ray tracing is done by the Monte-Carlo method with a certain randomness. For an accurate simulation, the ray density over a certain aim area needs to be high enough to ensure an evenly ray distribution for different simulations. The relative error (RE) of the simulation is defined based on the power absorbed by a given surface, simulated using 10 different seed values (P_{seed}). The relative error can be calculated with the following formula:

$$RE[\%] = \frac{\sigma_{Pseed}}{\overline{P_{seed}}} \cdot 100\% \tag{3.1}$$

Where σ_{Pseed} is the standard deviation (STD) and $\overline{P_{seed}}$ is the average power absorbed. In Fig. 3.5 below on the left the calculated relative error for a single module placed horizontal on top of an ground patch with a 2m radius is displayed under different total number of rays including the simulation time calculated for each sky

patch. For the simulation an aim area of 2 meter radius was taken similar as the ground below. Additionally the total simulation for the simulation of 640, 2560 and 10240 sky patches is displayed on the right.
For a single horizontal module the relative error and simulation time seems tolerable. However considering the irradiance on the rear-side of a bifacial module is mostly reflected originating off large (ground) surfaces, the aim area for the simulation also needs to cover large area that reflects irradiance onto the rear. While the simulation of a ray density over a small aim area is reasonably fast as was shown in the figure earlier, for a large aim area a greater number of rays is needed to ensure the same ray density which leads to longer simulations.

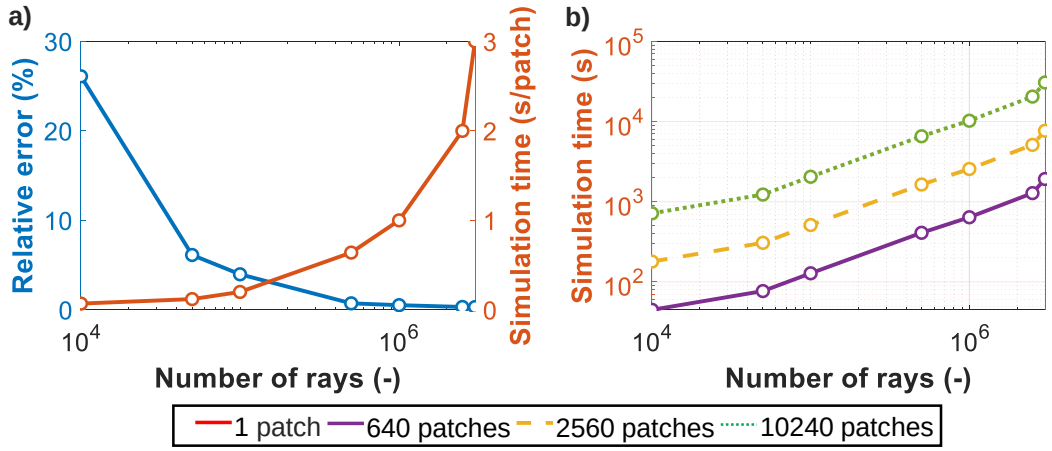

Figure 3.5: Left: Relative error and simulation time for a single module placed flat on top of an ground patch with a 2m radius simulated per sky patch. Right: Total simulation time when 640, 2560 and 10240 sky patches are considered.

The backward ray tracing simulations in Radiance depend on a number of parameters. In Table 3.1 the most important parameters for irradiance simulation in Radiance, including a list of useful ranges categorized from fast, accurate and very accurate is given. This table was provided in Axel Jacob's Radiance tutorial [10]. The ambient bounces parameter sets the number of ambient bounces to consider in the simulation. This is

Parameter	Abbreviation	Min	Fast	Accurate	Very Accurate
ambient bounces	-ab	0	0	2	8
ambient accuracy	-aa	.5	.2	.15	0
ambient resolution	-ar	8	32	128	0
ambient divisions	-ad	0	32	512	4096
ambient super-samples	-as	0	32	256	1024

Table 3.1: List of useful ranges of Radiance parameters categorized as fast, accurate and very accurate. Provided by Axel Jacob's Radiance tutorial [10].

the maximum number of diffuse bounces computed by the indirect calculation. A value of zero implies no indirect calculation. The parameter ambient resolution determines the maximum density of ambient values used in interpolation. Error will start to increase on surfaces spaced closer than the scene size divided by the ambient resolution. The maximum ambient value density is the scene size times the ambient accuracy (see the ambient accuracy option below) divided by the ambient resolution. The ambient accuracy sets the value which approximately equals the error from indirect illuminance interpolation. A value of zero implies no interpolation. The ambient divisions sets the number of rays and determines the error in the Monte Carlo calculation of indirect illuminance to be inversely proportional to the square root of the value inserted. A value of zero implies no indirect calculation. Lastly the ambient super-samples sets the number of ambient super-samples to apply only to the ambient divisions which show a significant change [51]. Similar to the forward ray tracing model, also within the Radiance software the rays are traced by the Monte-Carlo method. So also for Radiance the number of rays to be traced is important too ensure a high ray density for accurate simulations. While increasing the number of rays will result in an increase in simulation time, the simulation time is faster compared to the forward ray tracing model since the Radiance software is based on the more

efficient backward ray-tracing. For both LightTools and Radiance models 2 % is considered an acceptable relative error value. For the comparison only the ambient divisions and ambient super-samples was changed while the other parameters where left on the very accurate settings of the table above. For the simulations the ambient super-samples was put at half the ambient division setting as was suggested in [10].

The 3D view factor model does not depend on any random parameters, however it does contain certain parameters that can influence the accuracy of the simulation. The two most influential parameters when considering a free horizon simulation is the size of the entire ground surface to be considered and a segment ratio determining the size of the ground grid segment in relation to the solar cell [31]. During the rear irradiance the ground below the receiving solar cell for computational efficiency is split in segments. Each grid-cell reflects irradiance onto the rear of the solar cell based on the view factor Equation 2.8. The cell dimensions and grid boundary lead to an certain approximation error. In [31] a rough rule was set, putting the cell ratio to 1/4 the size of an solar cell in order to maintain a approximation error < 1%. And the grid boundaries set at an angle of 88^o from the cell's center to the ground below. This ensures the resulting grid encompasses 97% or more of the ground-reflected irradiance which might affect a receiving cell [31]. For consistency the same grid boundary is also used for the simulations performed in LightTools and Radiance.

In order to investigate the difference in simulation time between the three different software's mentioned above under free horizon conditions the following input variables where used: stand-off-height = 0.1 m, albedo = 0.25, tilt = 30^o and cell spacing = 0 mm, as shown in Fig. 3.1. For the ray tracing models the number of rays was increased until an acceptable relative error value for the simulation was reached below 2 %. And for the 3D view factor model the simulation was performed for a cell ratio of 1, 1/2, 1/3 and 1/4. In the Fig. 3.6 the resulting simulation times are given for the LightTools, Radiance and 3D view factor simulations.

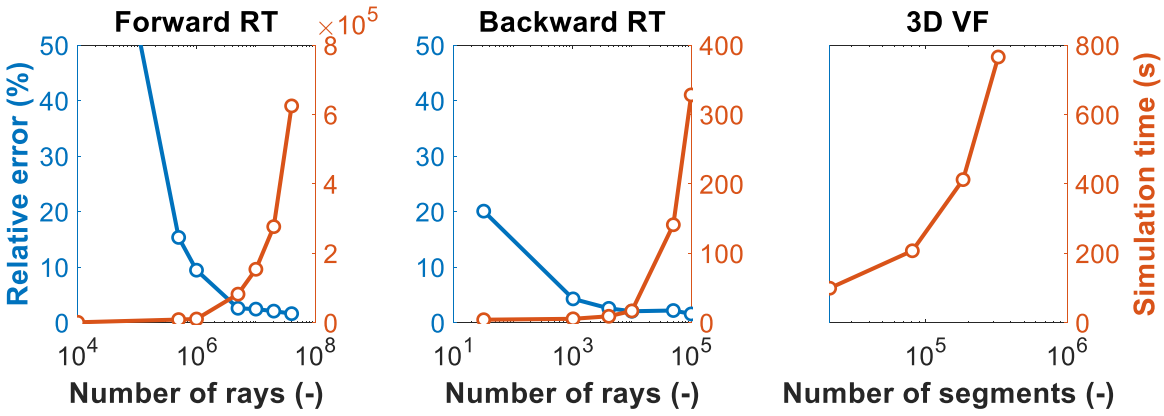

Figure 3.6: Resulting simulation times for simulation of single bifacial PV model under free horizon conditions performed with LightTools, Radiance and 3D view factor models.

The figure shows for each simulation model how increasing accuracy is at the expense of simulation time. Between the simulation tools the Radiance model performs the best, followed by the 3D view factor model and lastly by the LightTools model. Remarkably the Radiance model however requires a much higher number of rays compared to the suggested settings from the table above to ensure a < 2% relative error. These simulations where performed for free horizon conditions. How the different models perform within urban environments will be discussed in the next Chapter.
It should be noted that the Radiance simulations require a single ray trace simulation using the 'gendaylit' (for irradiance simulations) or the 'gencumsky' (for irradiation simulations) method described in Chapter 2. If time of use (TOU) needs to be simulated, for each time instance a different ray tracing simulation is required. The forward ray tracing and 3D VF implementation only require a single ray tracing (for setting up the sensitivity map) or view factor calculation (SVF and $VF_{i\rightarrow k}$) that are reused for each time instance. Only the shading factor (SF) and sky map of the 3D VF and forward ray tracing respectively needs to be calculated for each time instance. For this reason the simulation time increases for the backward ray tracing model when time of use (TOU) simulations are required. While it only slightly increases for the 3D VF models and the forward ray tracing model.

3.4. Discussion chapter

The different models available for simulating rear irradiance differ in input variables considered, simulation time and accuracy of predictions. Earlier in the chapter it was shown how even in free horizon the empirical model can result in inaccurate predictions since not all variables affecting rear irradiance are considered. Only the 3D VF, the backward and forward ray tracing methods fulfill all the requirements to simulate the back side irradiance/irradiation when the aim is to perform simulations in more complex urban environments.
Out of the existing simulation models tested, the backward ray tracing model Radiance was considered the fastest simulation tool for modeling yearly irradiation or a single irradiance measurement incident under free horizon conditions. Time of use (TOU) simulations however results in longer simulation time for the backward, while the 3D VF and forward ray tracing models stay relatively the same.
Sandia National Laboratory's 3D VF model implementation it suited for free horizon only. The required view factors can also be calculated with the ray casting method [52]. This method is implemented and discussed in the following chapters.

4

Modelling and validation of new VF based irradiance model for bifacial PV application

This chapter aims to develop a comprehensive and flexible irradiance model capable of simulating the front and rear side of a bifacial PV module. As was mentioned in the previous Chapter, the model should be able to fast and accurately calculate the irradiance distribution on the rear side of the bifacial PV module even in dense urban settings. Especially the reflected irradiance reaching for example the rear surface of a bifacial module has to be included. This is done by first, explaining how an urban environment is modeled with the different model frameworks. Followed by a description of a newly developed model working principle. And lastly, performing a series of sanity checks to explain potential shortcomings.

4.1. Free horizon to urban landscapes

Before the performance of the different rear irradiance models can be determined for urban landscapes the performance was first tested for a simple free horizon. This paragraph first explains what the difference between a free horizon and more complex urban landscapes is. And secondly, how this is implemented within each existing model.

Free horizon is the simple case where the direct and diffuse irradiance from the skydome is not blocked by any object, close or nearby the PV module or a solar cell. This is the case for example within an open field or on the ocean. For PV operation this is an ideal situation because the maximum irradiance can be collected without any of the negative effects caused by shading. However many application areas are non-ideal and suffer from a type of obstruction either far away or nearby. Typical examples of obstructions causing shading are, for example, trees, buildings, chimneys, etc. Especially within urban environment a PV module can be subjected to many obstructions, that block the direct/diffuse incident irradiance, and causes shading on the module/solar cells. Shading can have many negative effects on a PV solar cell/module/system. A distinction can be made between a fully shaded and partially shaded PV solar module/cell. At the PV module level the main negative effect of a fully shaded module is that it produces less than optimal power because it does not receive direct radiation from the sun, but only diffuse radiation from the skydome. The fully shaded module can however also have a negative effect for the entire system because in many PV systems the PV modules consist of several PV modules that are wired together into a series circuit. And when the power output of a single module is significantly reduced, the power output for the whole system in the series is reduced to the level of current passing through the weakest module. This is also true when a PV module or solar cell is partially shaded because within the PV module many solar cells are wired together into a series circuit. And the partially shaded module/solar cell can similarly negatively affect the entire module and system. This is why most PV modules have diodes that allow the current to flow through an alternative path when enough cells are shaded (or damaged). These bypass diodes allow the series-connected solar cells to continue supplying power at a reduced voltage rather than no power at all.

How obstructions and shading are modeled varies for the view factor and ray-tracing models. While in the previous chapter the theoretical working principle of the different models was explained, this chapter will give special attention to the difference in how obstructions are modeled in the view factor and ray-tracing models. Since this is important for simulating the urban environment. First, the view factor model is con-

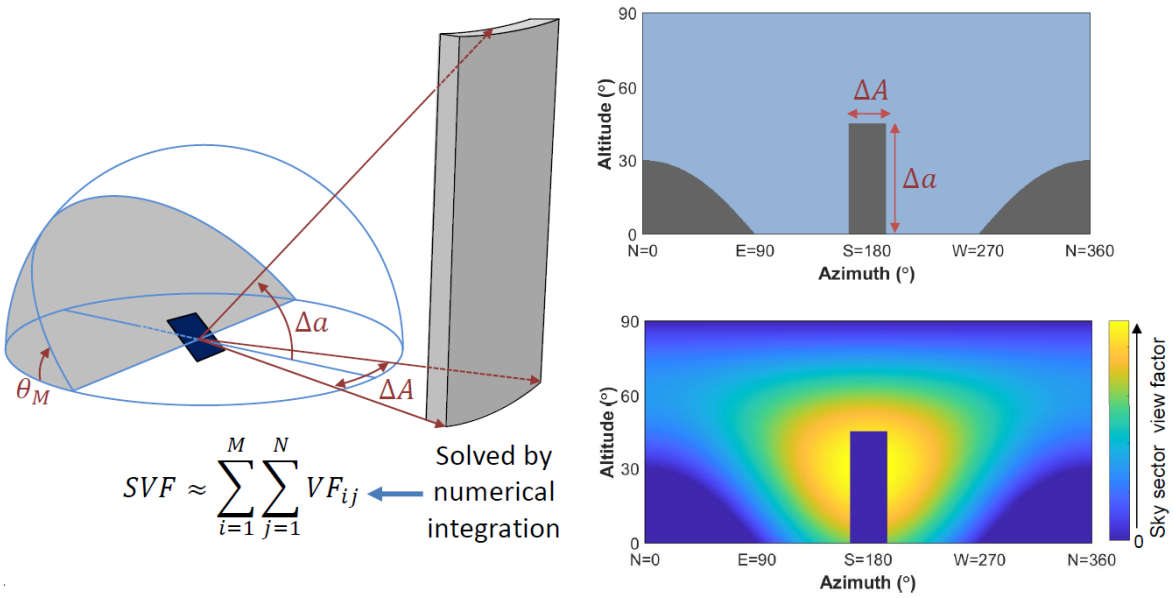

Figure 4.1: Decription of Sky View Factor calculation with skyline profile. Taken from [9]

sidered. For the view factor models the obstructions and their effect are considered through the Sky View Factor (for diffuse irradiance component) and the Shading Factor (for direct irradiance component). A Sky View Factor (SVF) represents the ratio at a point in space between the visible sky and a hemisphere centered over the analyzed location. The hemisphere is divided into different patches. Each patch in the visible sky's hemisphere is given a value that quantifies the fraction of diffuse irradiance that arrives at the solar cell calculated with the view factor principle. So when the entire hemisphere is unobstructed the summed Sky View Factor of all the patches is equal to 1 and when fully blocked it is equal to 0. However, when only a certain patch in the sky's hemisphere is blocked by an obstruction the Sky View Factor of this patch is set equal to 0. How this is done in practice is by setting up a skyline profile and multiplying this with the Sky View Factor. The skyline profile is a simple visual representation of the line along which the surface of the earth and/or obstructions and the sky meet. An example of this is displayed in Fig. 4.1. The Shading Factor (SF) is simply 0 when the sun is behind an obstruction and equal to 1 otherwise.
For the reflected irradiance similarly to the irradiance on the module also the irradiance on the reflected surface needs to be calculated with its own Sky View Factor and Sky View Factor. The irradiance the reflected surface received is calculated by multiplying the irradiance incident on the reflecting surface with the view factor of the receiving surface to the reflecting surface (VF_{Ground}) and the albedo value. The albedo is a measure of the diffuse reflection of solar radiation out of the total solar radiation received by a reflected surface. It is dimensionless and can be measured using an albedometer on a scale from 0 (corresponding to a black body that does not reflect any incident radiation) to 1 (corresponding to a body that reflects all incident radiation). As was described in an earlier Chapter, for the Sandia 3D VF model this is implemented by setting up a grid for the ground below the module and calculating for each grid cell the incident irradiance in order to calculate the reflected irradiance by multiplying with an albedo and ground view factors. For a free horizon, this can still be considered fast, but within an urban environment, calculation time can quickly become very long since the irradiance calculations must be performed for all the grid cells on the obstruction which are typically large surfaces.
While the obstructions are implemented within the mathematical equations described in Chapter 2 for the view factor model. For the ray-tracing models, the obstructions are simply implemented during the CAD design of the scene. Each surface is drawn in to the scene and given its optical properties, like reflectance and transmittance. While the ray-tracing simulation is carried out in a similar manner as was previously discussed in the earlier chapter. However, it should be noted that each additional surface reflecting light onto a surface can have a negative impact on the simulation time since the traced rays can follow a longer path to the light source or receiving surface after more bounces of other surfaces.

While previously it can be concluded that the LightTools, Radiance and 3D VF models show similar trends and yearly irradiance predictions, the simulation time between the three models varies greatly.

4.2. New Rhino/Grasshopper VF based model implementation

In this paragraph, the new irradiance model that has been designed is explained in detail. The model is created with Rhinoceros, a 3D modeling software including the plug-in Grasshopper for performing the mathematical irradiance calculations.

4.2.1. Reconstructing skyline

From the previous paragraph, it was shown that in order to calculate the irradiance on a surface with different obstructions nearby like a typical urban environment, the skyline profile needs to be determined. With this skyline profile, the Sky View Factor (SVF) can be calculated, using Eq. 2.8. Also, the View Factor (VF_{ground}) of the receiving solar cell from a reflecting surface can be calculated, using the same equation. Besides the relevant view factors, the skyline profile can also be used to determine the Shading Factor (SF) of a receiving surface. Simply by investigating on the skyline profile whether at the sun's azimuth and altitude values the closest cast ray did not intercept a sky blocking object. How the view factors and shading factors are modeled will be explained in more detailed in the following paragraph. This paragraph explains how the skyline profile is modeled.
In this study the skyline profile is constructed based on the simple, yet accurate view factor estimation method called ray-casting [52]. In this method, the view factor is determined by sending out a number of rays, evenly distributed in all directions of the hemisphere from an irradiance receiving surface. A cast ray that is sent in a certain azimuth and altitude direction, is given a binary value of 1 or 0. With 0 indicating a hit of an obstruction. Obstructions block the diffuse/direct irradiance coming from the sky-dome behind the obstruction.
The rays are cast into the sky-dome based on a certain angular resolution for azimuth and altitude. With a

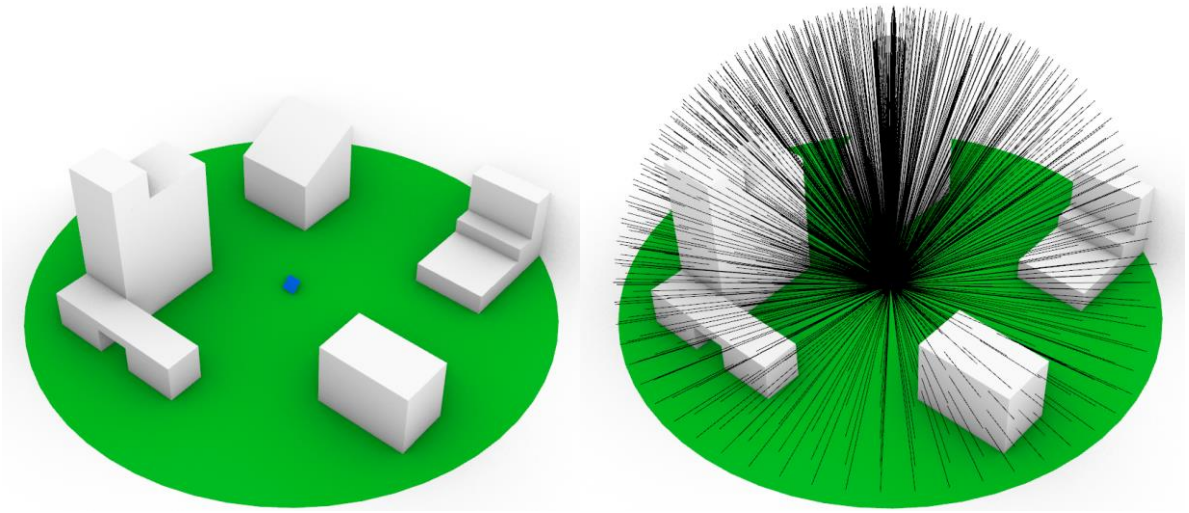

Figure 4.2: Examples of single module tilted 4^o on the left and the rays that are cast from the center of the module into the sky dome on the right.

lower angular resolution directly resulting in a higher number of rays send. This however results in a clearer and more accurate skyline profile, and subsequently in a more accurate prediction of the view factors and shading factors. However, the simulation time will also increase, due to the higher number of calculations that need to be performed for the higher amount of rays. For this reason only rays in front of the Point Of Array (POA) are cast since it is known that rays behind the POA do not contribute to the irradiance calculations. In the Fig. 4.3 below two examples of the ray casting method for different PV modules is displayed. On the left, a single module tilted 45 degrees and on the right the same module placed within an urban environment.

In Fig. 4.4 the resulting skyline profile of the two examples is displayed. Blocked or sky patches behind the POA are displayed in gray while the visible sky is displayed in blue. Since the module is tilted 45 degrees part of the sky falls behind the POA. In the skyline profile this is displayed by the dark gray silhouette around

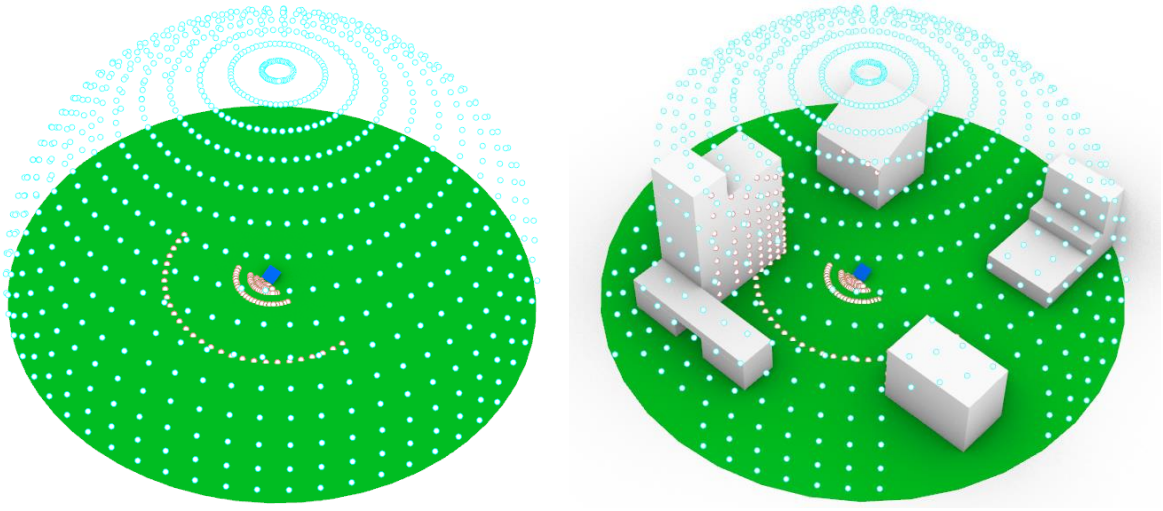

Figure 4.3: Examples used to explain model working. Left single module tilted 45^o. Right: Tilted module in urban environment. Blue dots indicate ray that has been cast without an interception with obstruction nearby. Brown dot indicate the intercepted point of the cast ray and the obstruction or ground.

the Northside of the skyline profile since the module is tilted 45 degrees to the south. For the module placed within the urban environment, the skyline profile also shows the silhouette of the two buildings blocking the sky in front of the tilted module. These obstructions blocking part of the skydome will lead to less diffuse irradiance and if the sun is behind the obstruction also no direct irradiance falling onto the solar module.

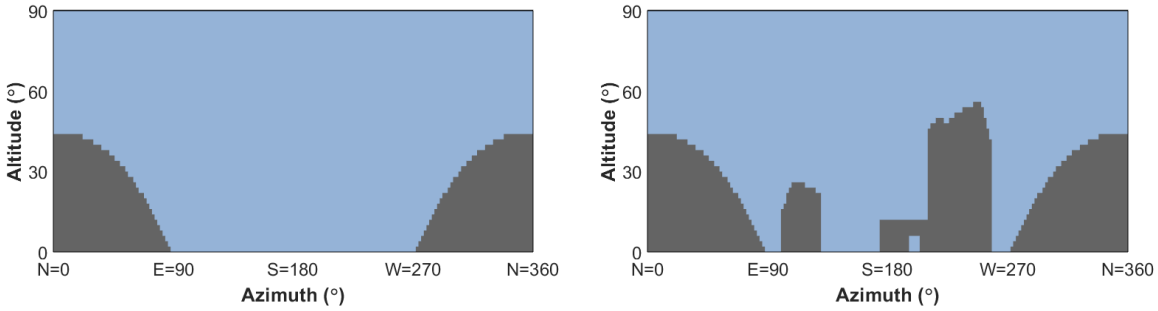

Figure 4.4: Skyline profile of single module tilted 45^o (Left), and same module placed within urban environment (Right).

4.2.2. Calculating direct and diffuse irradiance with sky view factor and solar cell shading factor

After constructing the skyline profile the next step in calculating the irradiance incident on the solar cell/module is calculating the solar module's Sky View Factor and Shading Factor. This is done by calculating the view factor of each sky section with Eq. 2.8, based on each cast ray's altitude and azimuth. And multiplying the skyline profile with the Sky View Factors, this ensures only unblocked Sky View Factors are considered. Since in the Rhino/Grasshopper model the altitude and azimuth of the blocked rays and rays falling behind the POA are filtered out no multiplication is needed, only the calculation based on the equation mentioned earlier. These Sky View Factors can then be used to calculate the Diffuse irradiance originating from the visible skydome. This is done by multiplying the irradiance originating from each sky patch with the Sky View Factor of the solar module. As was mentioned in Chapter 2 the diffuse irradiance can be modeled based on different models, varying in complexity. The simplest model the Isotropic model assumes the sky as a uniform source of diffuse irradiance. The Rhino/Grasshopper model is based on the Isotropic model for sky diffuse irradiance when a free horizon is considered this is described with Eq. 2.15. In the Fig. 4.5 below the Sky View Factors after multiplication with the skyline profile for the two examples are displayed. From the Figure, it can be seen that the view factor is highest for sky patches directly facing the solar module. Since the isotropic sky module assumes the sky as a uniform source of diffuse irradiance the view factors can be simply summed, resulting in a

total SVF, and multiplied with the Diffuse Horizontal Irradiance to calculate the total diffuse component. The more the sky is blocked by objects the lower the total SVF and the lower the total diffuse irradiance incident on the solar module.

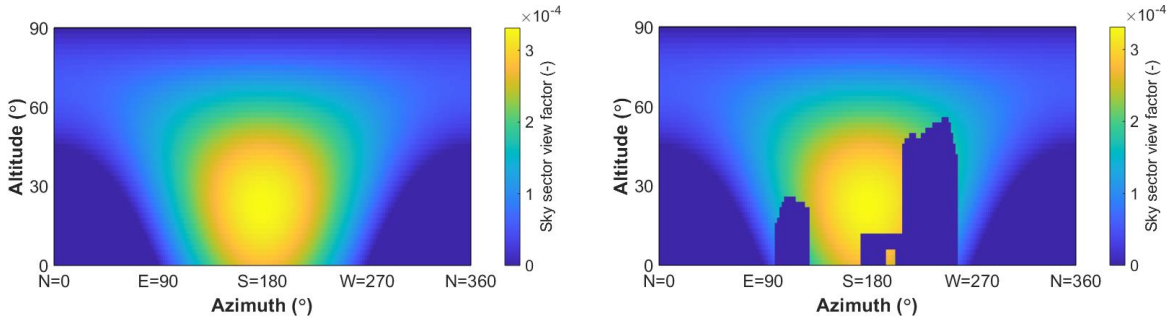

Figure 4.5: Sky sector view factor profile for single module tilted 45^o (left) and placed within urban environment (right).

In order to estimate the direct irradiance falling onto the solar module, it needs to be known whether the sun unblocked and facing the solar module. Or in other words, the Shading Factor needs to be determined. Since the position of the sun can be translated in an azimuth and altitude value, when investigating the same altitude and azimuth values for the skyline profile it can be determined whether the sun is (un)blocked and/or facing the solar module. The shading factor is then multiplied with the Direct Normal Irradiance to calculate the total direct component.

4.2.3. Calculating reflected irradiance with ground view factor, ground shading factor, albedo and ground incident irradiance

The reflected irradiance, as described in Eq. 2.20, is calculated using the albedo and the view factor of the ground cell to the solar cell. This is modeled by again tracing rays on to the environment. And calculating the view factor, albedo and irradiance values at the point of interception on the obstacle or ground. In the Fig. 4.6 below the intercepting points of the traced rays in the case of the two earlier examples are displayed.

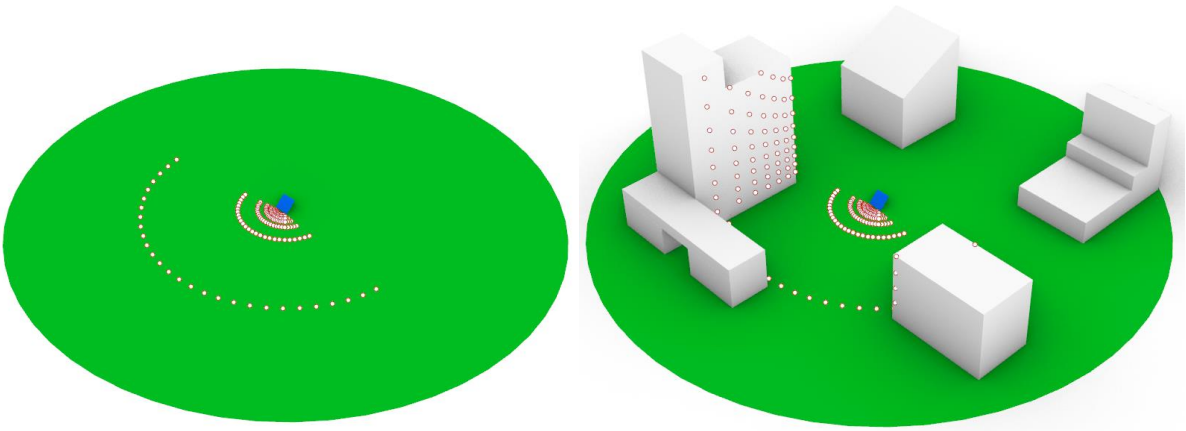

Figure 4.6: Intercepting points, displayed by brown dots, of traced rays. For examples of a single 45^o tilted module (left) and same module placed in urban environment (right).

As mentioned earlier for calculating the reflected irradiance incident on the solar module first the view factor quantifying the fraction of reflected irradiance from one surface arriving at the solar module needs to be determined. For simplicity, these view factors are called the surrounding View Factors ($VF_{i\rightarrow k}$). The $VF_{i\rightarrow k}$ are calculated similar to the SVF, with Eq. 2.8. Using the altitude and azimuth of each intercepting ray. In the Fig. 4.7 the $VF_{i\rightarrow k}$ of each intercepting ray is displayed. Notice that for the reflected light also rays in

the downward direction with a negative altitude are traced. Also for the $VF_{i\rightarrow k}$, it can be seen that the view factors are highest for reflecting surfaces directly facing the solar module.

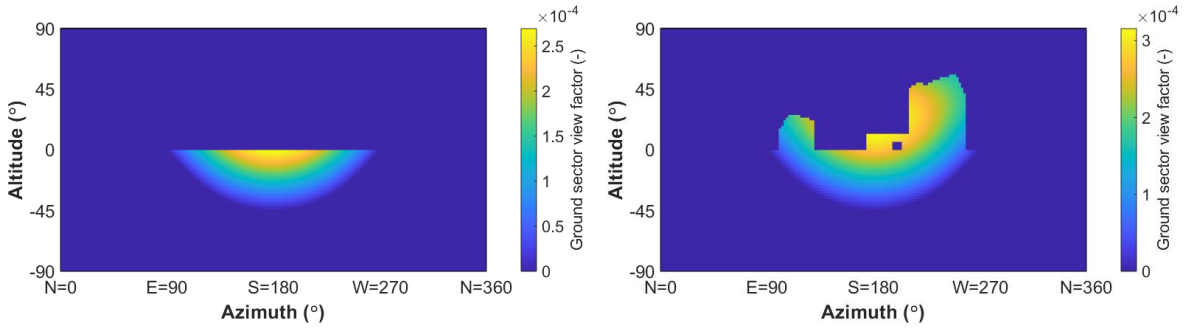

Figure 4.7: Ground sector view factor profile for single module tilted 45^o (left) and placed within urban environment (right).

That however does not mean that the surface with the highest view factor has the highest contribution of reflected irradiance since the reflected irradiance also depends on the amount of irradiance incident on the reflecting surface and the albedo of the reflecting surface. The albedo is a measure of how much light that hits the reflecting surface gets reflected without being absorbed. Each surface needs to be assigned an albedo quantifying how much of the incident irradiance it receives gets reflected onto the solar module. In Fig 4.8, an example of the albedo value of each reflecting surface is given. For the two examples, it was taken that the ground has an albedo of 0.25 and the surrounding white buildings an albedo of 0.5.

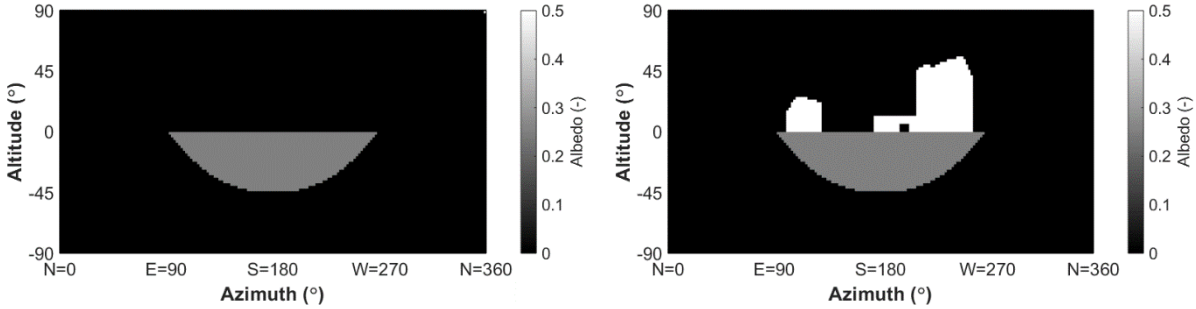

Figure 4.8: Albedo profile of the reflecting surfaces for the case of single module tilted 45^o (left) and placed within urban environment (right). With the ground surface having an albedo of 0.25 and the surrounding buildings an albedo of 0.5.

Before the reflecting irradiance can be calculated the irradiance incident on the reflecting surface needs to be determined. The irradiance incident on the reflecting surface is calculated similarly to the solar module. However only for the direct and diffuse component. Since if the reflected irradiance onto the reflected surface is also considered this quickly results in unnecessarily long simulations since theoretically the contribution of this extra component is very small. Considering it has to be multiplied with $VF_{ground\rightarrow cell}$, $Albedo_{ground}$, $VF_{surface\rightarrow ground}$ and $Albedo_{surface}$. This contribution of course becomes more significant when the reflecting surfaces have high albedo values. And the surrounding surfaces reflecting onto the solar module just like the solar module mostly receives reflected irradiance.

4.3. Basic validation and comparison with ray tracing models

In this section the New Rhino/Grasshopper VF based model implementation will be investigated. This will firstly be done by doing some basic validation checks in order to investigate whether the model actually measures what it should be measuring. Next, the model will be used for simulating different conditions. The simulation result will be compared with ray-tracing simulations under similar conditions. In order to identify the similarities and potential differences.

4.3.1. Basic validation checks

Check 1: with known VF

The first basic validation check is for investigating the view factor estimation performed by the model. In this

paragraph a simulation is performed and the view factor is estimated for a situation where the view factor can also be calculated mathematically, for comparison. According to Hamilton and Morgan [53] the view factor of a plane point source to an finite rectangle with dimensions a, b, c and angle θ, as seen in Fig. 4.9, can be calculated with the following equations:

$$V = \frac{1}{\sqrt{N^2 + L^2 - 2NLcos(\theta)}} \tag{4.1}$$

$$W = \sqrt{1 + L^2 sin^2(\theta)} \tag{4.2}$$

$$VF = \frac{1}{2\pi}\Big[tan^{-1}(\frac{1}{L}) + V(N \cdot cos(\theta) - L) \cdot tan^{-1}(V) + \frac{cos(\theta)}{W}\big[tan^{-1}(\frac{N - Lcos(\theta)}{W}) + tan^{-1}(\frac{Lcos(\theta)}{W})\big]\Big] \tag{4.3}$$

In the equation parameter N is the dimensionless ratio of the length and width of the finite rectangle ($\frac{a}{b}$). And parameter L is the dimensionless ratio described as the distance between source point to bottom corner of finite plane divided by the height of the finite plane ($\frac{c}{b}$). In the model the view factor is estimated by casting many rays in different directions, for each ray calculating the view factor of the intercepted ray and lastly summing up all the separate section view factors of only the intercepted rays. From the figure it can be seen that even under different angles of the finite rectangle the model still closely estimates the calculated view factor.

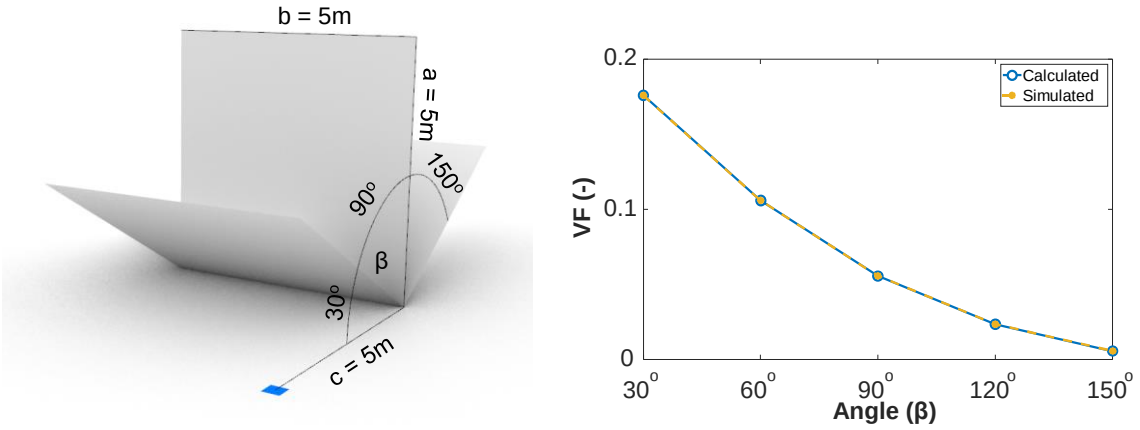

Figure 4.9: On the left the view factor from a plane point source (blue) to different angled finite rectangles (white). On the right a comparison of the view factor estimation based on the mathematical equation described in Eq. 4.3 and the same view factor estimation based on the ray casting method, performed with the Rhino/Grasshopper model.

Check 2: with known SF

Next, the shading factor calculation of the model is investigated. The Shading Factor simply resembles a binary value that represents whether the direct sunlight is (un)blocked, thus having a value 0 when the sun is behind an obstruction and equal to 1 otherwise. To investigate the working of the shading factor estimation of the model the same example urban environment as earlier is used. The sun is simulated hourly on the 9th of September, shown figuratively in Fig. 4.10. Between 9AM and 10AM the sun is blocked by the first building and between 4PM and 6PM by the second building. From 8PM the sun is behind the POA and should the shading factor also be considered blocked or 0. The model simulation results of the shading factor for the time period is displayed in Fig. 4.10. From the graph, it can be seen how the shading factor drops to 0 when the sun is behind the buildings or behind the POA of the module.

4.3.2. Comparison with forward and backward ray tracing

In this section, the total incident irradiance is simulated under different conditions. The simulation result is compared with other ray-tracing simulations methods. Namely, the backward ray-tracing method performed with the software Radiance and the forward ray-tracing method performed in the software LightTools. This

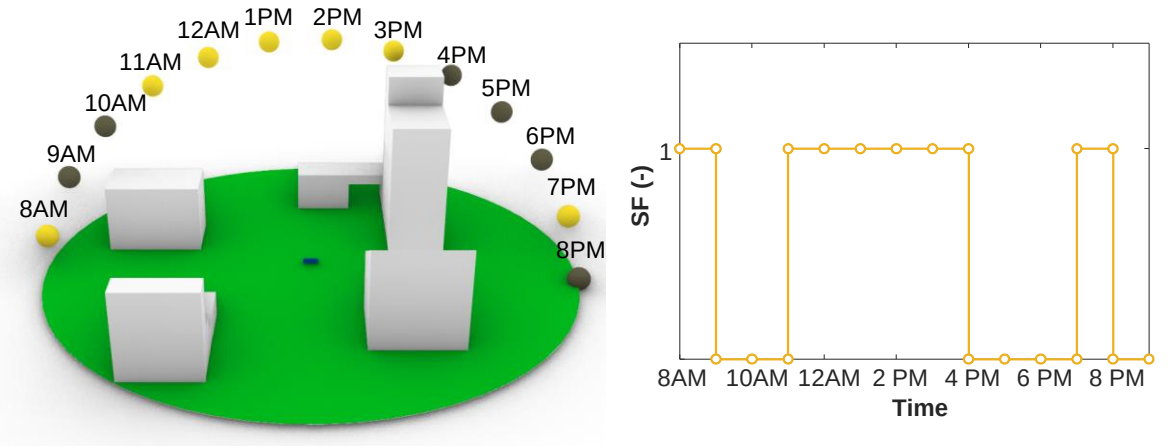

Figure 4.10: On the left a visualization of hourly sun spheres on the 9th of September for the solar module placed within an urban environment. The sun is painted yellow when it is in front and unblacked for the solar module. And painted black when it is either blocked by an building or behind the POA. On the right the simulation results for the shading factor (SF) of the solar module.

is done to investigate the working of the model but also identify potential differences in the results. For the comparison three conditions were set up.

- **Check 0:** Simulation of front side irradiance on a single 1 m^2 south facing solar module, under free horizon conditions. Also comparing the three models with similar calculations based on Eq. 2.9 to 2.15 described earlier.
- **Check 1:** Simulation of front- and back side irradiance on a 3 by 3 celled south facing solar module, again under free horizon conditions. At time instances when the sun is facing southeast and directly south.
- **Check 2:** And lastly considering the same 3 by 3 solar module, where part of the sky is blocked by an object. Considering the sun at a position where the solar module is unshaded and partially shaded.

Check 0: Single module tilted

For the first comparison the Rhino/Grasshopper 3D VF based model implementation is compared to different ray tracing models and also with the Eq. 2.9 to 2.15 described earlier. The ground reflected irradiance is based on the simplified formula [25]:

$$G_{Ground} = GHI \cdot \alpha \cdot (1 - \frac{1 + cos(\beta)}{2}) \tag{4.4}$$

As the simulations must be compared with each all the input parameters must be taken the same. The parameters that were taken for the simulations are: 1 m^2 square solar module, 0.5 m stand of height and a ground albedo of 0.25. For the sun, azimuth/altitude values of 115 and 25 degrees respectively where taken and DNI/DHI values of 600 and 70 respectively. With the ground drawn as a flat circle with a radius of 70 meters. The simulation results are displayed in Fig. 4.11 below. For the forward ray-tracing simulations in LightTools the sky map is constructed based on the complex luminance distribution of circumsolar and diffuse light across the sky but additionally also an isotropic sky.

From the graph, it can be seen that the 3D VF based model implementation perfectly follows the calculations based on the equations. This is also the case for the 0 degree tilted simulations performed with the ray-tracing models. However when the solar module is tilted deviations appear between the ray-tracing models and the rest. The reason deviations appear, is due to the way the sky is modeled between the different models. While the calculated and 3D VF models are based on the isotropic sky model, the ray-tracing models generally are based on more complex luminance distribution of circumsolar and diffuse light across the sky [33]. When the forward ray-tracing simulation is performed using the isotropic sky model the predictions are similar to the calculated values and the 3D VF model values. While the prediction based on the more complex luminance distribution is closer to the Radiance model. Not shown is the calculation based on the simplified Perez model (Equation 2.18). Also for this calculation, the same conclusion can be drawn as earlier. Simulation tools based on the Isotropic or Simplified Perez models can deviate from simulation tools based on complex luminance distribution of circumsolar and diffuse light across the sky when the surfaces are tilted.

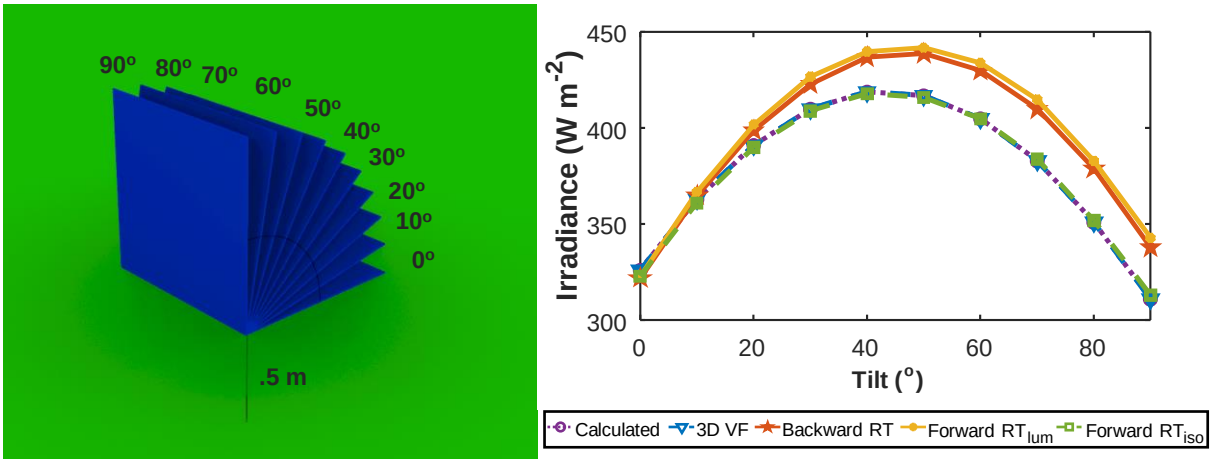

Figure 4.11: On the left a visualization of the 1 m^2 solar module that was simulated for different tilt angles. On the right the simulation results for calculations based on Eq. 2.9 to 2.15 incl. Eq. 4.4 for ground reflected irradiance (purple dotted line) in comparison with 3D view factor (blue dashed line), backwards (red line) and forward ray tracing models. The forward ray tracing model simulations are performed based on the luminance distribution sky model (yellow line) and the isotropic sky model (green dashed line).

When there is only reflected irradiance coming from the ground surface, almost no difference will be noticed between the models (when the same sky model is used). Within an urban environment where the light also reflects off tilted surfaces (like façades), these deviations can however become more significant.

Check 1: 9 solar cells with 0.1 m cell spacing

The irradiance models are also compared for the situation of 9 solar cells with a spacing between the cells of 0.1 meter. This is done because the irradiance models must also be used to measure the irradiance on the back-side of the solar module. And previously it was shown that under certain conditions by adding cell spacing the incident irradiance on the back can be increased. Fig. 4.12 shows the parameters that were used as input for the model. Also displayed is the dimensions of the sky blocking building which the calculations of the next paragraph is based on. The solar cells have a dimension of 0.158 by 0.158 meters. The module is placed with a stand off height of 0.5 meter, while the calculations are measured for a tilt angle of 0, 45 and 90 degrees respectively.

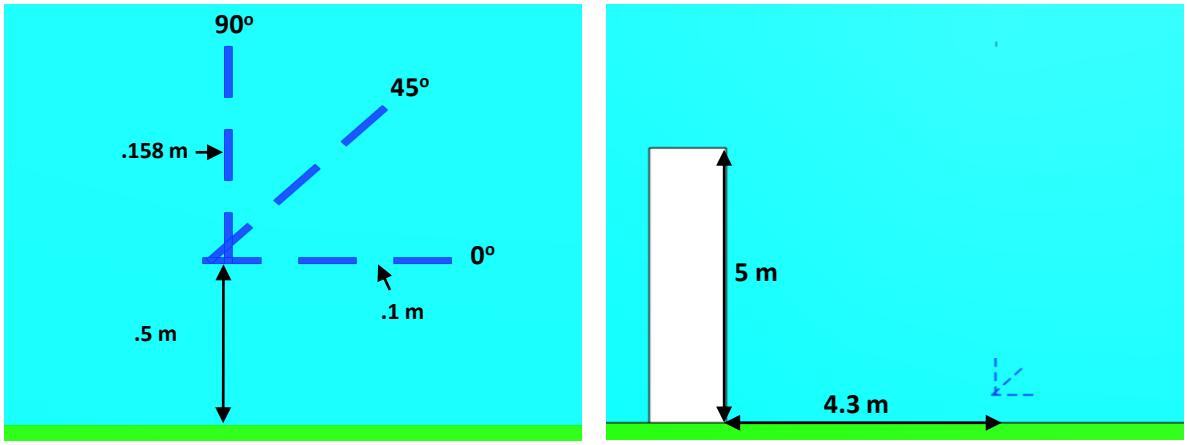

Figure 4.12: Sketch showing the different simulation input parameters that where considered. On the left the 9 celled solar module with 0.5 m stand off height, 0.158 · 0.158 m cell width and height and 0.1 cell spacing for different tilt angles considered during Check 1 and 2 is displayed. Also the dimensions of the sky blocking building of the Check 2 simulations is displayed on the right.

Rays are cast into the sky-dome based on a certain angular resolution for azimuth and altitude. The angular resolution is both important for calculating the solar module/cells SVF and SF but also for the reflecting surface. Higher angular resolution directly results in more accurate predictions. However, this also results in more rays and calculations that need to be performed. For this purpose it is important to find an optimal

angular resolution that results in accurate predictions. For the solar cell/module this is highly dependant on the environment the solar cell finds himself. The optimal solar cell/module angular resolution depends on the distance and area of obstructions. With wide obstructions that are closeby requiring a lower angular resolution that thin far away obstructions. The angular resolution for ground solar cells becomes particularly important when considering the irradiance on the back of a solar cell/module with cell spacing. When considering the 3 by 3 solar cell with 0.1 m cell spacing, for the reflecting surface below the solar module it is desired that the rays are cast with a low enough angular resolution that after a ray hits the solar cell the next ray is unobstructed and passes through the cell spacing. This is displayed figuratively in Fig. 4.13. The figure also displays the calculated angular resolutions plotted at different distances behind the solar module at varying tilt angles of 0, 45 and 90 degrees respectively. Also plotted is the distance of the shadow the lower

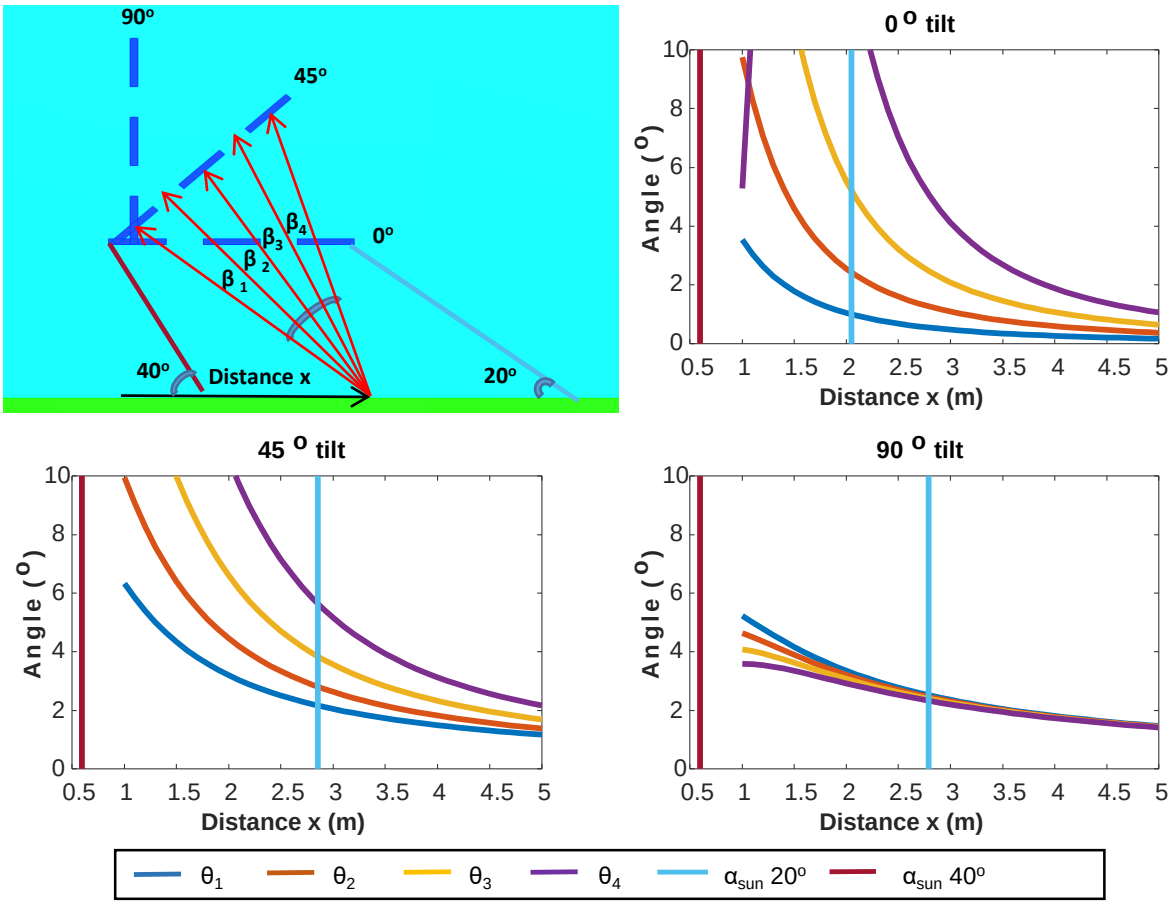

Figure 4.13: Illustration of 3 by 3 solar cell with 0.1 m cell spacing. Also displayed the calculated angular resolutions (θ_n) plotted at different distances behind the solar module at varying tilt angles of 0, 45 and 90 degree respectively. And the distance of the shadow the lower and upper corners of the solar module cast when the sun is at 40 and 20 degree.

and upper corners of the solar module cast when the sun is at 40 and 20 degrees respectively. Between these distances, it is desired to have a low enough angular resolution. From the figure it can be seen that the greater the distance between the measurement point of the reflecting surface and the solar module the smaller the angular resolution needs to be taken. Considering the furthest distance of the shadow due to the sun at a 20 degree altitude the maximum angular resolution that can be taken is 1, 2.2 and 2.3 degrees when the module is tilted 0, 45 and 90 degree respectively. These values are also considered for the next simulations in order to have fast and accurate simulation result with the 3D VF model.

For the first simulation, first the solar azimuth/altitude values of 115 and 25 degrees are taken and also DNI/DHI values of 600 and 70 W/m^2 respectively. In Fig. 4.14, the average, maximum and minimum incident irradiance for the front- and the back- side of the solar module for the different models is displayed. The irradiance values on each solar cell can be found in the Appendix. Also from the bar plots, it can be noticed how the 3D VF model starts underestimating the front side irradiance the more the module is tilted towards the sun. Deviations should also be noticed on the back the more the module gets tilted. However, the deviations

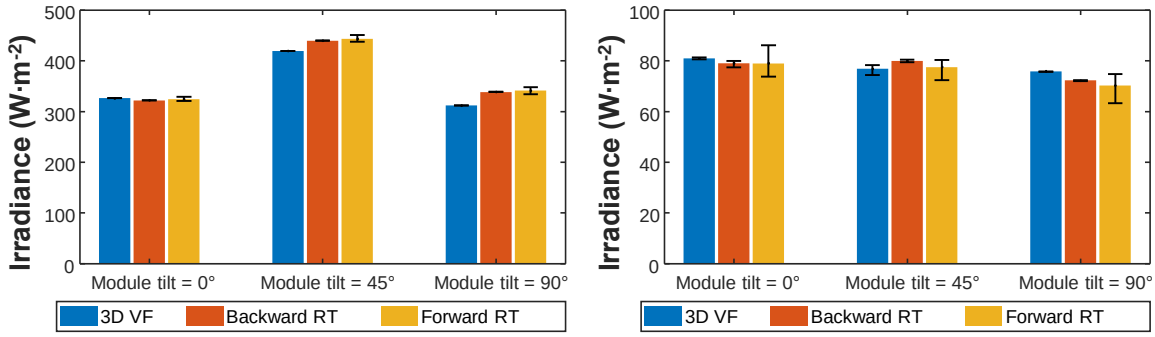

Figure 4.14: Bar plots showing the average, maximum and minimum incident irradiance on the front- (left) and the back side (right) of the solar module, for a tilt of 0, 45 and 90 degree. Simulations where performed with solar azimuth/altitude values of 115 and 25 degrees respectively and DNI/DHI values of 600 and 70 W/m^2 respectively.

are less significant for the south-facing module because the back mostly receives reflected irradiance originating from the horizontal ground below. Nevertheless, a higher tilt directly results in a higher contribution of direct and diffuse irradiance originating from across the sky. When only considering the front irradiance for the 0 degree tilted solar module the irradiance value incident on each cell should be exactly the same. This is the case for the 3D VF and the backward ray-tracing simulation. Considering the forward ray-tracing significant difference of 8 W/m^2 can be observed between the different solar cells. Even though for the simulations a very high accuracy setting was chosen, namely a ray density of around 13 thousand per square meter and a sky subdivision into 10240 sky patches.

Also for the sun directly facing south simulations are performed. Using azimuth/altitude values of 180 and 43 degrees and DNI/DHI values of 600 and 70 W/m^2 respectively. The resulting average, maximum and minimum incident irradiance for the front- and the back side of the solar module are displayed in Fig. 4.15 below.

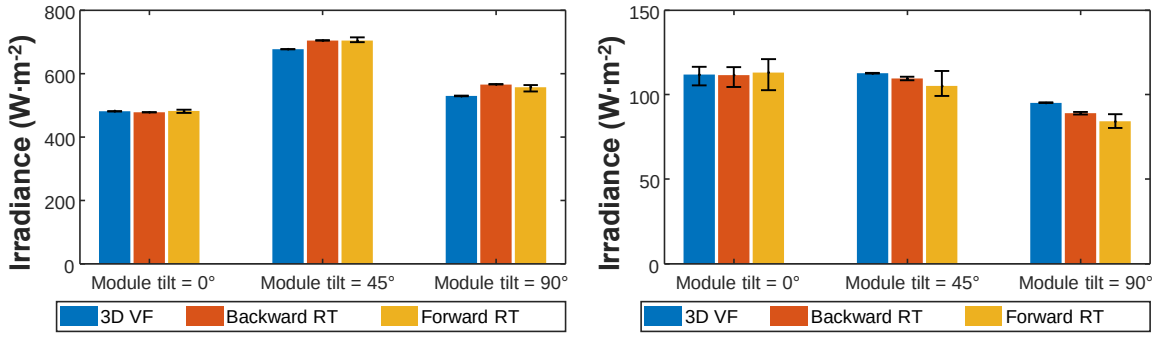

Figure 4.15: Bar plots showing the average, maximum and minimum incident irradiance on the front- (left) and the back side (right) of the solar module, for a tilt of 0, 45 and 90 degree. Simulations where performed with solar azimuth/altitude values of 180 and 43 degrees and DNI/DHI values of 600 and 70 W/m^2 respectively.

Since the sun is perfectly south and the solar module is also facing south, the back-side irradiance the outer edged solar cells receive should be exactly symmetrical. For each model, a difference can be noticed between the outer edged solar cells. The biggest difference between the symmetrical outer edged solar cells for the backward ray tracing is only 0.1 W/m^2. Considering the forward ray-tracing larger differences can be noticed. The biggest difference recorded is even 12.4 W/m^2 for the two lower outer edged solar cells considering the 45 degree tilted solar module. Also, the 3D VF model a difference of 1.1 W/m^2 is recorded between outer edged solar cells. This was however only recorded for the two lower outer edged solar cells when tilted 0 degrees, the rest only recording differences below 0.2 W/m^2.
From the bar plots above is can again be noticed, similar to Check 0 simulations, how considering the front side irradiance the 3D VF calculation is underestimated the more the solar module gets tilted. While the back side irradiance is overestimated in comparison to the ray tracing models.

Check 2: 9 solar cells facing sky blocking building

Comparison simulation is also performed for the situation where the 9 celled solar module is facing a building with dimensions as shown in Fig. 4.12. The first simulation for comparison was performed with solar azimuth/altitude values of 115 and 25 degrees and DNI/DHI values of 600 and 70 W/m^2 respectively. The resulting average, maximum and minimum incident irradiance for the front- and the back side of the solar module are displayed in Fig. 4.16 below.

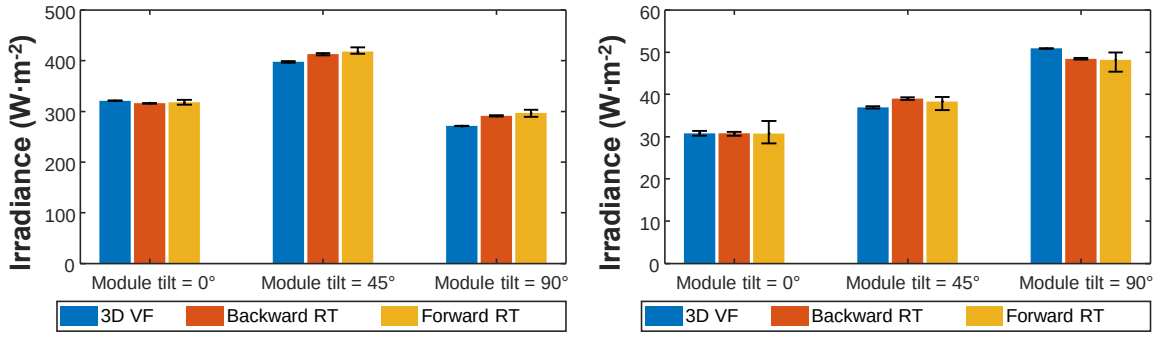

Figure 4.16: Bar plots showing the average, maximum and minimum incident irradiance on the front- (left) and the back side (right) of the solar module facing an building in front. Simulations are performed with solar azimuth/altitude values of 115 and 25 degrees and DNI/DHI values of 600 and 70 W/m^2 respectively.

Also shown is the irradiance distribution on each cell of the solar module for the 0 degree tilted module, in Fig. 4.17 below. The figure above shows even when considering the sky blocking building, besides some slight deviations in the back side measurements on the forward ray-tracing model, the three models show nice agreement in simulation results.

A noticeable difference was noticed when simulation was performed when the front side of the solar module was under partial shading due to shade cast by the building in front of the solar module. This is the case when the sun's azimuth/altitude values are 221 and 25 degrees and DNI/DHI values of 600 and 70 W/m^2 respectively are taken. In Fig. 4.18 below the resulting average, maximum and minimum incident irradiance on the front- and the back side of the solar module under these conditions are displayed. It is expected that the maximum and minimum of the solar module is much different compared to earlier simulation since some cells are fully shaded while others are unshaded. This causes the unshaded cells to record high irradiance values and other low irradiance values. In other words larger differences in the maximum and minimum values can will be noticed on the bar plots. Some cells can also be only half shaded. When the irradiance is solely measured from the middle of the solar cell this posses a problem, since then the irradiance over the entire solar module is either taken as fully shaded or unshaded.

This can be noticed in Fig. 4.19, showing the irradiance distribution on each cell at 0 degree tilt for partial shading conditions described earlier. The bottom left, middle and top right cells of the 3D VF solar module are all considered fully unshaded since only one measurement point at the center of each solar cell was considered. This is why the irradiance measurement on these cells is taken almost equal to the top left/middle and the middle left solar cells. The backward and forward ray-tracing simulation shows that the irradiance should be considered lower. Due to part of the solar cell to be shaded while the other part is unshaded. This effect causes the average irradiance across the entire solar cell to be lower compared to only the irradiance on the center of the solar cell. Backwards ray tracing considers irradiance on the entire solar cell and not only the center, by performing measurements at different points across the solar cell and not only the cell center. The forward ray-tracing inherently also measures irradiance across the entire solar cell, as long as the chosen ray density is high enough. This ensures that the rays send from the light source are spread evenly across the solar cell. When a building is causing partial shading part of the rays that are sent from the light source do not reach the solar cell while the unshaded part will still receives the rays.

Figure 4.17: Irradiance distribution on each cell of a 0 degree tilted 3 by 3 celled solar module blocked by a sky blocking building. Simulations are performed with solar azimuth/altitude values of 115 and 25 degrees and DNI/DHI values of 600 and 70 W/m^2 respectively.

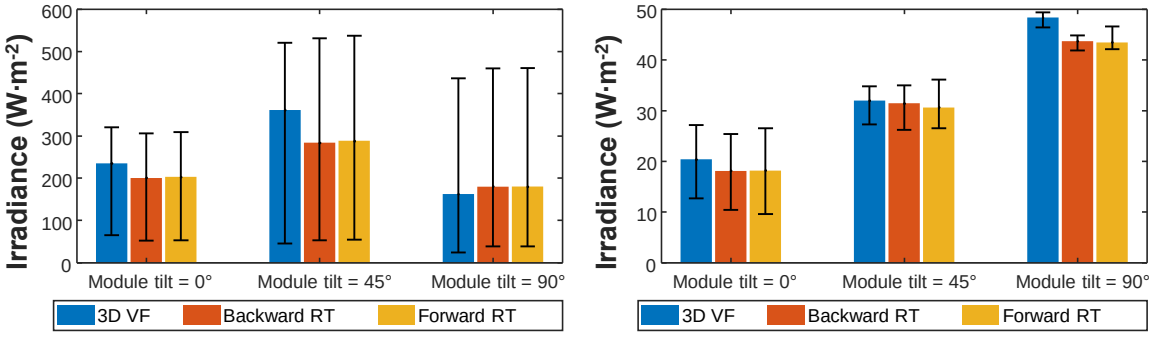

Figure 4.18: Bar plots showing the average, maximum and minimum incident irradiance on the front- (left) and the back side (right) of the solar module, for a tilt of 0, 45 and 90 degree. Simulations where performed with solar azimuth/altitude values of 221 and 25 degrees and DNI/DHI values of 600 and 70 W/m^2 respectively.

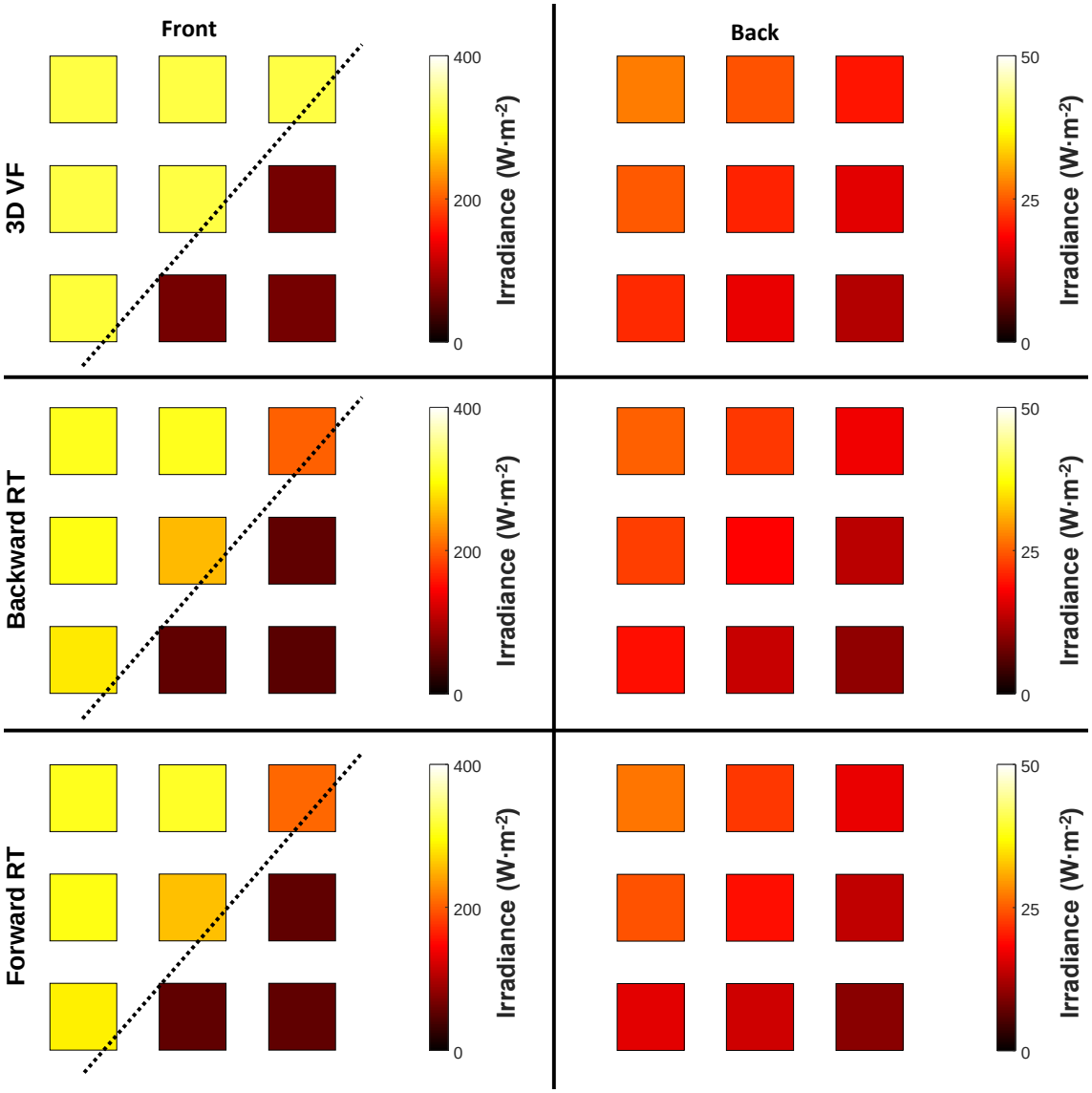

Figure 4.19: Irradiance distribution on each cell of a 0 degree tilted 3 by 3 celled solar module blocked by a sky blocking building. Simulations are performed with solar azimuth/altitude values of 221 and 25 degrees and DNI/DHI values of 600 and 70 W/m^2 respectively. Dashed line indicates the shadow falling on the PV module.

4.3.3. Discussion chapter

From the previous paragraph it can be concluded that the 3D VF model is well suited for modeling both the front and back irradiance on both a single 1 m^2 solar module or a 3 by 3 celled solar module with 0,1 m cell spacing when compared to other ray tracing models. It was also noticed that a higher tilt directly results in a difference noticed between the calculations based on Eq. 2.9 to 2.15, ground reflected irradiance Eq. 4.4 and the calculations performed based on the 3D VF models in comparison with the calculation based on the ray-tracing models. This is suspected to be because the later is based on more complex luminance distribution of circumsolar and diffuse light across the sky, while the earlier assumes an isotropic sky. Also, significant differences can be observed considering the 3D VF model calculations under partial shading conditions because the incident irradiance is measured with respect to the center of each cell instead of across the cell, like the ray-tracing models.

5

Model validation with monitoring station measurements

The aim of this chapter is to validate the irradiance model capable of simulating the front and rear side irradiance incident on a bifacial PV module as described in the previous chapter. This is done by comparing real outside measurements taken from the monitoring station with simulation results. For this purpose first in paragraph 5.1 the measurement setup at the monitoring station and the necessary parameters used as input for the irradiance models that have been extracted are discussed. In the following paragraph 5.2 the CAD design of the monitoring and the other reflecting surroundings created is described. Also within the paragraph, the CAD design is validated by comparing the skyline profile with real horizon profile obtained from the Horicatcher device [54]. The following paragraph 5.3 the 3D VF setup and initial ray casting results are displayed. The same is done for the ray-tracing models in paragraph 5.4. In the next paragraph 5.5 the validation result for 3D VF and ray tracing models irradiance simulations is given in comparison with real outdoor measurement taken from the PVMD monitoring station.

5.1. PVMD Monitoring station setup

At the PVMD groups monitoring station different measurements are taken using different measurement equipment. In this section, a detailed explanation of the monitoring station setup is presented. The monitoring station setup can be categorized into four categories. Namely, the Solys 2 sun tracker, the Single axis tracker, the Dual axis tracker and lastly the weather station. At each of the categories irradiance is measured. The location of the irradiance measurement locations on both the monitoring station and CAD design is displayed in Fig. 5.1.

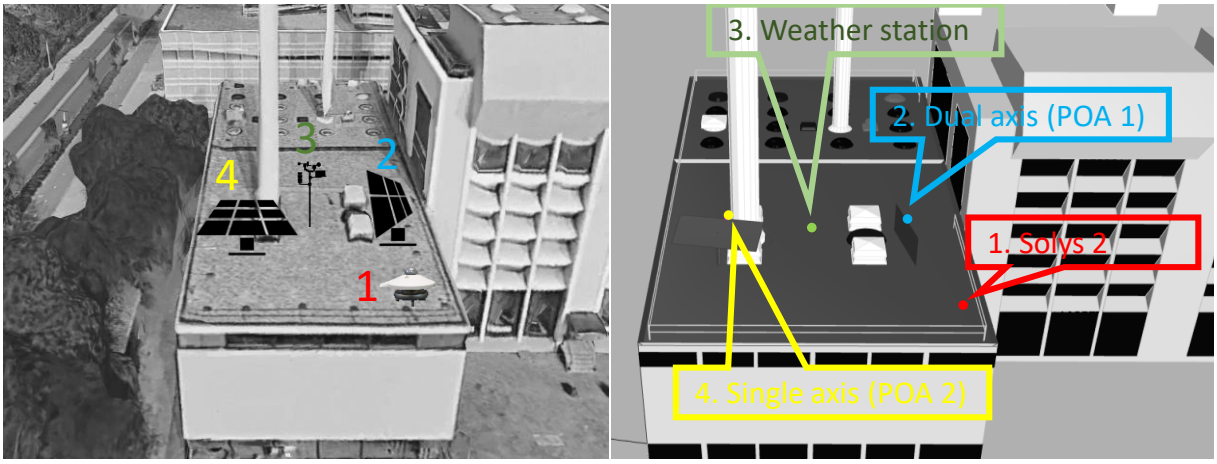

Figure 5.1: On the left an overview of the four irradiance measurement locations on the PVMD monitoring station roof. On the right the same measuring points in the CAD design.

The first location where irradiance measurements on the monitoring station are taken is at the Solys 2 sun tracker device, indicated by number 1 in Fig. 5.1. The Solys 2 sun tracker is a solar irradiance tracking system developed by Kipp & Zonen. It uses balls that follow the exact location of the sun and different pyrano- or pyrheliometer to measure the direct, diffuse and global irradiance components falling on the measuring device. It consists of two SPM 21 Kipp & Zonen pyranometers that measure the GHI and DHI and an SHP1 Kipp & Zonen Pyrheliometer for measuring the DNI. Also, an MS-700 EKO spectroradiometer is installed.

Next the irradiance is measured on the dual axis tracker, indicated by number 2 in Fig. 5.1. The dual axis tracker is a solar PV racking system with dimensions of 4.24m and 2.02m in length and width respectively. It has two degrees of freedom for rotation. Thus is able to rotate in both the x and y-axis. However, for simplicity during measurements the tilt and azimuth of the dual axis racking system were fixed at a 90 and 67 degree respectively. The dual axis racking system is able to hold multiple PV modules. During measurements a bifacial and monofacial PV module was installed on the racking system. Exactly in the top middle of the dual axis rack at a height of 3 meter an SMP 10 Kipp & Zonen pyranometer is installed for measuring the GPOA irradiance.

At the weather station multiple measurement instruments are installed to measure different weather conditions, such as wind speed/direction, ambient temperature, air humidity, dew point and pressure. The weather station is indicated with number 3 in Fig. 5.1. Also an ISET IKS Photovoltaic reference cell is installed for measuring the irradiance. The reference cell is installed at a height of 2.13m.

Lastly, the monitoring station consists of a single axis tracker, indicated by number 4 in Fig. 5.1. The single axis tracker is a solar PV racking system with dimensions of 4.24m and 2.02m in length and width respectively. It has a single degree of freedom for rotation. And is able adjust only the altitude of the rack while the azimuth is fixed to the south. During the measurements the tilt of the single axis racking system was fixed at a 30 degree respectively. Similar to the dual axis tracker the single axis tracker is able to hold multiple PV modules. During measurements two PV modules (one including PCM) were installed on the racking system. Around 1.89m from the top right of the single axis rack an SMP 10 Kipp & Zonen pyranometer is installed for measuring the GPOA irradiance.

5.2. CAD design and skyline profile comparison with real horizon

The irradiance that is measured at the PVMD monitoring station on TU Campus needs to be compared with simulation performed with the 3D VF, forward and backward ray-tracing simulations. The PVMD groups monitoring station is situated on the west-side roof of the WKC building, as can be seen on the left side of Fig. 5.2. The figure also displays the surroundings of the monitoring station. These surroundings also contribute to the irradiance the monitoring station receives. Either by blocking direct and diffuse irradiance of the sky-dome or by reflecting irradiance on to the receiving surface.

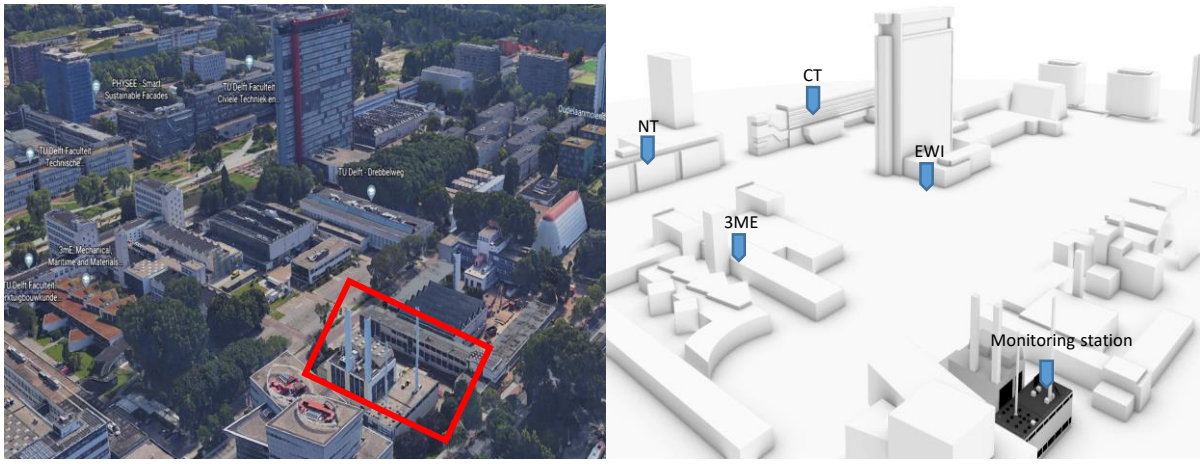

Figure 5.2: On the left the location of the PVMD monitoring station (Red square) and surrounding buildings on TU campus. On the right the CAD design of the monitoring building and surrounding buildings on the TU campus.

From first observations, some important irradiance blocking surroundings can be noticed. Namely, the higher part of the WKC building, the EWI building and some close-by trees. These surroundings are designed with varying detail depending on how important their contribution is to the irradiance measurements and

also difficulty to design. Some close-by trees for example can have a big influence on the irradiance received but are difficult to make a detailed CAD design of. Taking this into consideration it was decided that the monitoring station would be designed with the highest detail possible, the surrounding buildings on the TU Campus with less detail but still considering the 3-dimensional shape and orientation, while the trees are simply drawn as flat shapes based on the silhouette observed from the PVMD monitoring station. The resulting CAD design excluding the trees is depicted on the right of Fig. 5.2.
The CAD design must also be validated to prove the accuracy of the drawing with respect to reality. The validation of the CAD design is done with a Horicatcher device and the Meteonorm software [54]. The Horicatcher is a device that allows making pictures of a full hemisphere. The Horicatcher consists of a camera, a curved mirror and a tripod to hold all the parts together. The picture is taken from the zenith and uploaded into a software package provided by Meteonorm [54] which converts the picture to an equiangular representation. Meteonorm then allows for drawing of the horizon, converting the horizon to a file that holds all the information about the altitude of the horizon. Using a Matlab script the horizon can be drawn and compared to the skyline profile calculated at the same location in the CAD design. It should be noted that Meteonorm does not allow for overhanging geometries (multiple altitude values for a certain azimuth). Fig. 5.3, depicts

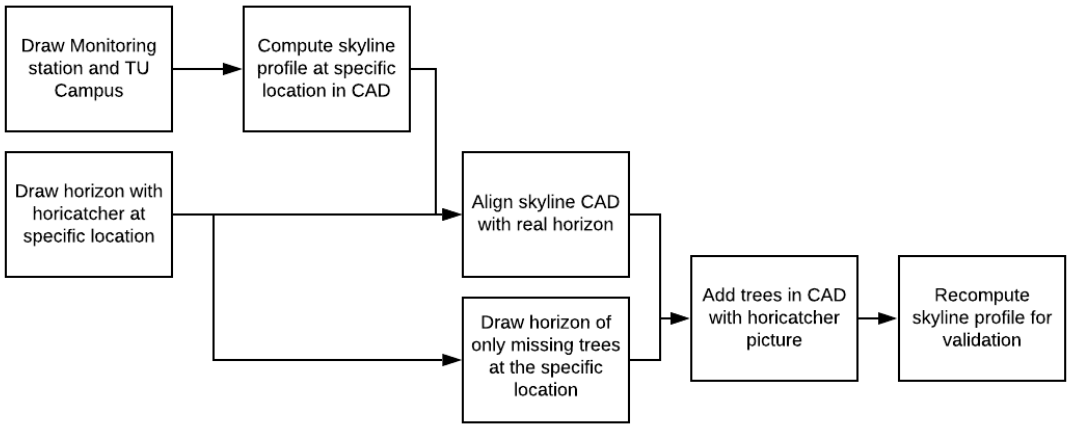

Figure 5.3: Block diagram describing the CAD Design and validation. First drawing the CAD for the monitoring station and the nearby buildings on the TU campus. Secondly computing the horizon and skyline profile with the Horicatcher and 3D VF model respectively. After alignment and adding the sky blocking trees, recomputing the horizon and skyline profile for comparison and validation.

a block diagram describing the steps taken for the CAD design and its validation. As the figure shows first the monitoring station and important nearby buildings on the TU campus are drawn with the Rhinoceros software. The monitoring station is drawn using a floor plan of the building and actual distance and angle measurements taken with the Bosch GLM 50C distance meter (See datasheet in the Appendix).
Next, at a specific location on the roof of the monitoring station the Horicatcher picture is taken and the resulting horizon is drawn within the Meteonorm software. For the same location in the CAD design the skyline profile based on the ray-tracing method described in the previous Chapter is constructed. The locations of the Horicatcher picture and the same location for the skyline profile calculation in the CAD design is depicted in Fig. 5.4. Three locations are chosen, at the front corners and at the center of the monitoring station. For locations 1 and 3 also pictures at a higher elevation are taken. Meaning in total five pictures is used for validating the CAD design. The skyline profile and the horizon profile is used to determine whether the orientation of the monitoring station or the surroundings on the TU Campus are properly aligned. The CAD design is rotated until the skyline profile falls perfectly under the horizon profile taken from the Meteonorm software.
The Horicatcher picture is also used for drawing the necessary trees into the CAD design. This is done as shown in Fig. 5.5. First, the trees are identified by visual inspection on the roof. Next, the silhouette of the trees is drawn in the Horicatcher picture with the best view of the trees. The location with the best view of the trees is location 1 as Fig. 5.5 shows. The altitude and azimuth values in the horizon profile is converted to cylindrical Cartesian coordinates and multiplied with the distance of the trees with respect to the Horicatcher picture. The trees are subsequently drawn into the CAD design by simply connecting the coordinates points. Trees with an altitude below 2 degrees are not considered or drawn since it is assumed they barely influence the irradiance on the roof.
Finally, the validation is concluded by constructing the skyline profile for the CAD design after adding the

trees and comparing this with the horizon profile of the Horicatcher picture.

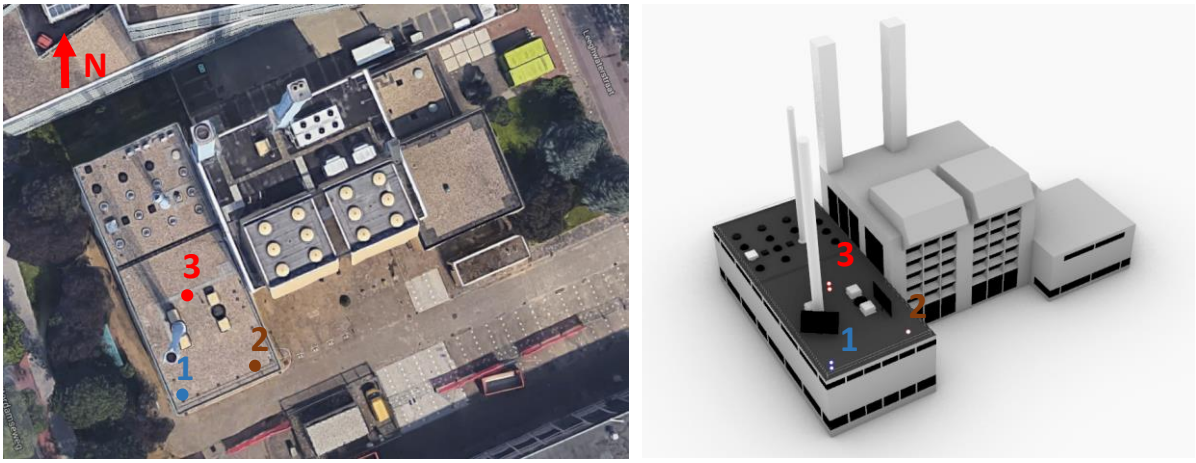

Figure 5.4: On the left the three locations where the Horicatcher pictures are taken for constructing the horizon in the Meteonorm software. On the right the same location on the monitoring station where the skyline profile was computed with the model.

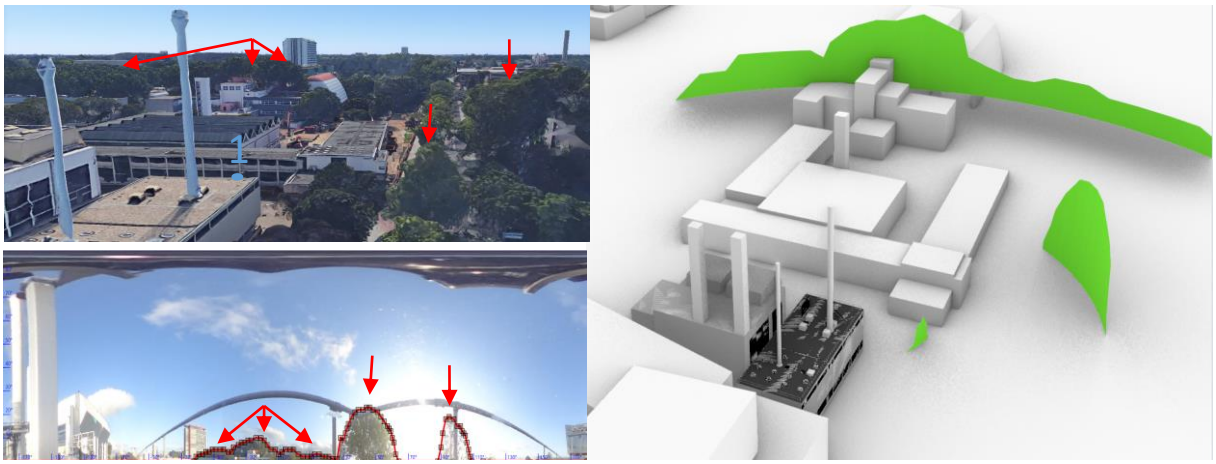

Figure 5.5: Figure displaying the process of drawing the necessary trees into the CAD design. First identifying the trees. Next drawing the tree silhouettes. And finally drawing the trees in the CAD.

In Fig. 5.6 below, the skyline and horizon profile at location 1 of the monitoring station is displayed. As the figure shows the main buildings blocking the sky-dome are the monitoring station in the northeast direction, the EWI building in the southeast direction and the InHolland graduate school building in the north direction.

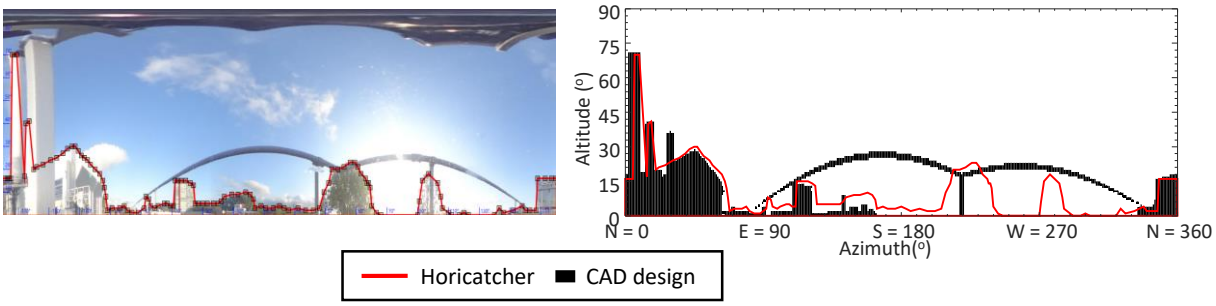

Figure 5.6: On the right the raised horizon image as taken from the Meteonorm software for lower orientation at location 1. On the right a comparison of the skyline profile after the CAD was aligned with the same horizon profile taken from the Meteonorm software.

As was mentioned earlier also some trees can be identified that block a large part of the sky-dome. Ignoring the trees can result in great under- or over-estimation of the irradiance estimations made on the monitoring station location. The same important conclusions can be made for location 2 and 3, displayed in Fig. 5.7 and 5.8 respectively.

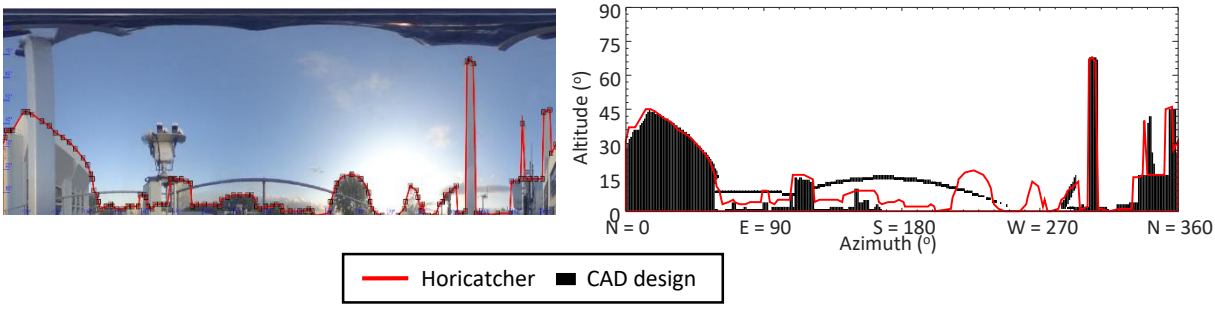

Figure 5.7: On the right the raised horizon image as taken from the Meteonorm software for lower orientation at location 2. On the right a comparison of the skyline profile after the CAD was aligned with the same horizon profile taken from the Meteonorm software.

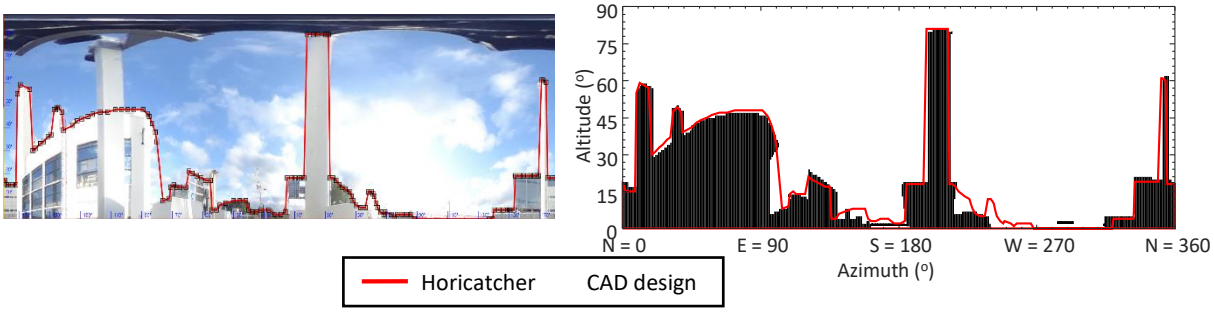

Figure 5.8: On the right the raised horizon image as taken from the Meteonorm software for lower orientation at location 3. On the right a comparison of the skyline profile after the CAD was aligned with the same horizon profile taken from the Meteonorm software.

The skyline profile is aligned for each of the locations and shows good agreement with the horizon profile for all the taken locations. The comparison of the different location however still highlights the importance of the sky blocking trees that should be included for properly estimating the irradiance. After adding the trees via the method described at the beginning of the paragraph this resulted in the skyline profile and horizon profile as depicted in Fig. 5.9 to 5.11.

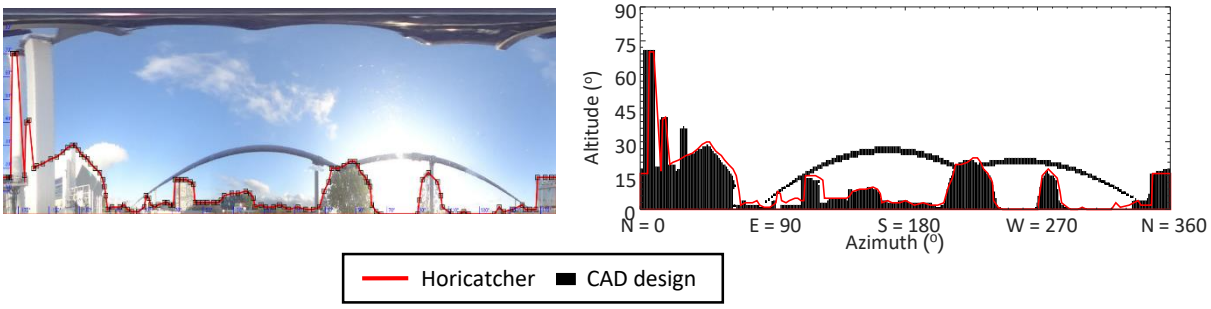

Figure 5.9: On the right the raised horizon image as taken from the Meteonorm software for lower orientation at location 1. On the right a comparison of the skyline profile after adding the trees with the same horizon profile taken from the Meteonorm software.

After drawing the monitoring station and adding the important surrounding objects such as the EWI/InHolland buildings and the trees the skyline profile shows good agreement with the horizon profile constructed from the Horicatcher picture. Only small deviations are noticed for some trees that are ignored due to them being

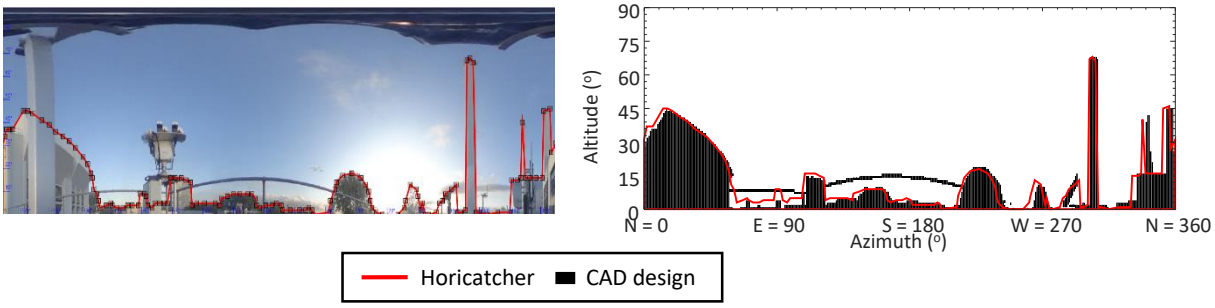

Figure 5.10: On the right the raised horizon image as taken from the Meteonorm software for lower orientation at location 2. On the right a comparison of the skyline profile after adding the trees with the same horizon profile taken from the Meteonorm software.

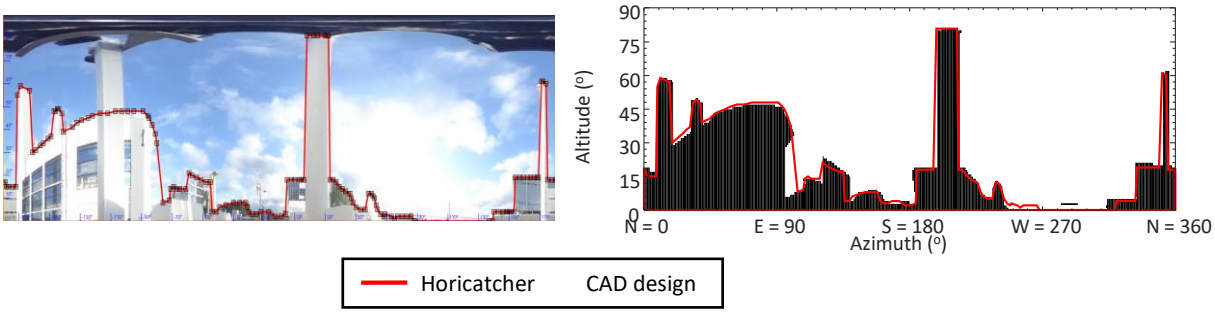

Figure 5.11: On the right the raised horizon image as taken from the Meteonorm software for lower orientation at location 3. On the right a comparison of the skyline profile after adding the trees with the same horizon profile taken from the Meteonorm software.

below the 2 degree boundary. Also, deviations can be noticed at locations where the Meteonorm software ignores overhanging geometries.

5.3. Ray casting initial setup and sky view factors and surface view factors results

The skyline profile and the SVF for POA 1 and POA 2 is calculated with the method described in sections 4.2.1 and 4.2.2. For the 3D VF simulations an angular resolution of 1^o was used for the ray casting performed at the pyranometer and a resolution of around 8^o for the ray casting performed at the reflecting surfaces. The resulting skyline profile and the equivalent SVF of each sky sector for POA 1 and 2 are displayed in Fig. 5.12 and 5.13 respectively. The SVF of POA 1 and 2 is calculated to be around .31 and .86 respectively. Since POA 1 is tilted 90 degrees this results in a lower SVF. Under free horizon conditions The skyline profile of a 90 degree tilted surface receives is 0.5, But due to the amoungst other the WKC building, the EWI building and some sky blocking trees a part of the skydome is blocked. These obstructions result in lower diffuse and for time periods when the sun is behind the objects also direct irradiance share. Instead, more irradiance gets reflected off these surfaces.

Each sky sector is determined by a ray that was cast with a certain altitude and azimuth direction into the scene. When this ray intercepts with a surface, it is translated into the intercepting surfaces tilt and azimuth angle. At each of the intercepting point, the skyline profile and SVF is calculated as explained in section 4.2.3. In total the entire scene consisted of around 2120 surfaces. For the select surfaces displayed in Fig. 5.14 the surrounding view factor ($VF_{i\rightarrow k}$) and SVF (SVF_i) is given in Table 5.1. Since multiple rays intercept with the surface the sum of the surrounding view factors and the SVF in the center of the surface is taken. In reality the SVF is calculated at each ray interception point.

From the table it can be seen that out of the reflecting surfaces the surface with the largest view factor are the corner surfaces of the WKC building and the tilted roof box surface, labeled by number 1, 4 and 5 in Fig. 5.14. The surfaces that have the largest SVF are surfaces with the lowest tilt angle. The more a surface is tilted the lower the SVF. Surfaces 1, 2 and 8 for example have a lower SVF because they are tilted 129 degrees, normal pointing towards the ground. The vertical surfaces like surfaces 3, 4, 5, 6 and 7 have a VF close to .5. When

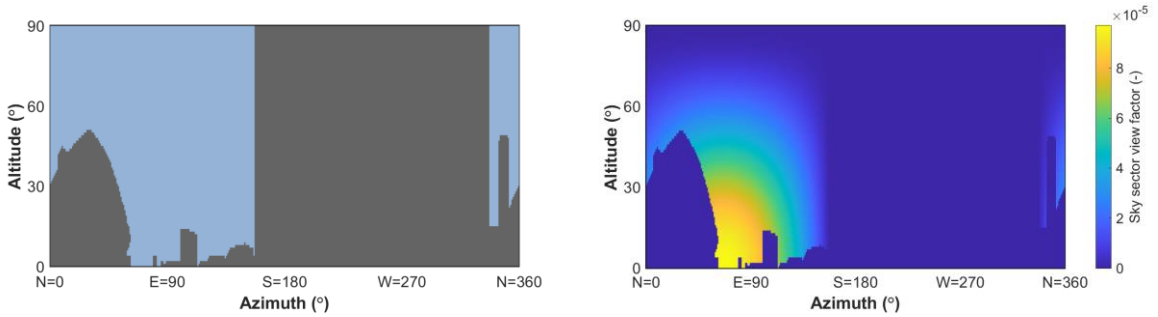

Figure 5.12: On the left the skyline profile for the single axis tracker (POA 1) measurement location calculated with 3D VF model. On the right the resulting sky sector view factor. The final SVF is calculated to be around 0.31.

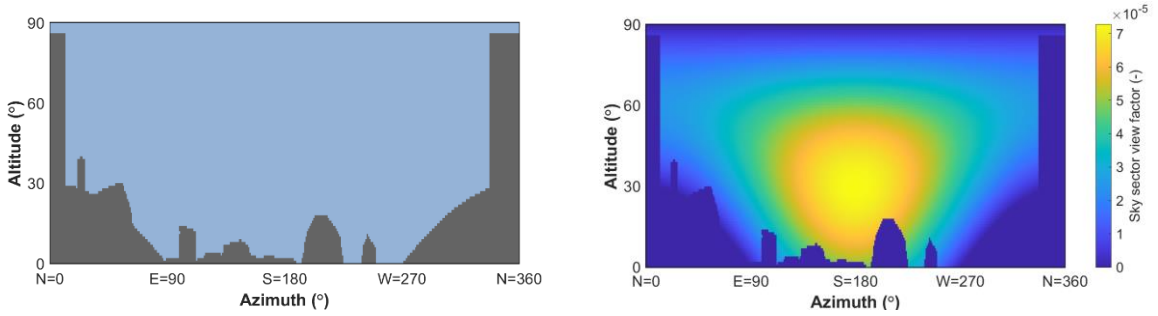

Figure 5.13: On the left the skyline profile for the the dual axis tracker (POA 2) measurement location calculated with 3D VF model. On the right the resulting sky sector view factor. The final SVF is calculated to be around 0.86.

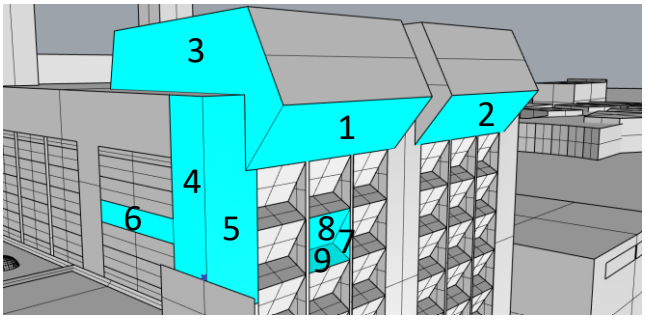

Figure 5.14: Illustration of the selected surfaces for which their surrounding view factor ($VF_{i\rightarrow k}$) and SVF (SVF_i) is calculated and given in Table 5.1.

Surface id	$\sum VF_{i\rightarrow k}$	$Tilt_i$	$Azimuth_i$	$SVF_{i,center}$	Description
1	0.0385	129	157	0.155	Lower part roof box
2	0.00456	129	157	.157	Lower part roof box
3	0.018616	90	247	.499	Side part roof box
4	0.03208	90	247	0.440	West part WKC
5	0.068503	90	157	0.416	South Part WKC
6	0.002846	90	247	0.434	Middle window south
7	0.001851	90	247	.145	Window edge
8	0.002208	120	157	.198	Window pointing down
9	0.001605	30	157	.452	Window pointing up

Table 5.1: Values of the surrounding view factor ($VF_{i\rightarrow k}$) and SVF (SVF_i) of the select surfaces displayed in Fig. 5.14. The SVF in the center of the surface is taken. The surrounding view factor is the sum of the surrounding view factors for each of the intercepting rays.

they have other sky blocking objects in front this leads to a lower SVF proportional with the how big a portion of the sky is blocked. Surface 7 for example has a large part of the sky blocked and thus has a lower SVF than

surfaces 3, 4, 5 and 6. While surface 9 has a low tilt the SVF is also lower due to it having a big portion of the sky that is blocked around the surface. The sky sector view factors for the different surfaces are displayed in Fig. 5.15. Data for all the surfaces can be found in Appendix C.

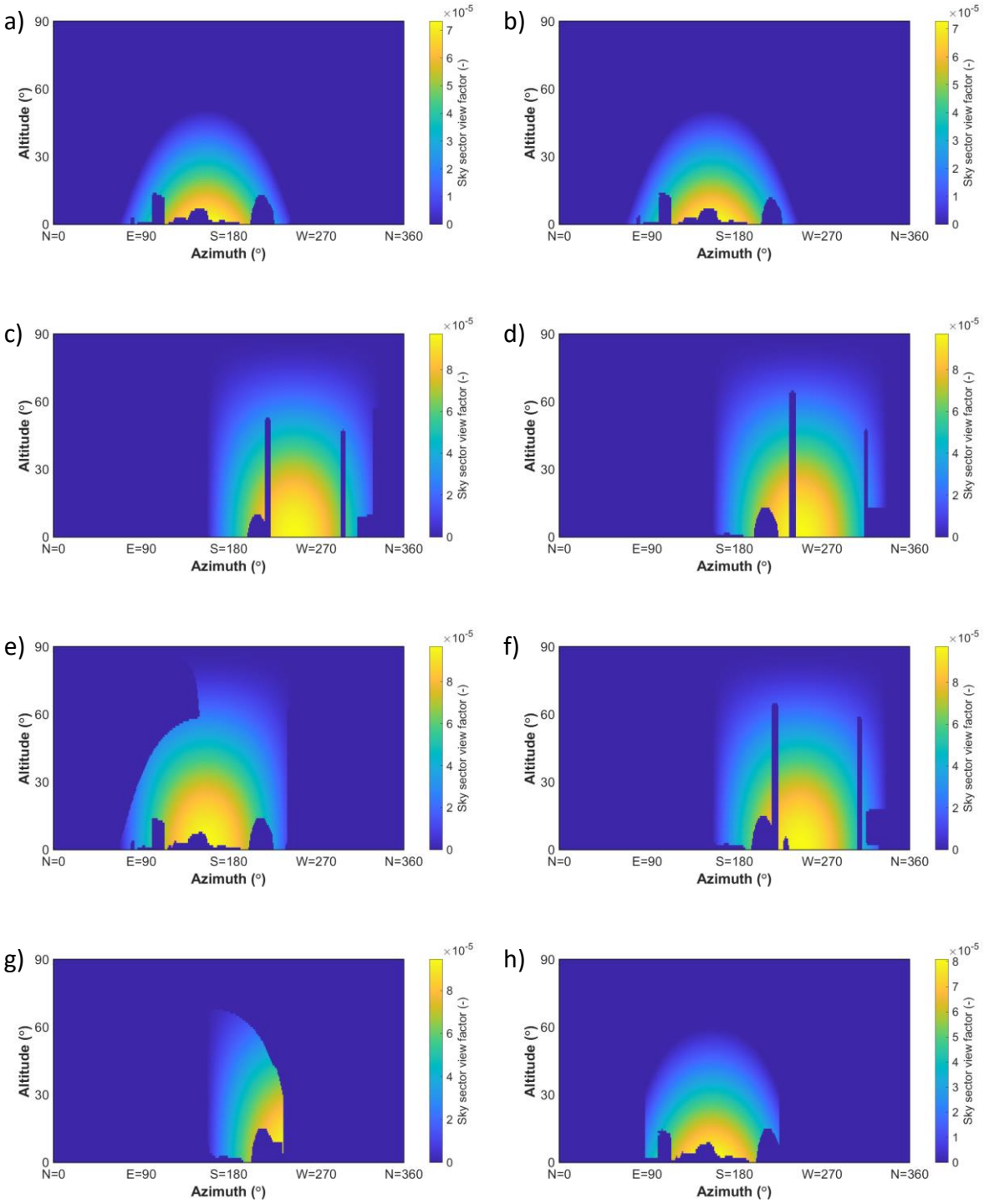

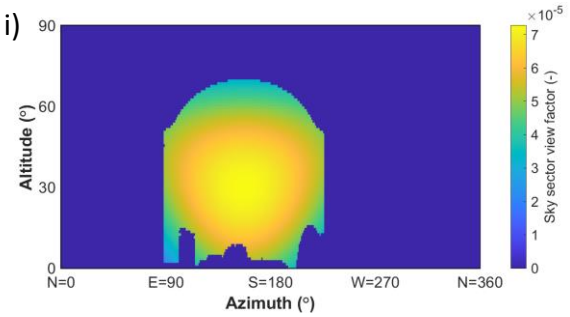

Figure 5.15: Sky sector view factors for the selected surrounding surfaces 1 through 9, labelled from a to i respectively.

5.4. Ray tracing simulation initial setup and results

The forward ray-tracing simulation was performed with the LightTools model as described earlier in Chapter 3. The pyranometer at POA 1 and 2 was modeled as a .158 by .158 meter square surface on top of the designated trackers. In order to obtain the sensitivity map for the forward ray-tracing simulation, a total number of rays of 10 million was chosen. The chosen number of rays ensures that when the sun is perpendicular with the pyranometer a ray density of 400 is received. An aim area with a radius of 14 meter was chosen. The aim area was aimed between the POA 1 and 2, but with a large enough radius to ensure the POA's are always inside the aim area during the simulation. This was also done so that a single ray-tracing simulation was needed to extract sensitivity maps for both POA's simultaneously. In Fig. 5.16 the simulation setup within the LightTools software is displayed. With both the POA 1 and 2 within the aim area the sensitivity map could be extracted. In Fig 5.17 the resulting sensitivity map obtained for POA 1 and 2 are displayed.

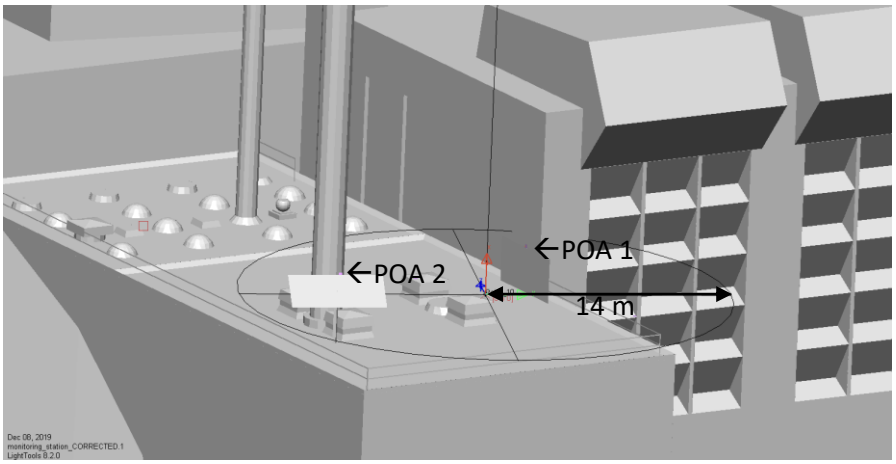

Figure 5.16: Simulation setup within LightTools.

The backward ray-tracing was performed using the Radiance software as described in Chapter 3. The Radiance simulations are performed using the accurate setting as given in Axel Jacob's Radiance tutorial [10]. These values can be found in Table 3.1. Radiance can only simulate the irradiance using 'gendaylit' or irradiation with the 'cumulative sky' approach. Earlier simulations used the 'cumulative sky' approach for simulations over an extended period. With this method the computational efficiency is improved since only a single simulation is performed. However, the temporal resolution which we are interested in for validation is lost, this is why the next backward ray-tracing simulations in Radiance is performed using 'gendaylit'. This however resulted in longer simulations since multiple ray-tracing simulations are needed for each irradiance measurement. The measurements consisted of measurements taken every minute from 5AM till 9:30PM, meaning in total 990 ray-tracing simulations were performed per POA per day.

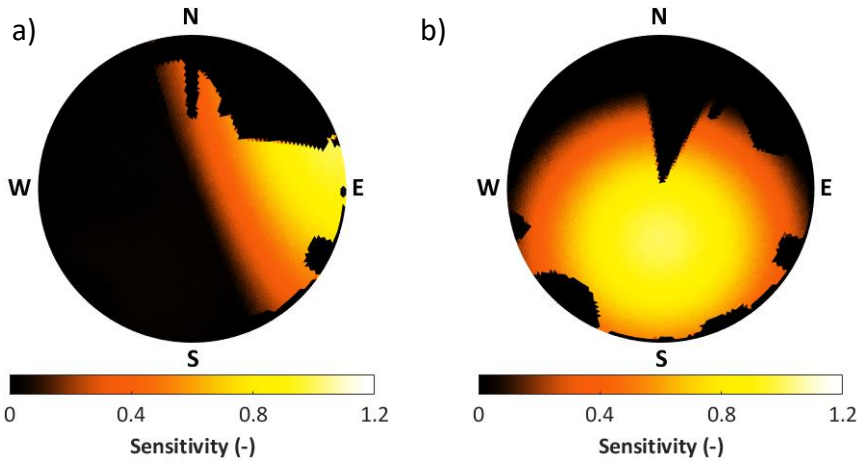

Figure 5.17: Sensitivity maps extracted for POA 1 and 2.

5.5. Irradiance simulation results and discussion

For validation of the simulation model results, measurement of DNI and DHI are taken from the Solys 2 and used as input for comparing the simulation models results. The irradiance measurements that are reproduced are the pyranometers installed on top of the dual- and single-axis tracker of the monitoring station. During measurement, both trackers had a fixed orientation. For this reason, henceforth they are referred too as POA 1 and POA 2 measurement for the dual- and fixed axis tracker respectively. Measurements on two different days are chosen. One clear sunny day and another overcast day. The sunny day is July 4th and the overcast day is July 10th both taken during the year 2019. For the simulation, an average albedo of 0.2 is taken. For all the simulation models all the reflecting surfaces are given this albedo value. It should be noted however that in reality each surface has a different albedo. And each corresponding albedo is not only determined by properties of the surface itself, but also by the spectral and angular distribution of irradiance reaching this surface [55].

In Fig. 5.18 and 5.19 the simulation and measured results for the overcast and sunny day measurements are depicted respectively. The top and middle graphs show the comparison of the simulation results obtained with the 3D VF, forward and backward ray tracing method at POA 1 and 2 respectively. Also displayed is the used DHI, DNI and GHI measurements that are retrieved from the Solys 2 measurement device in the bottom graph.
When considering the overcast day both the simulations at the POA 1 and 2 closely resembles the pyranometer measurement results. A slight underestimation of the 3D VF and forward ray-tracing method can be observed when considering the simulation results for the sunny day.

To analyse the different model predictions some statistical error metric values where calculated. The calculated error metrics are the root mean square error (RMSE), the mean bias error (MBE) and the mean absolute error (MAE).
The first metric, the RMSE, is a measure of how spread out the predictions are. In other words, by taking the average squared prediction error of each time instance an indication can be given of the difference between the model simulation results and the observed values is given.
The MBE is used as an indicator whether the model simulation results over- or underestimates the irradiation of the simulated day compared to the actual irradiation measurements.
Lastly, MAE is another commonly used measure of how spread out the predictions are. It is used to measures the average magnitude of prediction errors in a set of predictions, without considering if they are over- or underestimations. Both MAE and RMSE are negatively-oriented scores, which means lower values are better. The difference is the errors when calculating the RMSE are squared before they are averaged. Because they are squared the RMSE gives a relatively high weight to large errors. In other words the RMSE also penalizes variance as it gives errors with larger absolute values more weight than errors with smaller absolute values [56]. For this reason both metrics where calculated, as [56] suggest. Since by calculating both an indication is given into how spread the measures are and an indication if the spread is due to only a few large errors or

outliers. Additionally, by considering the difference between the MAE and MBE it can be concluded whether the over- or underestimation conclusion drawn by calculating the MBE is always true. Since, if the simulations where always under- or overestimated, the MAE and absolute value of MBE would be equal.

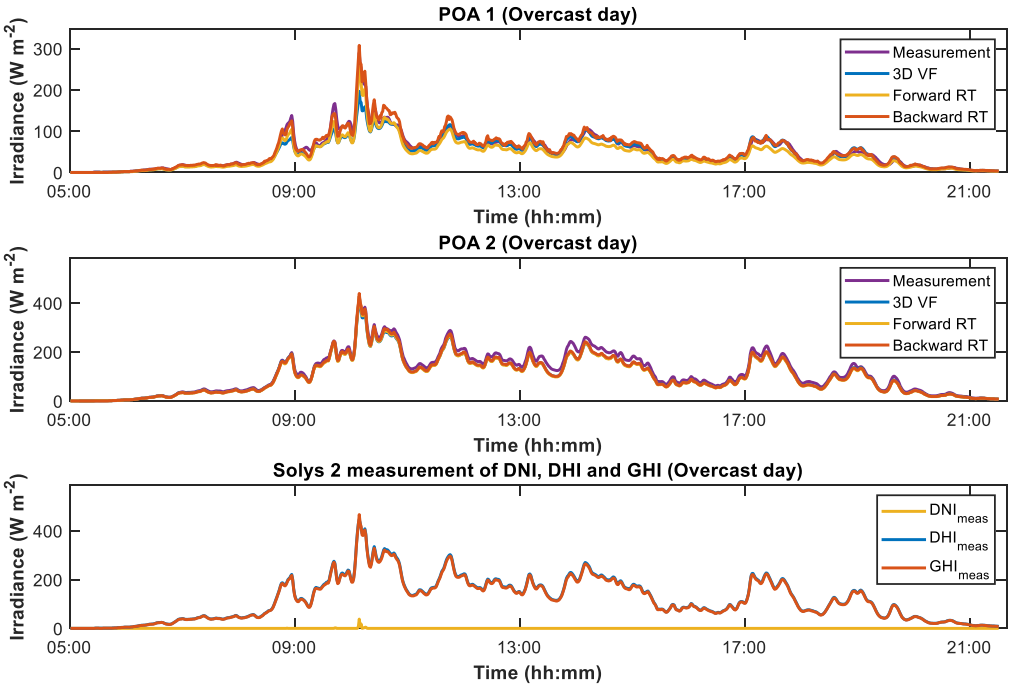

Figure 5.18: Upper and middle graph show the measured irradiance at POA 1 and 2 respectfully, for the overcast day of 10th of July. Also displayed is the simulation results for the 3D VF, forward and backward ray tracing models. In the lower graph the DNI, DHI and GHI Solys 2 measurement used to make the prediction is displayed.

The RMSE, MBE and MAE are defined as follows:

$$RMSE = \sqrt{\sum_{i=1}^{n} \frac{(G_{obs} - G_{Meas})^2}{n}} \tag{5.1}$$

$$MAE = \frac{\sum_{i=1}^{n} |G_{obs} - G_{Meas}|}{n} \tag{5.2}$$

$$MBE = \frac{\sum_{i=1}^{n} G_{obs} - G_{Meas}}{n} \tag{5.3}$$

In Table 5.2 and 5.3, the resulting metric values for POA 1 and 2 respectively is given. From the table 5.2 it can be seen how predictions on the overcast day are higher than predictions made on the sunny day for all models considered. During the overcast day the model can neglect the shading calculations (SF calculations for 3D VF model). Out of the three different models, the backwards ray tracing model best predicts the actual POA 1 measurements taken on both the overcast and sunny day, with an RMSE of around 8 Wh/m^2 and 29 Wh/m^2 on the overcast and sunny day. On the overcast day the 3D VF and forward ray tracing resulted in a similar RMSE of 12 Wh/m^2. On the sunny day the 3D VF has a lower RMSE of around 63 Wh/m^2 while the forward ray tracing model result in a higher RMSE of 66 Wh/m^2.
From the MBE metric values it can be seen that on both the sunny and overcast day the 3D VF and forward ray tracing model the irradiation is underestimated. The backwards ray tracing is the only model that overestimates the irradiation.
When considering the MAE which is a similar method to the RMSE for comparing the simulations with actual measurements the same conclusion can be drawn as for the RMSE. But additionally it can be seen that the simulations are not always under- or overestimated as was concluded with the MBE. This can be seen by the

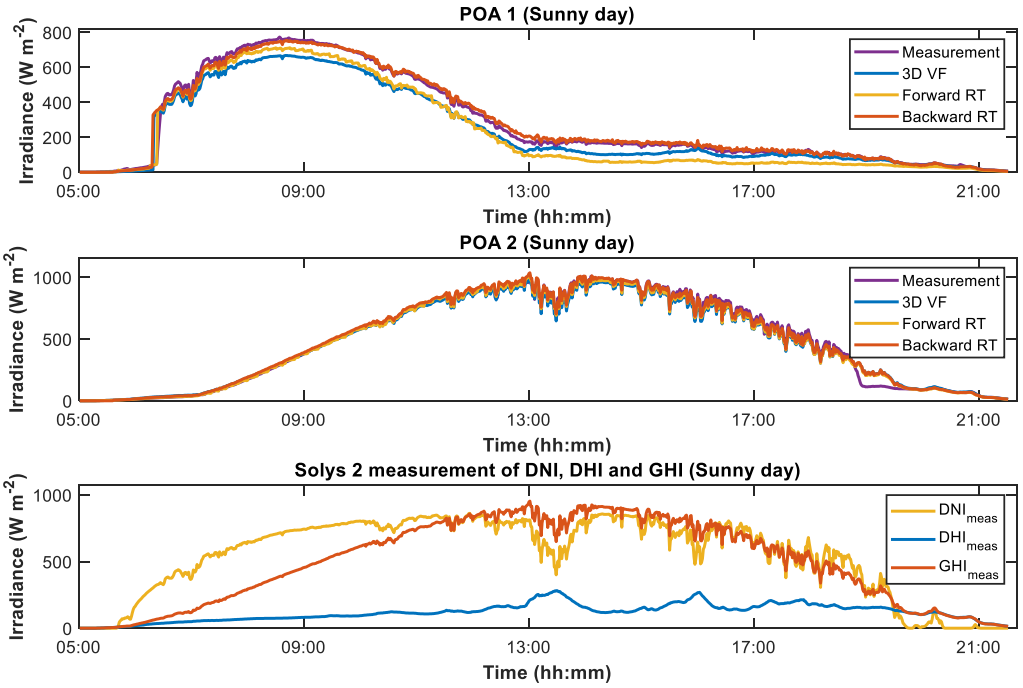

Figure 5.19: Upper and middle graph show the measured irradiance at POA 1 and 2 respectfully, for the clear sunny day of 4th of July. Also displayed is the simulation results for the 3D VF, forward and backward ray tracing models. In the lower graph the DNI, DHI and GHI Solys 2 measurement used to make the prediction is displayed.

	RMSE (Wh m^{-2})		MBE (Wh m^{-2})		MAE (Wh m^{-2})	
	Overcast day	Sunny day	Overcast day	Sunny day	Overcast day	Sunny day
3D VF	12.44	62.59	-4.15	-47.77	6.02	51.26
Forward RT	12.16	65.88	-9.20	-59.13	9.27	60.27
Backward RT	7.50	29.02	2.51	5.34	4.72	15.23

Table 5.2: RMSE, MBE and MAE values for POA 1 simulations compared with measurements retrieved on sunny and overcast summer days.

difference between the MAE and MBE. If the simulations where always under- or overestimated, the MAE and absolute value of MBE would be equal.

Table 5.3 the RMSE, MBE and MAE metric values for the POA 2 are given. Considering only the RMSE, out of the three different models the backwards ray tracing model again has the closest prediction to the actual POA 2 measurements taken on both the overcast and sunny day. While the 3D VF and forward ray tracing predictions again are also close for the overcast day. The forward ray tracing predictions are closer to actual measurements compared to 3D VF predictions on the sunny day.
The MBE value now shows that the all the models are underestimating the irradiation on the cloudy day. While on the sunny day only the forward ray tracing model overestimates the irradiation.
When considering the MAE which is a similar method to the RMSE for comparing the simulations with actual measurements. A similar conclusion is drawn as when the RMSE is considered. Again the 3D VF has a closer prediction of the actual measurements compared to the forward ray tracing model. Similarly, it can also be seen that the simulations are not always under- or overestimated as was concluded with the MBE. This can be seen by the difference between the MAE and the absolute value of MBE would be equal. If the simulations where always under- or overestimated, the MAE and MBE would be equal.

Notice how the metric values calculated earlier give the difference between the measured irradiation and the simulated irradiation throughout the measurement period. The relative RMSE, MBE and MAE in percent-

	RMSE (Wh m^{-2})		MBE (Wh m^{-2})		MAE (Wh m^{-2})	
	Overcast day	Sunny day	Overcast day	Sunny day	Overcast day	Sunny day
3D VF	14.60	31.62	-11.86	-21.22	11.87	25.69
Forward RT	15.72	21.97	-13.18	-13.38	13.19	16.36
Backward RT	13.28	16.08	-10.79	1.38	10.88	13.30

Table 5.3: RMSE, MBE and MAE values for POA 2 simulations compared with measurements retrieved on sunny and overcast summer days.

age of the measurements can be defined as followed:

$$RMSE = \sqrt{\sum_{i=1}^{n} \frac{(G_{obs} - G_{Meas})^2}{n \cdot \overline{G_{Meas}^2}}} \tag{5.4}$$

$$MAE = \frac{\sum_{i=1}^{n} |G_{obs} - G_{Meas}|}{n \cdot \overline{G_{Meas}}} \tag{5.5}$$

$$MBE = \frac{\sum_{i=1}^{n} G_{obs} - G_{Meas}}{n \cdot \overline{G_{Meas}}} \tag{5.6}$$

With $\overline{G_{Meas}}$ being the average irradiation measured with the Solys 2 device over the measuring time period. The $\overline{G_{Meas}}$ was calculated based on the following formula:

$$\overline{G_{Meas}} = \frac{\int G_{Meas} \cdot dt}{\int dt} \tag{5.7}$$

The $\overline{G_{Meas}}$, for the sunny day for POA 1 was around 54 and 308 Wh/m^2 on the overcast and sunny day respectively. While POA 2 received an average irradiation of around 125 and 601 Wh/m^2 on the overcast and sunny day respectively.

	RMSE (%)		MBE (%)		MAE (%)	
	Overcast day	Sunny day	Overcast day	Sunny day	Overcast day	Sunny day
3D VF	23.09	20.35	-7.71	-15.53	11.18	16.67
Forward RT	22.57	21.42	-17.08	-19.22	17.21	19.59
Backward RT	13.93	9.44	4.66	1.74	8.76	4.95

Table 5.4: The relative RMSE, MBE and MAE values for POA 1 simulations compared with measurements retrieved on sunny and overcast summer days.

	RMSE (%)		MBE (%)		MAE (%)	
	Overcast day	Sunny day	Overcast day	Sunny day	Overcast day	Sunny day
3D VF	11.7	5.26	-9.5	-3.53	9.51	4.27
Forward RT	12.59	3.65	-10.56	-2.23	10.57	2.72
Backward RT	10.64	2.67	-8.64	.23	8.72	2.21

Table 5.5: The relative RMSE, MBE and MAE values for POA 2 simulations compared with measurements retrieved on sunny and overcast summer days.

In Fig. 2.5, besides the total irradiance (G_{tot}^M) calculated with the 3D VF for the overcast and sunny day also the direct (G_{direct}), diffuse ($G_{diffuse}$) and reflected ($G_{reflected}$) irradiance component is given. For the overcast day the irradiance component with the highest share is the diffuse component. This is followed with the reflected irradiance. The direct irradiance is almost zero because the sky is overcast and their is little to no DNI measured during the day. The reflected irradiance is higher for the POA 1 measurement compared to POA 2. This is because the POA 1 measurement at the dual axis tracker has a 90^o tilt compared to POA 2's 30^o tilt. Also POA 1 is partly facing the WKC building which also reflects more irradiance on POA 1.

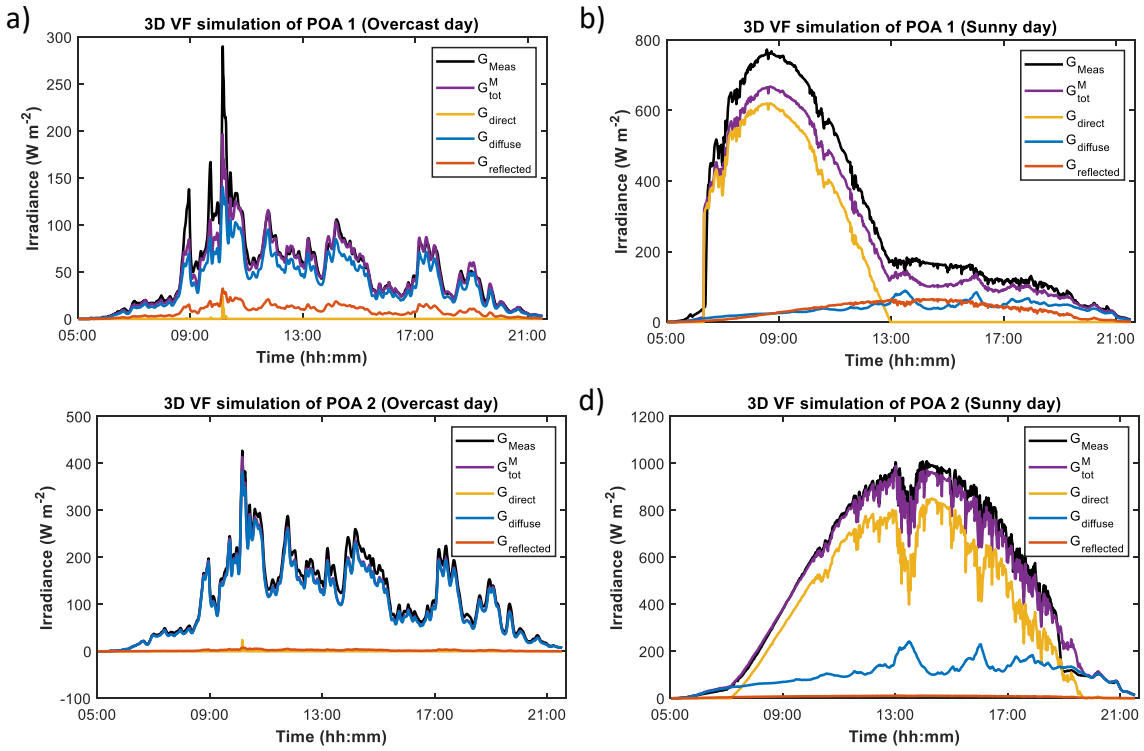

Figure 5.20: Total irradiance (G_M^{tot}) calculated with the 3D VF model, including the different irradiance components; direct (G_{Direct}), diffuse ($G_{Diffuse}$) and reflected ($G_{reflected}$).

Considering the sunny day, when the sun is in front of the POA the direct irradiance is mostly dominated by the direct irradiance. For the POA 1 simulation this is early in the morning when the sun rises in the east between 6 AM and when the sun is south around 1 PM. After this the sun is behind the AOI and the largest share is either the reflected and diffuse irradiance.
For POA 2 simulation the largest share is the direct irradiance since the sun is facing the POA throughout the measurement period. The second largest share is from the diffuse irradiance. While the reflected irradiance is neglegibly small.

5.5.1. Results after simple DHI correction

Earlier in the Chapter it was mentioned that the DHI, and DNI measurements are taken from the Solys 2. The Solys 2 is also placed on top of the PVMD monitoring station roof. The location of the Solys 2, displayed in Fig. 5.1, is at the southeast corner of the PVMD monitoring station. Measurements of the DHI are performed similar to the measurements for GHI except the DNI component of the irradiance is blocked by placing a ball at the exact solar position thought the measurement period. For the exact measurement of the DHI the measurements need to be taken with a free horizon or in other words where the sky is fully unblocked. At the PVMD monitoring station this is not the case. Due to this the actual DHI that is is as given by the following formula:

$$DHI_{meas} = SVF \cdot DHI_{real} + G_{Refl} \tag{5.8}$$

The actual DHI that is measured (DHI_{meas}) is multiplied with the SVF seen by the pyranometer, and an additional reflected irradiance G_{Refl} that is also measured. In the Fig. 5.21 the skyline profile and the each sky sectors view factor as seen from the Solys 2 measurement location in the CAD design is given. The sky view factor at this location is calculated to be around .92.

The reflected irradiance is expected to be negligibly low similar to the POA 2 measurements because the Solys 2 measurements are taken at an even lower tilt angle of 0^o. Neglecting the reflected irradiance after re-writing Eq. 5.8 the actual DHI can be calculated by multiplying the measured DHI with a correction factor of 1/SVF. This means that the measured DHI will increase after correction. It should be noted however that this does not necessarily have to be true, since the reflected irradiance should first be subtracted. The simulation results using the corrected DHI values is given in Table 5.6 and 5.7.

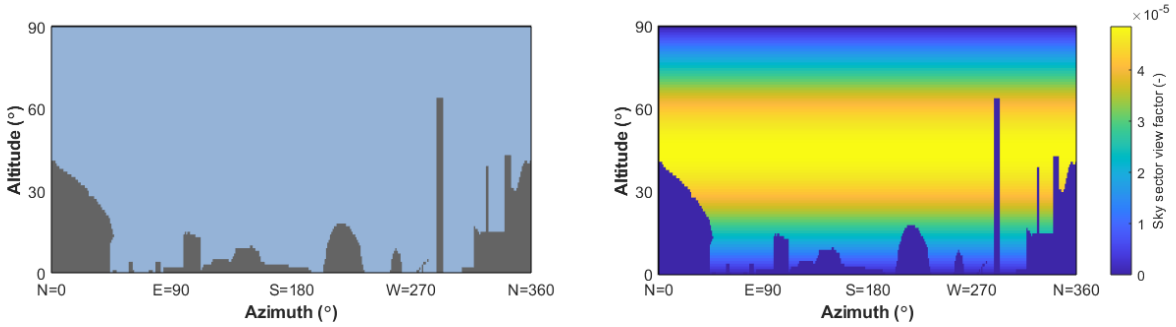

Figure 5.21: On the left the skyline profile for the Solys 2 measurement location calculated with 3D VF model. On the right the resulting sky sector view factor. The final SVF is calculated to be around 0.92.

	RMSE (%)		MBE (%)		MAE (%)	
	Overcast day	Sunny day	Overcast day	Sunny day	Overcast day	Sunny day
3D VF	19.96	19.38	0.60	-14.07	10.97	15.32
Forward RT	15.47	20.16	-8.76	-17.89	11.14	18.27
Backward RT	13.93	9.44	4.66	1.74	8.76	4.95

Table 5.6: RMSE, MBE and MAE values for POA 1 simulations compared with corrected DHI measurements measured on sunny and overcast summer days.

From table 5.6 it can be seen how the simple correction of the DHI measured at the Solys 2 affected the POA 1 simulation results. For each simulation method the DHI has an direct impact on the diffuse irradiance received. Also the reflected irradiance received is influenced. Since the reflecting surfaces also receive diffuse irradiance from the sky.
For both the 3D VF as well as the forward ray tracing models the simulation results are improved after using the corrected DHI measurement values. With a significant improvement on the overcast day and less significant on the sunny day. Noticeably, the MBE of the simulation is close to zero for the 3D VF model for the overcast simulation, while the MAE and RMSE are also lower. This indicates the 3D VF has smaller outliers. Also the outliers are evenly over- or underestimating the irradiance since the MBE is close to zero and MAE is above zero.
The conclusions drawn earlier for the forward ray tracing are still valid after correction of the simulation results, only in a lesser extent after the DHI correction.
Considering the backwards ray tracing model the simulation results for POA 1 are never improved with DHI corrections but rather worsened. Before the corrected DHI was implemented the POA 1 simulation results was slightly over estimated compared to measured results (See MBE results). Increasing the DHI only further over estimates the simulation results.

	RMSE (%)		MBE (%)		MAE (%)	
	Overcast day	Sunny day	Overcast day	Sunny day	Overcast day	Sunny day
3D VF	5.20	3.77	-1.35	-1.81	3.64	3.05
Forward RT	6.27	2.63	-2.25	-0.35	4.48	1.96
Backward RT	10.64	2.67	-8.64	0.23	8.71	2.21

Table 5.7: RMSE, MBE and MAE values for POA 2 simulations compared with corrected DHI measurements measured on sunny and overcast summer days.

In table 5.7 the simulation results, after correcting the DHI, at the POA 2 is given. The impact of the DHI correction is even more significant for the POA 2 simulations. This is because the POA 2 measurements due to its 30^o tilt and 180^o azimuth receives an higher share of diffuse irradiance. For this reason increasing the DHI after correction has a bigger impact on the POA 2 compared to POA 1. This can also be noticed in the simulation results.
An improvement is particularly noticeable during the overcast day. All the simulation models results are significantly improved compared to when uncorrected DHI is used. Considering the RMSE and MAE, the ray tracing models have the largest variance compared with the 3D VF model. However it is the backwards ray

tracing model that has the closest overall irradiation measurement when the MBE is considered.
On the sunny day only the 3D VF and forward ray tracing model simulation results are improved after the DHI correction is implemented. The ray tracing model simulation results are worsened, due to the already over estimation being further over estimated.

5.6. Discussion chapter

The aim of this chapter was to validate the irradiance model described in the earlier chapter with actual measurement. Also other simulation model predictions are considered for comparison. From the results obtained it can be concluded that the simulation model is capable of simulating the actual measurements. Even sometimes giving more accurate predictions compared to the other simulation models. While the models have a higher irradiation over- or underprediction the models performs better on the sunny day compared to overcast day. On the sunny day both the direct and reflected irradiance increases. The direct irradiance on both the solar cell as the reflecting surfaces are dependent on the DNI, AOI and the SF. The SF is modeled by considering the skyline profile. The accuracy of the skyline profile is determined by the angular resolution chosen. For the solar cell an high angular resolution of 1^o is chosen while for the reflecting surface an angular resolution of 8^o was chosen. It is suspected that the 8^o angular resolution is not high enough and is the reason why on the sunny day the model is giving worse results than on the overcast day. Another source of difference is the isotropic assumption which the 3D VF model is based on. As the earlier chapter shows that considering tilted or sky blocked situation variations start to appear between the isotropic diffuse sky model and the ray tracing models on the luminance distribution of circumsolar and diffuse light across the sky. Also for the reflecting surfaces the reflected irradiance was neglected. In reality this is not the case and should also be considered like the other ray tracing models do.
Which simulation model gives the closest prediction with the actual measurements is difficult to compare with actual measurements. Because the chosen input variables such as albedo, DNI and DHI also can have a certain error, while the actual value can lead to completely different results. For example the simple DHI correction that was made negatively impacted the backwards ray tracing model in some situations, however it positively impacted the other simulation models. But even this DHI does not have to be the actual DHI because it also is dependent on reflected light received by the Solys 2. Additionally, also the level of accuracy that is set for each model is different. This is why the purpose of comparing the other models was not to choose the best performing model but rather use as a benchmark for the 3D VF model that was validated. And after comparison with the other ray tracing simulation models looking at the RMSE results it can be concluded that the 3D VF model is capable of predicting the actual measurement competitively with the other models considered.

6

Conclusions and recommendations

6.1. Conclusions

This research aimed to investigate the current bifacial simulation tools commercially available, and identify their shortcomings or challenges when using these modeling tools within more complex urban landscapes. The aforementioned research objective aimed to be answered with this study was summarized into one main research question. Defined as followed:

- **How and with which type of modeling framework can the irradiance received on a bifacial (BI)PV system be simulated while considering the impact of surrounding objects that can cause shading on such a system?**

The main research question was subdivided into different sub-questions, answered throughout the research. In the following paragraph the obtained answers to each sub-question are given.

The first research question was defined as:

- **What are the most relevant variables influencing the irradiance a bifacial PV system receives?**

An answer to this question is provided in chapter 2 and partly in chapter 3. Bifacial PV, unlike monofacial PV, is able to utilize solar irradiation incident on both sides. The back side of the bifacial PV module generally receives mostly reflected irradiance and depending on how visible the skydome is also diffuse irradiance. This is because similar to monofacial modules the front side of a bifacial module is oriented in such a way it can receive the maximum amount of irradiance, and thus generally points towards the sky. So the back side is mostly facing the ground.

The amount of irradiation both the front and back sides receive depends on different installation parameters such as; tilt, azimuth, stand off height, albedo, system size and cell spacing. The tilt, azimuth and system size usually directly influence the amount of irradiance both the front and back side receives. But since the back side mostly receives reflected light from surroundings other parameters become relevant such as stand off height, cell spacing and albedo. Also important is the role of shading for the irradiance the front and back side of the bifacial modules receive. A distinction between self/mutual shading and ground/surface reflected-shading is important for bifacial PV. For the back side, since reflected and diffuse irradiance dominate, ground reflected shading becomes important. Because just like the front side of the bifacial PV module also the surrounding surfaces receive direct, diffuse and reflected irradiance which sequentially gets reflected onto the back side of the bifacial PV module.

In Fig. 3.3 for each of the simulation parameter, it was shown what the effect is on the irradiation received on the back of a bifacial PV module in a free horizon environment. The graphs show a positive increasing trend for the tilt, stand off-height, albedo and cell spacing installation parameters. Some of the installation parameters also depend on each other. An interesting example that was given was the interdependence of the cell spacing and stand off height. In this example, it was shown how the cell spacing becomes more relevant at a lower stand off height.

- **How do different existing models perform in different environments, ranging from free horizon to more complex urban landscapes?**

Different modeling frameworks exist for simulating the irradiance received on the front and back side of bifacial PV systems. They can be categorized into empirical, view factor and ray tracing models. The different simulation methods differ in input parameters considered, simulation time and accuracy of predictions. In chapter 3 it was identified that only the 3D VF, the backward and forward ray tracing methods fulfill all the requirements to simulate the back side irradiance in more complex urban environments. While these models, after choosing a high enough accuracy setting, can closely predict the irradiance a bifacial PV would receive. A big difference is noticed in the simulation time required for arriving at this prediction. Out of the existing simulation models, the backward ray tracing performed with Radiance was identified as the fastest simulation tool for modeling yearly irradiation of a single bifacial module under free horizon conditions.
Instead of the Sandia implementation of the 3D VF model in chapter 4 a new 3D VF simulation model based on the ray casting method was developed since this is better suited for urban environments. Through a series of sanity checks, it can be concluded that the developed 3D VF model can be competitive for both the front and back irradiance on bifacial solar modules compared with the ray tracing models. It was also noticed that a higher tilt directly results in a difference noticed between the calculations based on the simplified mathematical formulas or the 3D VF model and the ray tracing models. This is suspected to be because the later is based on more complex luminance distribution of circumsolar and diffuse light across the sky, while the earlier assumes isotropic sky. When considering the front irradiance for the 0 degree tilted 3 by 3 celled solar module the irradiance value incident on each cell should be the same. This only proved to be the case for the 3D VF and the backward ray tracing simulation. However, for the forward ray tracing a significant difference of 8 W/m^2 was obtained between the different solar cells. Even though for the simulations a very high accuracy setting was chosen, namely a ray density of around 13 thousand per square meter and a sky subdivision into 10240 sky patches. Also, significant difference can be observed considering the 3D VF model calculations under partial shading conditions. This is because the incident irradiance is measured at the center of each cell instead of across the cell like ray tracing models.

- **How do the simulation models compare to real-life measurements?**

An answer to this question is given in chapter 5. The simulation models are compared with pyranometer measurements taken at the dual and fixed axis trackers on the PVMD monitoring station, since their orientation was fixed throughout the measurement period they are referred to as POA 1 and POA 2 respectively. Two measurement days are considered, a fully overcast day and a clear sunny day. For the overcast day, an relative RMSE value of 23.09% and 11.7% are achieved for POA 1 and 2 for calculations with the 3D VF model. For both cases the irradiation was mostly underestimated, considering the negative MBE and positive MAE. On the clear sunny day, relative RMSE values of 20.35% and 5.26% are achieved for POA 1 and 2 with the 3D VF based model. The model also again mostly underestimates considering the negative MBE and positive MBA values. With POA 2 having more instances where the irradiance is overestimated but overall is the irradiation underestimated.
A simplified correction on the DHI measurement, neglecting reflected irradiance also measured at Solys 2, is performed. After correction, an relative RMSE value of 19.96% and 5.2% are achieved for POA 1 and 2 was calculated on the overcast day. While on the sunny day relative RMSE values of 19.38% and 3.77% are achieved for POA 1 and 2 respectively.

The actual DHI is a value between the measured and the corrected DHI, because of the reflected irradiance also measured at the Solys 2. Because of this it can be concluded that if 3D VF calculations are performed with the real DHI the minimum relative RMSE would be 19.96% POA 1, and 5.2% for POA 2 on the overcast day. While on the clear sunny day the minimum relative RMSE is around 19.38% POA 1, and 3.77% for POA 2. Using the other simulation models as a benchmark it can be concluded that the 3D VF model is capable of predicting the actual measurement competitively compared to the other ray tracing models.

6.2. Recommendations

Next recommendations are made for potential future research. The recommendations are based on either new questions that arose during research or research questions that where left unanswered due to time constraints. These recommendations address either the 3D vF model that was developed, the comparison made with the other ray tracing models or recommendations that can be made at the monitoring station. For this reason the following paragraphs are presented accordingly.

6.2.1. Recommendations for 3D VF model based on ray casting method

- **Expanding 3D VF model with reflected irradiation on surrounding surfaces**

  The first concept of the 3D view factor implementation made in the Rhinoceros and Grasshopper software calculated the irradiance on surrounding surfaces based on Equations 2.20 and 2.19. According to this formula the irradiance surrounding surfaces does not receive reflected irradiance from the environment. In other words the G_{Ground} term in Equation 2.9 is neglected. And thus only the solar cell or pyranometer receives reflected irradiance. However, in reality the irradiance the surrounding surfaces receives also consist of reflected irradiance from the environment. This term was initially neglected because this would result in a long simulation time, while also long simulations needed to be performed with the forward and backward ray tracing models. Additionally the contribution of this term was expected to be small. For future research it is however recommended to also consider the reflected irradiance term from Equation 2.9 for the surrounding surface and analyse the implication on the total irradiance received.

- **Diffuse sky model**

  The diffuse irradiance on a receiving surface can be calculated with different models like; Isotropic, Hay en Davies or simplified Perez and luminance sky destribution models, each increasing in complexity. During the research it was shown how the irradiance result on a receiving surface can highly depend on the diffuse sky model the simulation model is based on. In order to have an even comparison the 3D VF model also needs to be equiped with the luminance distributed sky model, similar to the ray tracing models considered.

- **Matlab implimentation:**

  The 3D VF model based on the ray casting method was implemented in the Rhinoceros and Grasshopper software. The main reason for implementing the 3D VF model in the Rhinoceros and Grasshopper software was to ensure uniformity between the different simulation models. Since the CAD design tool Rhinoceros could be used for constructing the 3D environment and 3D design could either be uploaded in the Grasshopper/Ladybug/Honeybee plug-in for running the simulations in the intended 3D VF and backward ray tracing simulations or LightTools for running the forward ray tracing simulations. Whether this is ultimately the fastest simulation method was not investigated. It is known that the simulations can also be performed in Matlab software, which easily allows matrix manipulations, plotting of functions and data, implementation of algorithms. Since the simulation time is important and existing simulation tools have shown a big difference in simulation time required it is interesting to also implement the 3D VF model in Matlab in order to compare the simulation time required with different existing models.

- **Effect of mirrors and glass windows**

  The reflecting surfaces considered within this research for simplicity where all assumed to be lambertian. Also for the validation simulations that was performed at the monitoring station the surfaces where taken to be lambertian. The reason for doing this was to make an first estimation of irradiance measurements with the ray casting method. However at the monitoring station there are surrounding windows or other glass surfaces that could cause specular reflection. An example is the highest section of the WKC building in front of the dual axis traker and also the InHolland façade on the northside of the monitoring station roof area. For situations where specular reflection may occur the 3D VF model needs to be equipped with the requirements for calculating the specular reflection.

6.2.2. Recommendation for model comparison

- **Reflected irradiance component simulation ray tracing models**

  The 3D VF model is capable of separately calculating the reflected irradiance or irradiation with Equations 2.20 and 2.19. This unfortunately is not inherently possible with the ray tracing models. A method for calculating only the reflected irradiance component is by with the ray tracing models is by subtracting the total irradiance with a total irradiance when all surrounding surfaces have an zero albedo value. The difference is the reflected irradiance. Unlike the earlier simulation this requires each simulation to be performed twice. One simulation with each surface having the actual albedo and the second simulation with each surface having a zero value of albedo.

- **Forward ray tracing simulation with varying aim area**

  During the comparison studies throughout the research a aim area of the forward ray tracing simulation was taken based on the distance of potential reflecting surrounding surfaces. When all reflecting building are taken within the aim area as was done in Chapter 4 the forward ray tracing simulation result shows almost now difference with other simulation models. The aim area however becomes a problem the larger the 3D scene that needs to be simulated. A clear example is the monitoring station environment in Chapter 5. This scene is so large that if all the reflecting surfaces would have to fall within the aim area the number of rays for ensuring a high enough ray density would result in an extremely long simulation time. This is why the aim area was taken only covering the monitoring roof area with a radius of 14 meter and an ray density of 16 thousand per square meter. However, it is recommended to also perform simulations with an different aim areas to see how this affects the forward ray tracing model predictions.

6.2.3. Recommendation for monitoring station setup

- **Irradiance measurements on the back of POA 1 and 2**

  In this research the 3D VF model was validated for what can be considered a typical front/back side of a east-west bifacial PV module configuration at POA 1. And what can be considered a front side of a 30 degree tilted bifacial PV module at POA 2. It is also interesting to validate the performance for the back side of the tilted POA 2 bifacial PV module, since for this configuration the reflected irradiance would contribute the largest share of the total irradiance received. For this a similar pyranometer as the POA 2 pyranometer needs to be placed on the top of the rack with it's orientation facing the ground. The pyranometer also needs to be connected to the monitoring portal where measurements are taken simultaneously as the other measurements and timestamped accordingly.

- **Impact of different surface albedos**

  It would additionally also be interesting to construct a measuring setup where measurement is taken behind a module facing a single ground surface that consists of a single material. The setup could be made in such a way that the material underneath can be easily changed. If that was the after calculating the albedo of that single surface material, this albedo can be used during simulations. Additionally, it could also allow to research the effect of different albedo conditions. Because in this research all the validation measurements a single average albedo was taken since the surrounding surfaces consist of too many surfaces to consider individually.

Bibliography

[1] International Energy Agency (IEA). Trends in photovoltaic applications 2018.

[2] ITRPV. Results 2017 including maturity report 2018, ninth edition, september 2018.

[3] Claudia Duran. *Bifacial Solar Cells : High Efficiency Design, Characterization, Modules and Applications*. PhD thesis, Universität Konstanz, Konstanz, 2012.

[4] R Kopecek and J Libal. Towards large-scale deployment of bifacial photovoltaics. *Nature Energy*, 3(6):443, 2018.

[5] Darren Robinson and Andrew Stone. Irradiation modelling made simple: the cumulative sky approach and its applications. In *PLEA Conference*, pages 19–22, 2004.

[6] Isa Zanetti, Pierluigi Bonomo, Francesco Frontini, Erika Saretta, Menno van den Donker, Finn Vossen, and Wiep Folkerts. Building integrated photovoltaics: Product overview for solar building skins-status report 2017. *Kidlington, UK*, 2017.

[7] Karoline Fath, Julian Stengel, Wendelin Sprenger, Helen Rose Wilson, Frank Schultmann, and Tilmann E Kuhn. A method for predicting the economic potential of (building-integrated) photovoltaics in urban areas based on hourly radiance simulations. *Solar energy*, 116:357–370, 2015.

[8] P Redweik, Cristina Catita, and Miguel Brito. Solar energy potential on roofs and facades in an urban landscape. *Solar Energy*, 97:332–341, 2013.

[9] Andres Calcabrini, Juan Camillo Ortiz Lizcano, Hesan Ziar, and Olindo Isabella. Photovoltaic systems instruction ii. University Lecture, 2019.

[10] Axel Jacobs. Radiance tutorial, 2012.

[11] International Energy Agency (IEA). World energy outlook 2016: Executive summary.

[12] International Energy Agency (IEA). Technology roadmap: Solar photovoltaic energy, 2017.

[13] John Conti, Paul Holtberg, Jim Diefenderfer, Angelina LaRose, James T. Turnure, and Lynn Westfall. International energy outlook 2016 with projections to 2040. 5 2016.

[14] Fabian Fertig, Sebastian Nold, Nico Wöhrle, Johannes Greulich, Ingrid Hädrich, Karin Krauß, Max Mittag, Daniel Biro, Stefan Rein, and Ralf Preu. Economic feasibility of bifacial silicon solar cells. *Progress in photovoltaics: research and applications*, 24(6):800–817, 2016.

[15] Tian Shen Liang, Mauro Pravettoni, Chris Deline, Joshua S. Stein, Radovan Kopecek, Jai Prakash Singh, Wei Luo, Yan Wang, Armin G. Aberle, and Yong Sheng Khoo. A review of crystalline silicon bifacial photovoltaic performance characterisation and simulation. *Energy Environ. Sci.*, 12:116–148, 2019.

[16] European Commission. Energy performance of buildings.

[17] Raphael Bointner, Ramón Pascual, Giulia Paoletti, and Filippos Anagnostopoulos. Nearly zero-energy building strategy 2020. Technical report, 2014.

[18] International Energy Agency (IEA). Renewables 2018: Analysis and forecast to 2023, 2018.

[19] Silvana Ayala Pelaez, Chris Deline, Sara M MacAlpine, Bill Marion, Joshua S Stein, and Raymond K Kostuk. Comparison of bifacial solar irradiance model predictions with field validation. *IEEE Journal of Photovoltaics*, 9(1):82–88, 2019.

[20] Clifford W Hansen, Joshua S Stein, Chris Deline, Sara MacAlpine, Bill Marion, Amir Asgharzadeh, and Fatima Toor. Analysis of irradiance models for bifacial pv modules. In *Photovoltaic Specialists Conference (PVSC), 2016 IEEE 43rd*, pages 0138–0143. IEEE, 2016.

[21] Claudia Duran. *Bifacial solar cells: high efficiency design, characterization, modules and applications*. PhD thesis, 2012.

[22] Andrés Cuevas et al. The early history of bifacial solar cells. 2005.

[23] R. Guerrero-Lemus, R. Vega, Taehyeon Kim, Amy Kimm, and L.E. Shephard. Bifacial solar photovoltaics – a technology review. *Renewable and Sustainable Energy Reviews*, 60:1533 – 1549, 2016.

[24] Jai Prakash Singh, Timothy M Walsh, and Armin G Aberle. A new method to characterize bifacial solar cells. *Progress in Photovoltaics: Research and Applications*, 22(8):903–909, 2014.

[25] Olindo Isabella, Arno Smets, Klaus Jäger, Miro Zeman, and René van Swaaij. Solar energy: The physics and engineering of photovoltaic conversion, technologies and systems. *UIT Cambridge Limited*, 2016.

[26] Amir Asgharzadeh, Tomas Lubenow, Joseph Sink, Bill Marion, Chris Deline, Clifford Hansen, Joshua Stein, and Fatima Toor. Analysis of the impact of installation parameters and system size on bifacial gain and energy yield of pv systems. In *2017 IEEE 44th Photovoltaic Specialists Conference (PVSC)*, 2017.

[27] Jouri Kanters and Henrik Davidsson. Mutual shading of pv modules on flat roofs: a parametric study. *Energy procedia*, 57:1706–1715, 2014.

[28] J. E. Castillo-Aguilella and P. S. Hauser. Multi-variable bifacial photovoltaic module test results and best-fit annual bifacial energy yield model. *IEEE Access*, 4:498–506, 2016.

[29] Solarworld. Sunmodule bisun boost calculator, 2019.

[30] Bill Marion, Sara MacAlpine, Chris Deline, Amir Asgharzadeh, Fatima Toor, Daniel Riley, Joshua Stein, and Clifford Hansen. A practical irradiance model for bifacial pv modules. In *44th IEEE Photovolt. Spec. Conf*, 2017.

[31] Clifford W Hansen, Renee Gooding, Nathan Guay, Daniel M Riley, Johnson Kallickal, Donald Ellibee, Amir Asgharzadeh, Bill Marion, Fatima Toor, and Joshua S Stein. A detailed model of rear-side irradiance for bifacial pv modules. *44th IEEE PVSC. Washington DC*, 2017.

[32] A. Mermoud and B. Wittmer. Pvsysts new framework to simulate bifacial systems. PVPMC Workshop, 2016.

[33] R Santbergen, V.A. Muthukumar, R.M.E. Valckenborg, W.J.A. van de Wall, Arno Smets, and Miro Zeman. Calculation of irradiance distribution on pv modules by combining sky and sensitivity maps. *Solar Energy*, 150:49–54, 07 2017.

[34] M Kutzer, A Fülle, A Jahnke, JBH Hahn, S Wendt, DH Neuhaus, A Witzig, and KM Kutzer. Ertragssteigerung durch bifaciale modultechnologie. In *Proc. 31st Symp. Photovolt. Sol. Energy*, pages 1–10, 2016.

[35] Hoyt C Hottel and BB Woertz. Evaluation of flat-plate solar heat collector. *Trans ASME*, 64:91, 1942.

[36] JA Davies and JE Hay. Calculation of the solar radiation incident on an inclined surface in proc. In *First Canadian Solar Radiation Data Workshop (JE Hay and TK Won, eds.)*, pages 32–58, 1978.

[37] Richard Perez, Pierre Ineichen, Robert Seals, Joseph Michalsky, and Ronald Stewart. Modeling daylight availability and irradiance components from direct and global irradiance. *Solar energy*, 44(5):271–289, 1990.

[38] Radsite. Radiance.

[39] COMSOL. Comsol multiphysics® 5.5.

[40] Synopsys. Lighttools illumination design software.

[41] Christoph F Reinhart and Sebastian Herkel. The simulation of annual daylight illuminance distributions—a state-of-the-art comparison of six radiance-based methods. *Energy and buildings*, 32(2):167–187, 2000.

[42] Greg Ward and Rob Shakespeare. Rendering with radiance: the art and science of lighting visualization. 1998.

[43] S Freitas and MC Brito. Bifacial pv integrated on building balconies. In *32nd European Photovoltaic Solar Energy Conference and Exhibition. Munich, Germany*, 2016.

[44] NREL. bifacial_radiance, 2019.

[45] R Santbergen, VA Muthukumar, RME Valckenborg, WJA van de Wall, AHM Smets, and M Zeman. Calculation of irradiance distribution on pv modules by combining sky and sensitivity maps. *Solar Energy*, 150:49–54, 2017.

[46] Rhinoceros. Rhino 6 features.

[47] Iea Pvps. Trends 2017 in photovoltaic applications, 03 2017.

[48] Cristina Catita, Paula Redweik, J Pereira, and Miguel Centeno Brito. Extending solar potential analysis in buildings to vertical facades. *Computers & Geosciences*, 66:1–12, 2014.

[49] Harry Lehmann and Stefan Peter. Assessment of roof & façade potentials for solar use in europe. *Institute for sustainable solutions and innovations (ISUSI): Aachen, Germany*, 2003.

[50] Chris Deline, Sara MacAlpine, Bill Marion, Fatima Toor, Amir Asgharzadeh, and Joshua S Stein. Assessment of bifacial photovoltaic module power rating methodologies—inside and out. *IEEE Journal of photovoltaics*, 7(2):575–580, 2017.

[51] SPOT Pro. Rradiance parameters, 2019.

[52] Furkan Fatih Sönmez, Hesan Ziar, Olindo Isabella, and Miro Zeman. Fast and accurate ray-casting-based view factor estimation method for complex geometries. *Solar Energy Materials and Solar Cells*, 200:109934, 2019.

[53] Do C Hamilton and WR Morgan. Radiant-interchange configuration factors. 1952.

[54] Meteonorm. Horicatcher.

[55] JA Coakley. Reflectance and albedo, surface. *Encyclopedia of the Atmosphere*, pages 1914–1923, 2003.

[56] Tianfeng Chai and Roland R Draxler. Root mean square error (rmse) or mean absolute error (mae)?–arguments against avoiding rmse in the literature. *Geoscientific model development*, 7(3):1247–1250, 2014.

Appendix A

This appendix shows all information from the Grasshopper file that was used for performing the ray casting as described in Chapter 4. In Fig. 6.1 a block diagram is presented indicating the different steps taken within the Grasshopper file. In Fig. 6.2 the Grasshopper canvas with the irradiance model is indicated.

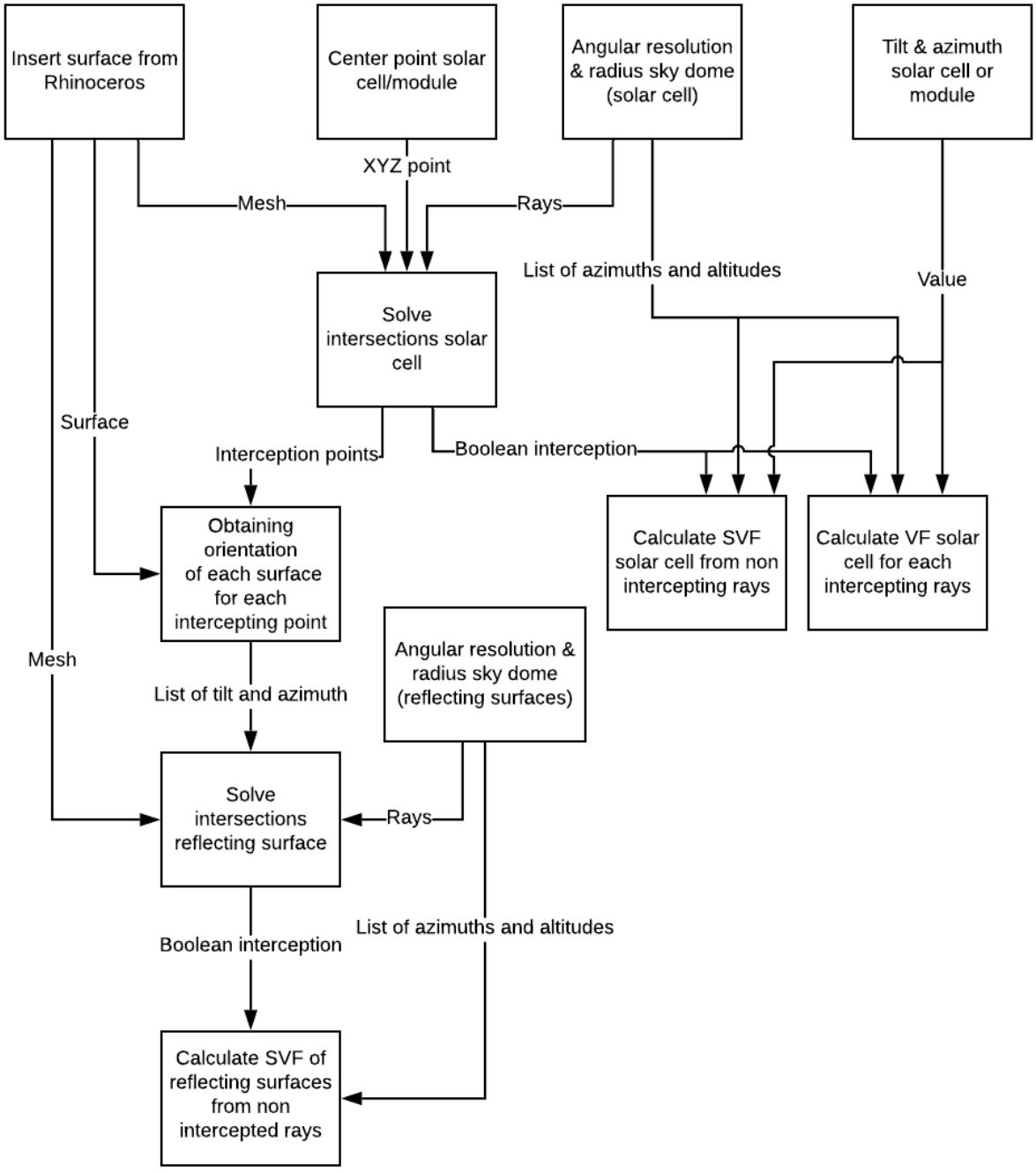

Figure 6.1: Block diagram showing the different steps performed in the Grasshopper software.

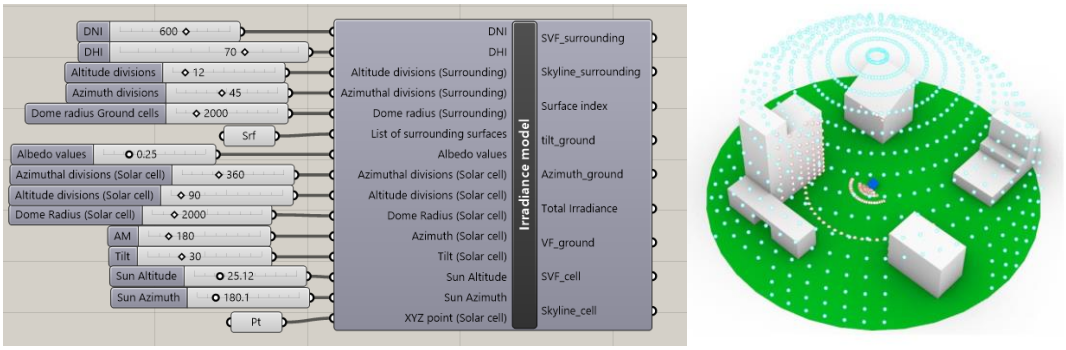

Figure 6.2: On the left the Grasshopper canvas of the irradiance model, including the required input variables. On the right the Rhino interface displaying the model in an urban environment. The blue dots indicate ray that has been cast without an interception with obstruction nearby. Brown dots indicate the intercepted point of the cast ray and the obstruction or ground.

As can be seen in the block diagram and the Grasshopper model the first step is adding the surfaces drawn in the Rhinoceros software and choosing desired values for the tilt, azimuth and the center point of the solar cell/module in xyz coordinates. Also, an appropriate value for the angular resolution and radius to determine the direction of the rays to be cast. For an angular resolution of 1 degree for example, within the Grasshopper file a series of altitude and azimuth is created. Ranging from .5 to 89.5 and .5 to 359.5 for altitude and azimuth respectfully. Additionally, also a negative altitude range is created for casting rays in the direction of the ground below. Next, the series is translated into xyz points, moved from the origin to the center of the solar cell and multiplied with the radius value chosen. These points form the endpoint of a line along which the rays will be cast. The setup of the rays, the list of altitude and azimuth values in the Grasshopper file is illustrated in Fig. 6.3.

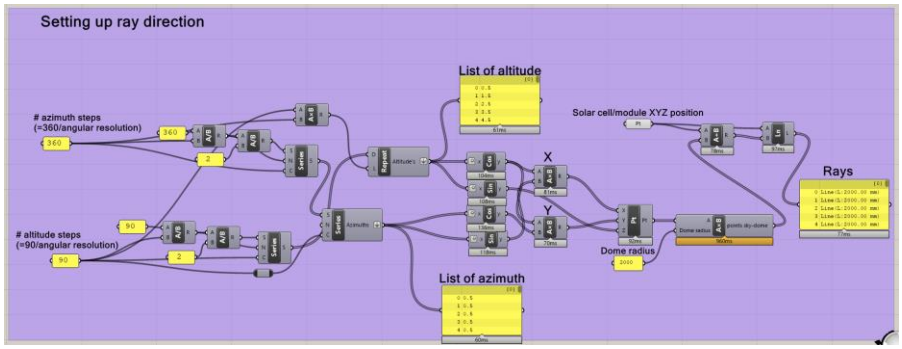

Figure 6.3: Grasshopper canvas of the blocks for setting up of the ray direction.

The list of altitude and azimuth values are used for calculating the Sky View Factor (SVF) and surrounding view factor ($VF_{i\rightarrow k}$) later on. Next, the intersections of the rays with the scene are solved to determine the (un)blocked sky. This is done using the "Mesh|Ray" block within Grasshopper. The surfaces are first meshed and joined. The output of the "Mesh|Ray" block is a list of boolean values, being true when an obstacle was intercepted by a ray and false otherwise. With a "gate not" block the skyline profile can be constructed from the boolean values for calculating the SF. Another output of the "Mesh|Ray" block is the xyz point of interception on the intercepted surfaces. The ray interception setup in Grasshopper is illustrated in Fig. 6.4.

Before the SVF is calculated first the altitude and azimuth of intercepted rays are filtered out. Next, the SVF of each sky sector is calculated using Equation [25]:

$$SVF = \left[sin(\theta_M)cos(\alpha)cos(Az_M - Az) + cos(\theta_M) \cdot sin(\alpha) \right] \cdot \frac{cos(\alpha) \cdot \pi}{\delta\alpha\delta Az} \tag{6.1}$$

With θ_M and Az_M being the tilt and azimuth angle of the solar cell or surrounding surface. α and Az being the tilt and azimuth angle of the cast rays. And lastly, $\delta\alpha$ and δAz being the angular resolution of the altitude and azimuth. The $VF_{i\rightarrow k}$ is calculated in a similar method with the main difference being that now the non intercepted rays are filtered out. Next, the orientation of the surface at each intercepted point needs

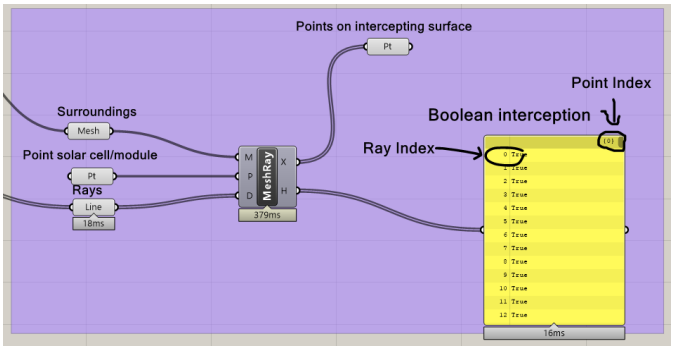

Figure 6.4: Grasshopper canvas of the blocks solving the ray interceptions.

to be determined. This is done using the list of surfaces from the Rhinoceros software and the points from the "Mesh|Ray" block mentioned earlier. For each point, it needs to be determined with which surface from the list its intercepts. This is done by first projecting each point onto the surfaces. Each projection has a certain distance from the point to the surface. When this distance is (close to) zero the point is on the surface. This condition is also used within the Grasshopper file for determining the intercepting surface. For each intercepting surface, the tilt and azimuth are calculated using the normal. The setup for determining the orientation of the surface each ray intercepts in the Grasshopper file is illustrated in Fig. 6.4. Now that the

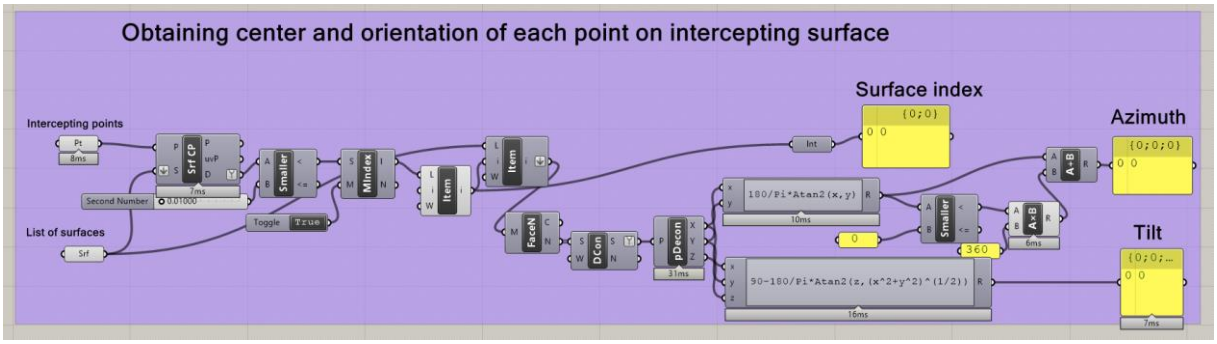

Figure 6.5: Grasshopper canvas of the blocks for obtaining the orientation of the surface each ray intercepts with.

tilt, azimuth and intercepting point is known, in a similar method as described earlier the interceptions of the rays with the scene can be determined followed by the SVF calculation for all the reflecting surroundings. With all the variables SVF_{cell}, SVF_{sur}, $VF_{i \rightarrow k}$ and the skyline profile known the irradiance at different time instances can be calculated. This is done within the Matlab software.

Appendix B

3D VF compared with ray tracing
In the following chapter the simulation results of the of the three comparison checks discribed in chapter 4 is given. For the comparison three conditions where set up.

- **Check 0:** Simulation of front side irradiance on a single 1 m^2 south facing solar module, under free horizon conditions. Also comparing the three models with similar calculations based on Eq. 2.9 to 2.15 described earlier.
- **Check 1:** Simulation of front- and back side irradiance on a 3 by 3 celled south facing solar module, again under free horizon conditions. At time instances when the sun is facing southeast and directly south.
- **Check 2:** And lastly considering the same 3 by 3 solar module, where part of the sky is blocked by an object. Considering the sun at a position where the solar module is unshaded and partially shaded.

An illustration of the setup for each check is given in the Fig. 6.6.

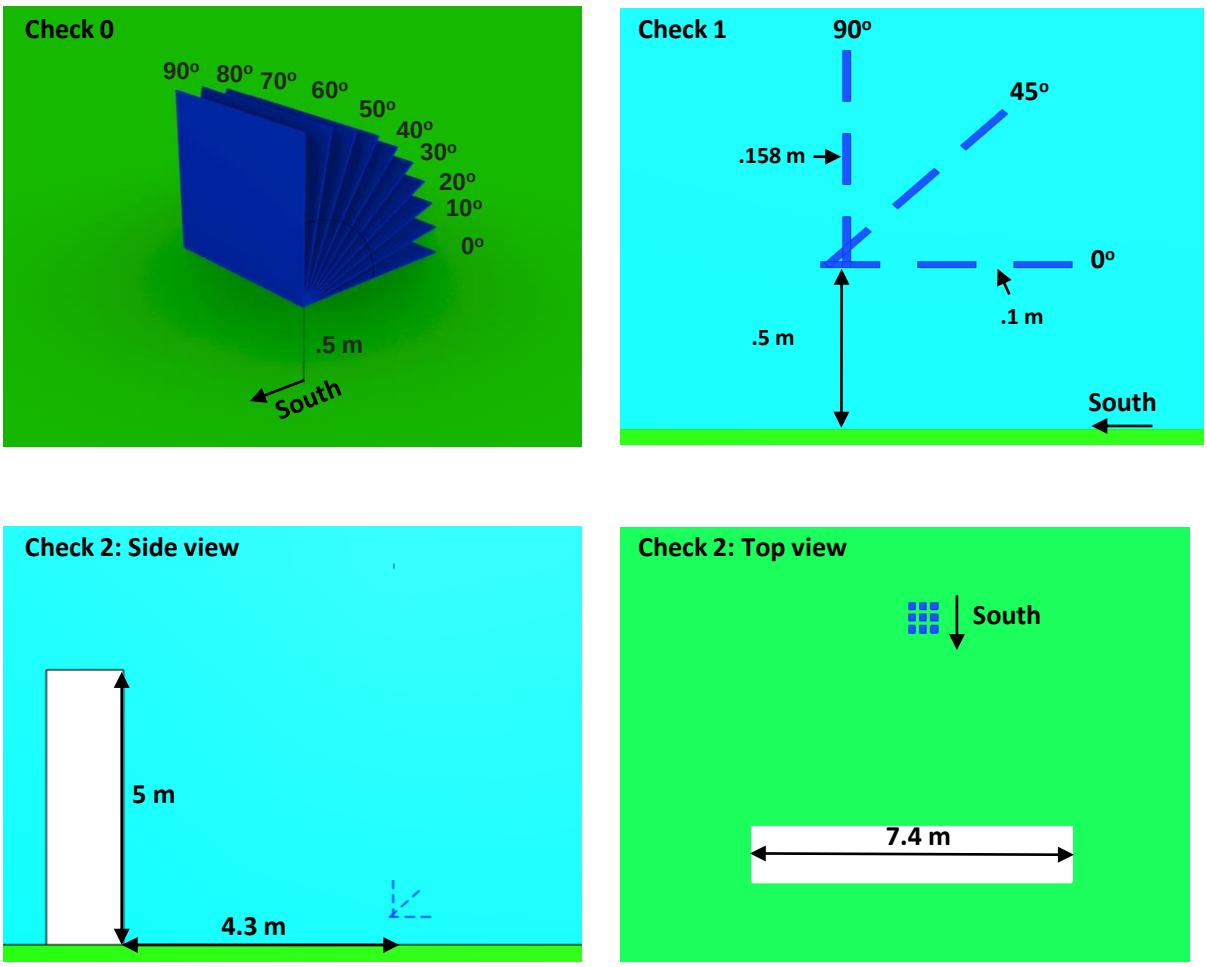

Figure 6.6: Illustration of the dimensions considered for each check.

In the tables below the simulation results in W/m^2 are given.

Result check 0: 1m² solar module

Tilt	Calculated	3D VF	Backward RT	Forward RT	Forward RT (Isotropic sky)
0	326	326	322	323	323
10	363	363	365	367	361
20	391	391	399	402	390
30	410	410	423	427	409
40	419	419	437	440	418
50	417	417	439	442	416
60	405	405	430	434	405
70	383	383	410	415	384
80	351	351	379	383	352
90	311	311	338	343	313

Result check 1: 9 solar cells including .1 m cell spacing

			3D VF		Backward RT		Forward RT	
Tilt	**Cell**	**Time**	**front**	**back**	**front**	**back**	**front**	**back**
0	1	*t1: sun eastwest*	325.9	80.8	321.9	78.9	320.6	78.8
		t2: sun south	481.0	106.9	478.0	116.3	476.0	121.0
	2	*t1: sun eastwest*	325.9	80.6	321.9	79.4	326.9	83.4
		t2: sun south	481.0	105.3	478.0	115.9	481.2	115.8
	3	*t1: sun eastwest*	325.9	80.8	321.9	79.8	329.0	79.7
		t2: sun south	481.0	108.1	478.0	116.3	483.3	116.0
	4	*t1: sun eastwest*	325.9	80.6	321.9	78.1	323.7	76.7
		t2: sun south	481.0	112.7	478.0	112.5	482.3	118.7
	5	*t1: sun eastwest*	325.9	80.5	321.9	79.1	322.1	77.2
		t2: sun south	481.0	111.5	478.0	111.3	482.9	116.5
	6	*t1: sun eastwest*	325.9	80.6	321.9	79.6	323.7	77.2
		t2: sun south	481.0	112.8	478.0	112.5	479.1	115.3
	7	*t1: sun eastwest*	325.9	81.3	321.9	77.4	321.6	73.6
		t2: sun south	481.0	116.5	478.0	107.0	480.2	104.7
	8	*t1: sun eastwest*	325.9	81.1	321.9	78.8	323.7	78.1
		t2: sun south	481.0	115.9	478.0	104.6	485.5	107.4
	9	*t1: sun eastwest*	325.9	81.3	321.9	79.5	324.8	86.0
		t2: sun south	481.0	116.3	478.0	107.1	483.4	102.6

45	1	*t1: sun eastwest*	419.3	74.3	439.4	79.4	441.0	75.5
		t2: sun south	677.1	112.5	704.4	110.5	702.0	114.0
	2	*t1: sun eastwest*	419.3	75.9	439.4	79.9	441.3	72.3
		t2: sun south	677.1	112.5	704.4	109.9	708.3	103.0
	3	*t1: sun eastwest*	419.3	77.6	439.4	80.2	449.3	80.2
		t2: sun south	677.1	112.6	704.4	110.5	705.2	101.6
	4	*t1: sun eastwest*	419.3	75.9	439.7	79.4	439.5	78.2
		t2: sun south	677.1	112.6	704.4	109.2	701.9	108.8
	5	*t1: sun eastwest*	419.3	76.2	439.2	79.8	439.4	79.2
		t2: sun south	677.1	112.6	704.4	108.5	700.7	100.2
	6	*t1: sun eastwest*	419.3	77.0	439.7	80.1	444.2	79.7
		t2: sun south	677.1	112.6	704.2	109.1	702.7	107.0
	7	*t1: sun eastwest*	419.3	78.0	439.5	79.3	437.6	77.4
		t2: sun south	677.1	112.8	704.6	109.3	703.4	110.7
	8	*t1: sun eastwest*	419.3	78.0	439.5	80.0	450.9	77.2
		t2: sun south	677.1	112.8	704.4	108.7	698.6	99.3
	9	*t1: sun eastwest*	419.3	78.3	439.5	80.4	445.1	78.0
		t2: sun south	677.1	112.8	704.4	109.3	713.1	101.3
90	1	*t1: sun eastwest*	311.4	75.8	338.1	71.9	344.8	71.1
		t2: sun south	528.6	95.1	565.5	88.4	555.8	85.7
	2	*t1: sun eastwest*	311.4	75.8	338.1	72.1	339.7	72.2
		t2: sun south	528.1	95.1	565.5	88.1	563.4	87.9
	3	*t1: sun eastwest*	311.4	75.8	338.2	72.2	333.5	69.2
		t2: sun south	527.8	95.1	565.5	88.4	562.5	88.4
	4	*t1: sun eastwest*	311.4	75.7	338.2	72.0	344.8	74.7
		t2: sun south	529.5	95.1	565.6	89.1	562.4	83.9
	5	*t1: sun eastwest*	311.4	75.8	338.3	72.2	342.9	70.5
		t2: sun south	529.1	95.1	565.6	89.3	556.3	80.3
	6	*t1: sun eastwest*	311.4	75.8	338.2	72.2	343.7	70.3
		t2: sun south	529.1	95.1	565.6	89.1	557.0	82.1
	7	*t1: sun eastwest*	311.5	75.7	338.6	72.3	338.2	70.6
		t2: sun south	530.4	95.1	565.6	89.7	543.0	85.1
	8	*t1: sun eastwest*	311.5	75.8	338.4	72.2	348.0	69.8
		t2: sun south	530.1	95.2	565.6	89.5	556.4	83.3
	9	*t1: sun eastwest*	311.5	75.8	338.4	72.3	336.4	63.2
		t2: sun south	530.2	95.1	565.9	89.7	557.6	81.2

Result check 2: building facing 9 solar cells including .1 m cell spacing

Tilt			3D VF		Backward RT		Forward RT	
	Cell	Time	front	back	front	back	front	back
0	1	*t1: partially shaded*	320.0	30.7	314.8	30.6	312.9	30.3
		t2: unshaded	319.6	21.3	282.2	19.1	284.7	16.3
	2	*t1: partially shaded*	320.0	30.9	315.2	30.8	319.7	32.6
		t2: unshaded	64.2	16.6	52.3	14.2	53.4	14.7
	3	*t1: partially shaded*	320.0	31.0	315.5	31.0	322.4	31.0
		t2: unshaded	64.2	12.7	51.7	10.4	52.7	9.6
	4	*t1: partially shaded*	320.5	30.4	315.4	30.4	316.8	29.8
		t2: unshaded	320.2	24.9	303.9	22.8	300.7	24.1
	5	*t1: partially shaded*	320.6	30.8	315.7	30.8	315.8	30.1
		t2: unshaded	320.2	20.5	252.3	18.3	256.2	19.4
	6	*t1: partially shaded*	320.6	31.1	316.1	31.1	317.5	30.1
		t2: unshaded	64.7	16.1	53.0	13.4	54.1	13.7
	7	*t1: partially shaded*	321.1	30.2	315.9	30.2	315.4	28.4
		t2: unshaded	320.8	27.1	305.1	25.4	307.5	26.5
	8	*t1: partially shaded*	320.8	30.7	316.3	30.8	317.6	30.4
		t2: unshaded	320.7	24.2	304.0	22.0	308.7	22.2
	9	*t1: partially shaded*	321.1	31.3	316.5	31.1	319.1	33.7
		t2: unshaded	320.8	19.9	201.9	17.2	205.5	16.9
45	1	*t1: partially shaded*	396.2	36.7	410.7	38.7	412.8	37.3
		t2: unshaded	517.2	33.6	496.5	32.9	501.5	32.1
	2	*t1: partially shaded*	396.4	37.0	411.6	39.0	414.9	36.2
		t2: unshaded	45.0	30.8	54.6	29.5	55.0	28.5
	3	*t1: partially shaded*	396.5	36.9	412.6	39.1	423.3	39.4
		t2: unshaded	47.2	27.2	52.7	26.2	53.8	26.5
	4	*t1: partially shaded*	397.0	36.6	411.9	38.8	413.9	38.5
		t2: unshaded	518.0	34.4	528.0	34.1	526.6	34.1
	5	*t1: partially shaded*	397.8	37.0	412.7	39.0	413.6	39.0
		t2: unshaded	516.5	32.3	248.7	31.8	268.8	28.9
	6	*t1: partially shaded*	397.2	37.2	413.6	39.2	418.6	39.2
		t2: unshaded	48.0	29.9	55.5	29.1	56.1	28.1
	7	*t1: partially shaded*	397.6	36.8	413.0	38.9	413.1	38.2
		t2: unshaded	520.1	34.8	530.8	34.9	536.5	36.1
	8	*t1: partially shaded*	398.4	36.8	413.9	39.2	426.3	38.2
		t2: unshaded	519.4	33.2	528.8	33.1	529.1	31.3
	9	*t1: partially shaded*	398.5	37.1	414.6	39.3	420.7	38.6
		t2: unshaded	519.5	31.4	58.4	31.1	64.3	29.8

90	1	*t1: partially shaded*	270.6	50.9	289.8	48.2	296.9	48.5
		t2: unshaded	436.3	49.1	457.1	44.4	455.3	46.6
	2	*t1: partially shaded*	270.6	50.8	290.6	48.3	296.0	49.0
		t2: unshaded	23.7	49.3	40.8	43.2	42.3	42.1
	3	*t1: partially shaded*	270.7	50.9	291.9	48.3	288.7	47.8
		t2: unshaded	26.0	47.9	38.6	41.8	38.6	42.1
	4	*t1: partially shaded*	270.5	50.9	289.4	48.4	297.1	49.9
		t2: unshaded	436.7	48.1	458.0	44.6	459.8	42.8
	5	*t1: partially shaded*	270.5	50.9	290.4	48.4	296.7	48.2
		t2: unshaded	24.3	46.4	41.9	43.8	42.1	43.4
	6	*t1: partially shaded*	270.7	50.9	291.6	48.4	300.8	48.2
		t2: unshaded	26.6	46.9	39.9	42.8	39.8	42.4
	7	*t1: partially shaded*	270.9	50.9	289.2	48.5	295.6	48.4
		t2: unshaded	436.5	49.3	459.0	44.8	454.2	45.1
	8	*t1: partially shaded*	271.0	50.8	290.3	48.5	302.4	48.1
		t2: unshaded	24.1	49.3	43.1	44.2	43.5	43.0
	9	*t1: partially shaded*	271.0	50.9	291.4	48.6	294.7	45.4
		t2: unshaded	26.5	48.6	41.3	43.5	41.1	43.4

Appendix C

Monitoring station setup

This appendix shows all information from the monitoring station validation that was conducted in Chapter 5. In Fig. 6.7 a top view and the exact locations of where the horicatcher images, the collection location of the input DHI/DNI measurements and the measurement location at POA 1/POA 2 is given.

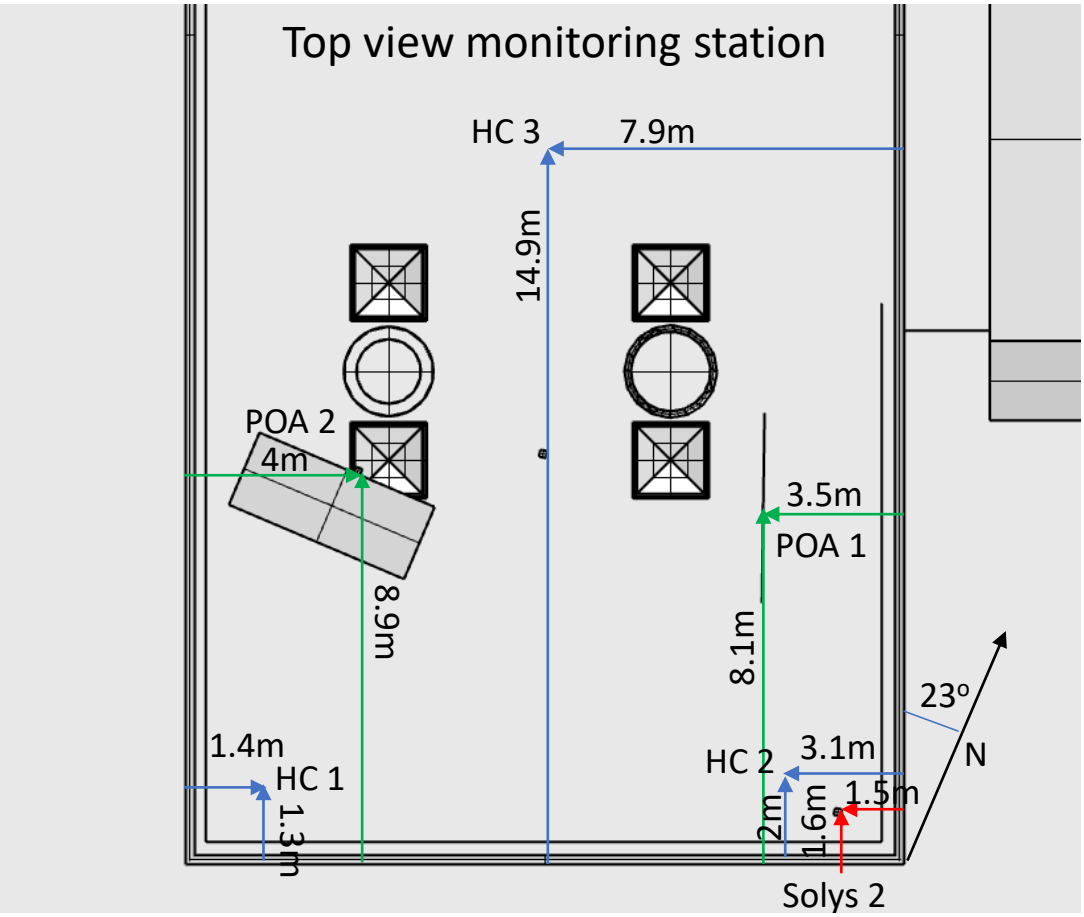

Figure 6.7: Top view of the monitoring station roof. Also indicated is the location and distances of the horicatcher images (HC), the input DHI/DNI measurements from the Solys 2 and the measurement location (POA 1 and POA 2) to be replicated.

Skyline validation with horicatcher image

In the Fig. 6.8 the horicatcher pictures for the three locations on the monitoring roof is displayed. For location 1 and 3 additional pictures where taken at a higher elevation (.6m and 1.6m respectively).

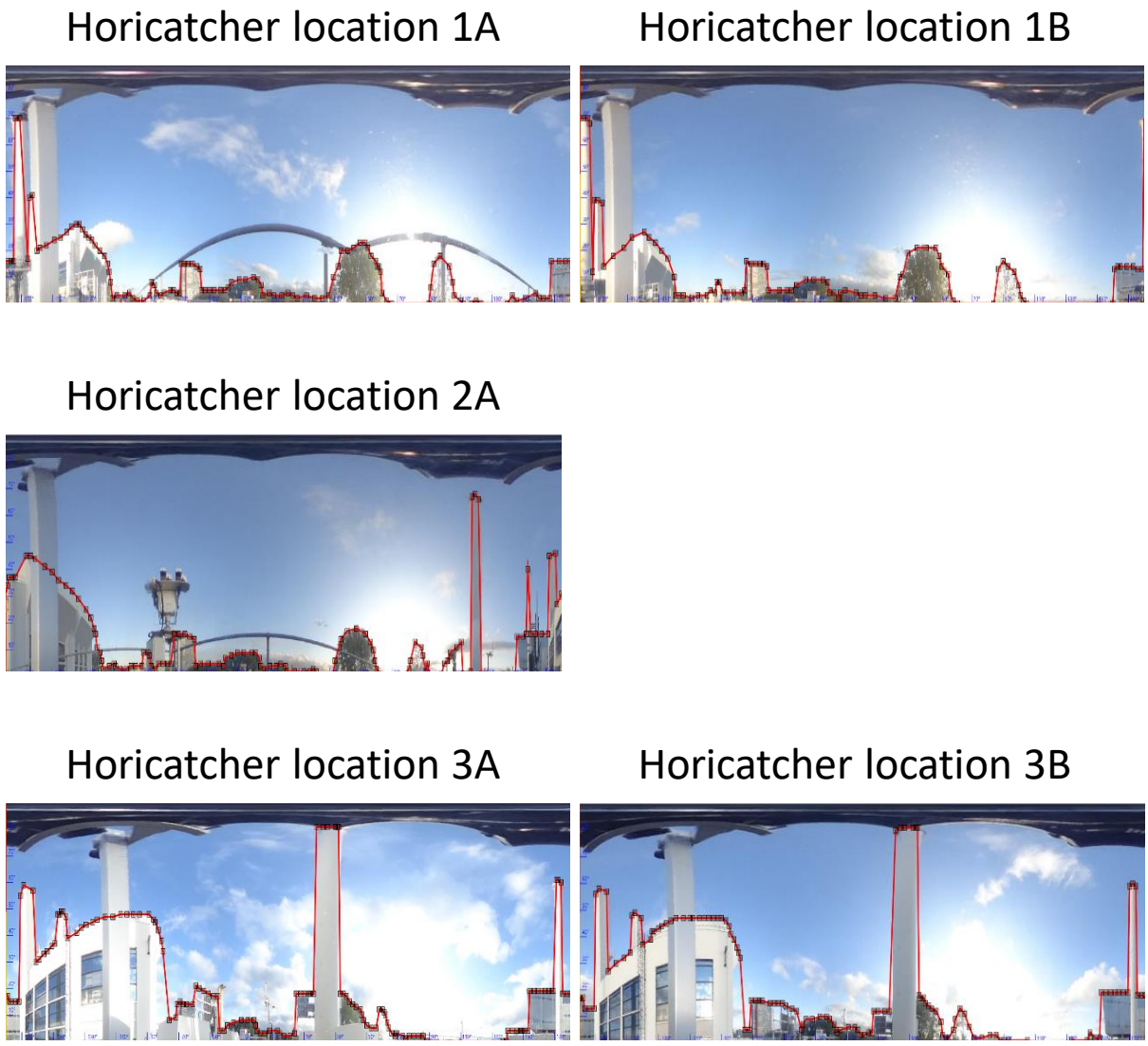

Figure 6.8: Horicatcher pictures extracted from meteonorm at location 1 to 3. For location 1 and 3 additional pictures where taken at an higher elevation.

Ray casting result

This section shows all information from the ray casting performed within the Grasshopper plug-in of the Rhinoceros program that was conducted in Chapter 5. The Table below gives the view factor ($VF_{i\rightarrow k}$), $Tilt_i$, $Azimuth_i$ and average SVF of reflecting surface (identified by a particular id). Since multiple rays intercept in a surface the sum of all the rays and the average SVF is given.

Ray casting results for POA 1

Surface id	VF	Tilt	Azimuth	SVF
11	4.23E-06	90	333.5	0.486709
12	1.77E-05	90	331.4998	0.492819
13	0.000293	90	328	0.492781
14	0.000448	90	323	0.485698
15	0.000311	90	319.5	0.499188
16	0.00012	90	316	0.499073
17	0.000577	90	312.5	0.476286
18	0.000142	90	310.5003	0.476032
19	0.000267	90	308.9999	0.479589
20	0.000585	90	306.5	0.478556
21	0.000225	90	304.4999	0.486804
22	0.00023	90	303.5001	0.485521
23	0.000739	90	301.5	0.48783
24	0.000802	90	298.4999	0.485139
25	0.000398	90	296.0001	0.482891
26	0.000732	90	293	0.48386
27	0.000391	90	289.0001	0.479303
28	0.116572	0	180	0.723683
56	0.017872	46.22461	247	0.595659
58	0.002506	90	247	0.309853
60	0.000198	90	337	0.196338
61	0.003734	90	247	0.316115
62	0.000113	90	337	0.302024
63	9.80E-05	90	337	0.278277
73	0.000473	90	247	0.165961
74	0.000475	90	247	0.14329
75	0.000461	90	247	0.168606
76	0.000443	90	247	0.162805
77	0.000333	90	247	0.154086
78	0.000316	90	247	0.139732
79	0.000342	90	247	0.155243
80	0.000455	90	247	0.132482
81	0.000375	90	247	0.159402
82	0.000473	90	247	0.142016
83	0.000342	89.99998	247	0.149554
84	0.00036	89.99998	247	0.160043
85	0.000373	89.99998	247	0.176615
86	0.00038	89.99998	247	0.16583
87	0.000478	89.99998	247	0.141574
88	0.001569	89.99999	247	0.138344
89	0.001641	89.99999	247	0.146547
90	0.00137	89.99999	247	0.14794
91	0.001157	89.99999	247	0.131589
92	0.000808	89.99999	247	0.10825
93	0.000694	90.00001	247	0.079949
94	0.001179	90.00001	247	0.103437
95	0.00153	90.00001	247	0.139614
96	0.001851	90.00001	247	0.150475
97	0.001889	90.00001	247	0.137111
98	0.002816	89.99999	247	0.140108
99	0.002729	89.99999	247	0.151655
100	0.002146	89.99999	247	0.125395
101	0.001327	89.99999	247	0.075148
102	0.000241	89.99999	247	0.049344
135	8.60E-05	29.99999	157	0.522561
136	8.00E-05	30.00001	157	0.362443
137	0.00015	29.99999	157	0.497014

Ray casting results for POA 2

Surface id	VF	Tilt	Azimuth	SVF
1	0.000389	90	7.499932	0.476055
2	0.000443	90	3.999955	0.475676
3	0.00074	90	359.5	0.476912
4	0.000588	90	355	0.477299
5	0.000541	90	351.5	0.483484
6	0.000196	90	349.4998	0.484232
7	0.000779	90	347.0001	0.484771
8	0.000334	90	343.4999	0.482972
9	0.00042	90	340.5	0.484721
10	0.000645	90	336.9999	0.483798
11	0.00059	90	333.5	0.485022
12	0.000284	90	331.4998	0.490234
13	0.002209	90	328	0.489601
14	0.001053	90	323	0.481352
15	0.000766	90	319.5	0.47732
16	0.000614	90	316	0.498351
18	0.000142	90	310.5003	0.472946
19	0.00024	90	308.9999	0.475462
20	0.000397	90	306.5	0.478675
21	0.000155	90	304.4999	0.482958
22	0.000151	90	303.5001	0.484347
23	0.000433	90	301.5	0.484427
24	0.000402	90	298.4999	0.482889
25	9.80E-05	90	296.0001	0.48503
26	0.000264	90	293	0.482764
27	0.000131	90	289.0001	0.476546
28	0.003896	0	180	0.886901
29	4.27E-06	90	99.00007	0.372497
30	4.83E-05	90	96.00001	0.381479
32	6.95E-05	90	92.5004	0.413119
33	0.000442	90	91.00006	0.420013
34	0.000569	90	89.00026	0.402524
35	0.001134	90	86.49978	0.419858
37	0.001028	90	82.50011	0.427612
38	0.0002	90	80.50036	0.423883
39	7.80E-05	90	79.5002	0.390153
40	3.70E-05	90	78.00008	0.390779
41	9.60E-05	90	52.00003	0.426539
42	0.00048	90	49.99995	0.450753
43	0.000494	90	48.5001	0.459681
44	0.001164	90	46.49989	0.466942
45	0.002148	90	43.50011	0.468754
46	0.002566	90	40.49994	0.47003
47	0.00095	90	38.49996	0.480385
48	0.003091	90	35.99999	0.477691
49	0.004235	90	31.99998	0.478345
50	0.003249	90	27.99999	0.476128
51	0.004575	90	23.50001	0.479378
52	0.001873	90	19.5	0.469973
53	0.000291	90	17.49985	0.457215
54	0.000188	90	16.00006	0.453922
62	0.000215	90	337	0.327186
63	0.00035	90	337	0.336749
162	5.39E-06	3.277703	337	0.955702
172	2.80E-05	90	247	0.443152
185	0.000255	90	247	0.451321
188	0.00028	90	157	0.491843

Ray casting results for POA 1 (continued)

138	0.000165	29.99997	157	0.468297
139	0.000177	29.99991	157	0.527702
140	0.000186	29.99999	157	0.439755
142	8.30E-05	30.00003	157	0.443672
143	8.80E-05	30.00001	157	0.448042
144	9.20E-05	29.99999	157	0.521816
145	9.40E-05	30.00003	157	0.582743
147	0.000369	30.00001	157	0.455855
148	0.000444	30.00001	157	0.468551
149	0.000572	29.99997	157	0.484639
150	0.000642	30.00003	157	0.481512
151	0.000551	30.00003	157	0.459079
152	0.000973	29.99999	157	0.394753
153	0.00161	29.99999	157	0.437314
154	0.001635	29.99996	157	0.4475
155	0.001605	30	157	0.445958
156	0.000892	30	157	0.382913
157	0.002319	30.00001	157	0.415025
158	0.003699	30.00001	157	0.454008
159	0.003573	29.99997	157	0.426248
160	0.001501	30.00001	157	0.351915
162	3.20E-05	3.277703	337	0.943121
164	0.00456	128.8652	157	0.165029
168	7.80E-05	0	0	0.779165
169	0.001547	90	247	0.17543
172	0.043448	90	247	0.430216
175	0.003772	0	0	0.846391
182	0.011313	90	247	0.202276
183	0.001078	90	247	0.175201
184	0.000551	90	246.9999	0.160479
185	0.000457	90	247	0.467886
188	0.000442	90	157	0.491843
190	0.000341	90	247	0.475298
193	0.002949	90	157	0.476802
195	0.000617	90	157	0.323072
197	0.000244	90	157	0.345547
198	0.000594	90	157	0.353498
199	0.000605	90	157	0.367476
200	0.001125	90	157	0.351635
207	0.001272	90	247	0.184364
208	1.40E-05	90	247	0.419709
209	4.20E-05	90	247	0.415743
210	2.80E-05	90	247	0.415309
211	4.20E-05	90	247	0.416245
212	4.20E-05	90	247	0.413582
213	2.80E-05	90	247	0.395736
214	2.80E-05	90	247	0.387537
215	4.90E-05	90	247	0.436185
216	8.50E-05	90	247	0.430444
217	0.00012	90	247	0.425837
218	0.000102	90	247	0.429028
219	0.000102	90	247	0.424139
220	9.90E-05	90	247	0.408549
221	6.60E-05	90	247	0.399628
222	0.000104	90	247	0.450904
223	0.000227	90	247	0.446084
224	0.000252	90	247	0.441356
225	0.000232	90	247	0.444208

Ray casting results for POA 2 (continued)

266	2.22E-05	128.8652	157	0.160911
268	8.12E-06	90	157	0.282717
269	0.001068	89.99999	247	0.445958
293	0.001274	46.22448	337	0.641625
294	0.000538	46.22438	67	0.657929
300	0.000136	90	67.00003	0.350561
301	0.000235	90	67.00003	0.350116
605	0.011272	90	169.8571	0.456662
606	0.008711	90	195.5716	0.462588
607	0.003996	90	221.2855	0.468048
617	0.002854	90	118.4284	0.448911
618	0.006584	90	144.1429	0.457408
1509	0.001704	0	0	0.968289
1511	0.000874	90	335.5498	0.438481
1514	0.000325	90	245.5498	0.445577
1515	0.001344	0	0	0.951797
1518	0.000104	90	65.54981	0.426555
1519	0.003765	90	335.4359	0.420891
1521	0.002632	0	180	0.940382
1523	0.006616	90	335.5498	0.384762
1527	0.002741	0	0	0.826246
1530	0.000696	90	335.5071	0.413839
1531	0.000157	90	65.50708	0.319581
1534	8.20E-05	0	0	0.969864
1535	3.92E-05	90	335.5498	0.43397
1547	0.001104	90	335.5498	0.478774
1548	0.000379	90	245.5498	0.481093
1553	0.000339	90	335.3153	0.470285
1554	8.90E-05	90	245.3153	0.330366
1555	9.20E-05	90	335.3153	0.317412
1561	0.000555	90	335.3153	0.485121
1562	0.000121	90	245.3153	0.426999
1566	0.000236	0	0	0.69537
1575	0.00045	90	335.3153	0.408337
1576	4.00E-05	90	245.3153	0.422697
1579	3.50E-05	180	0	0
1582	0.001146	90	335.3153	0.462701
1583	0.000196	90	245.3153	0.41572
1587	4.20E-05	90	335.3153	0.492402
1837	5.10E-05	180	0	0
1839	0.002149	90	244.6086	0.496767
1841	2.90E-05	90	334.6085	0.476221
1845	0.000343	90	244.609	0.500058
1847	3.00E-05	180	180	0
1851	0.000253	90	334.6085	0.416801
1856	5.50E-05	90	244.6085	0.412803
1857	0.000188	90	334.6086	0.486343
1860	2.70E-05	90	334.6086	0.499944
1862	0.000463	90	244.6085	0.332174
1871	2.70E-05	90	334.6086	0.185594
1872	2.80E-05	90	334.6086	0.448383
1877	3.20E-05	90	244.6077	0.44129
1884	0.000269	90	244.6086	0.480709
1933	3.00E-05	90	332.9631	0.469146
1935	5.60E-05	90	245.9	0.478052
1962	0.000125	90	336.3194	0.458199
1965	0.000148	90	246.3194	0.477861
1970	5.30E-05	90	335.5859	0.344228

Ray casting results for POA 1 (continued)

226	0.00023	90	247	0.438041
227	0.000246	90	247	0.42784
228	0.000143	90	247	0.422908
229	0.000956	90	247	0.446877
230	0.002485	90	247	0.444757
231	0.003168	90	247	0.442364
232	0.002838	90	247	0.439013
233	0.002887	90	247	0.433583
234	0.002457	90	247	0.42452
235	0.001139	90	247	0.4149
236	9.50E-05	120	157	0.197649
237	9.50E-05	120	157	0.200535
238	9.40E-05	120	157	0.202677
244	0.000189	120	157	0.204531
245	0.000188	120	157	0.214376
249	9.60E-05	120	157	0.200535
250	9.50E-05	120	157	0.213903
251	0.001	120	157	0.206685
252	0.00055	120	157	0.209058
253	0.000438	120	157	0.207484
254	0.000158	120	157	0.193542
257	0.000494	120	157	0.170059
258	0.001138	120	157	0.188425
259	0.002208	120	157	0.196803
260	0.00289	120	157	0.199516
261	0.007565	120	157	0.196981
262	0.005341	120	157	0.19547
263	0.002548	120	157	0.181615
264	0.00068	120	157	0.134297
266	0.038663	128.8652	157	0.161533
267	4.40E-05	62.60317	157	0.690031
268	0.097503	90	157	0.402977
269	0.018473	89.99999	247	0.402112
292	2.10E-05	0	0	0.908864
298	3.00E-05	46.24029	157	0.519554
299	0.000512	46.22448	337	0.600446
302	0.000115	133.7754	337	0
448	4.16E-06	47.80565	168.1084	0.491163
450	2.49E-06	47.81162	212.6064	0.636773
461	5.82E-06	47.80563	100.3254	0.344051
1030	7.31E-06	61.93253	147.266	0.353812
1038	8.92E-06	62.84141	100.3739	0.155814
1041	2.44E-06	61.33393	235.7153	0.575687
1042	4.06E-06	61.29489	190.6503	0.550684
1043	5.68E-06	63.53939	167.7806	0.468641
1071	7.35E-06	27.90443	100.6512	0.398744
1080	5.72E-06	27.90452	168.4339	0.599782
1089	4.09E-06	27.94615	235.715	0.690995
1374	7.40E-06	46.41603	100.0054	0.238251
1380	5.76E-06	46.46622	145.0693	0.384787
1386	4.11E-06	46.41601	190.005	0.541515
1392	2.47E-06	46.46637	235.0696	0.644923
1428	2.48E-06	62.99003	212.7323	0.58819
1454	5.79E-06	46.3646	121.9631	0.323014
1460	4.14E-06	46.35844	167.4649	0.477309
1515	0.002166	0	0	0.961759
1517	0.001375	90	335.5498	0.436164
1527	0.005126	0	180	0.951722

Ray casting results for POA 2 (continued)

1971	2.50E-05	90	245.586	0.407921
1972	2.50E-05	90	335.5859	0.26552
1973	0.000132	90	245.5859	0.473582
1995	4.08E-05	90	244.6086	0.378801
1997	6.09E-06	90	244.6086	0.062046
2000	1.77E-06	90	334.6091	0.498215
2008	5.36E-07	90	244.6087	0.370589
2033	4.79E-05	90	244.6086	0.400156
2036	6.43E-06	90	244.6086	0.35398
2056	3.10E-07	90	244.6086	0.400695
2064	1.96E-05	90	244.6086	0.351621
2066	1.38E-06	90	334.6086	0.324633
2072	4.96E-06	90	334.6085	0.214209
2116	1.22E-05	90.00004	244.6086	0.339639
2130	0.029364	0	0	0.929925

Ray casting results for POA 1 (continued)

1529	0.024726	90	335.5498	0.378471
1540	0.000723	0	0	0.964457
1541	0.000385	90	335.5498	0.424864
1553	0.00062	90	335.5498	0.47444
1554	0.000286	90	245.5498	0.482448
1557	0.000249	0	180	0.741728
1559	0.000328	90	335.3153	0.468887
1560	7.40E-05	90	245.3153	0.348427
1561	0.000265	90	335.3153	0.363766
1567	0.000282	90	335.3153	0.480259
1568	2.10E-05	90	245.3153	0.423821
1574	0.000105	90	335.3153	0.462588
1575	1.60E-05	90	245.3153	0.351498
1581	0.000296	90	335.3153	0.440251
1582	1.40E-05	90	245.3153	0.382446
1586	6.76E-05	0	180	0.727112
1588	0.000203	90	335.3153	0.458854
1593	2.10E-05	90	335.3153	0.492402
1594	3.80E-05	90	245.3154	0.320751
1597	0.000411	90	168.3571	0.379588
1604	0.000259	90	157.1621	0.290248
1617	0.000197	90	150.2952	0.454663
1639	9.60E-05	90	245.2828	0.218487
1674	0.000678	0	180	0.984681
1680	0.000482	90	245.2828	0.343264
1682	0.002598	90	245.2828	0.441301
1685	0.001826	89.99998	245.2828	0.472843
1687	0.002281	90	245.2828	0.45038
1691	0.000388	90	245.2828	0.409552
1706	0.000384	90	335.2831	0.47254
1707	0.000572	90	245.2828	0.485143
1773	0.000288	90	335.2828	0.345465
1845	0.007269	90	244.6086	0.496934
1847	7.50E-05	90	334.6085	0.324812
1851	0.002141	90	244.609	0.486463
1857	0.001171	90	334.6085	0.289224
1862	7.60E-05	90	244.6085	0.456101
1863	0.0012	90	334.6086	0.493005
1866	7.60E-05	90	334.6086	0.499944
1868	0.001186	90	244.6085	0.3908
1877	7.60E-05	90	334.6086	0.065778
1878	7.50E-05	90	334.6086	0.341534
1883	6.60E-05	90	244.6077	0.454412
1890	0.000632	90	244.6086	0.471879
1896	7.70E-05	90	334.6084	0.361626
1918	4.50E-05	90	64.60853	0
1939	0.000141	90	332.9631	0.471333
1941	0.00045	90	245.9	0.480941
1968	0.000891	90	336.3194	0.459907
1971	0.000678	90	246.3194	0.479314
1976	0.000143	90	335.5859	0.381064
1977	5.10E-05	90	245.586	0.412328
1978	5.20E-05	90	335.5859	0.282796
1979	0.000281	90	245.5859	0.473891
2001	0.000856	90	244.6086	0.354286
2006	9.00E-05	90	334.6091	0.498215
2014	0.000441	90	244.6087	0.333282
2039	0.000854	90	244.6086	0.402559

Ray casting results for POA 2 (continued)

Ray casting results for POA 1 (continued)

2042	8.20E-05	90	244.6086	0.368014
2056	0.000184	90	334.6087	0.368354
2057	0.000271	90	244.6085	0.418289
2059	9.20E-05	90	334.6086	0.499944
2060	9.10E-05	90	244.6086	0.433719
2062	0.000271	90	244.6086	0.420152
2064	0.000544	90	244.6086	0.338249
2068	9.20E-05	90	334.6087	0.499944
2070	0.000509	90	244.6086	0.364778
2072	8.80E-05	90	334.6086	0.252849
2078	8.20E-05	90	334.6085	0.084024
2122	0.000338	90.00004	244.6086	0.348103
2123	8.70E-05	134.1769	334.6086	0.090972
2132	0.000473	90	336.0403	0.500091
2135	0.001128	90	246.0404	0.471089
2136	0.141399	0	0	0.744777

Ray casting results for POA 2 (continued)